The Astrophysical Journal Supplement Series, 247:48 (44pp), 2020 April https://doi.org/10.3847/1538-4365/ab7919
© 2020. The American Astronomical Society. All rights reserved.

Modeling Dense Star Clusters in the Milky Way and Beyond with the CMC Cluster Catalog

Kyle Kremer[1,2], Claire S. Ye[1,2], Nicholas Z. Rui[3], Newlin C. Weatherford[1,2], Sourav Chatterjee[4], Giacomo Fragione[1,2], Carl L. Rodriguez[5], Mario Spera[1,2,6,7], and Frederic A. Rasio[1,2]
[1] Department of Physics & Astronomy, Northwestern University, Evanston, IL 60208, USA
[2] Center for Interdisciplinary Exploration & Research in Astrophysics (CIERA), Northwestern University, Evanston, IL 60208, USA
[3] Department of Astronomy, University of California at Berkeley, Berkeley, CA 94720, USA
[4] Tata Institute of Fundamental Research, Homi Bhabha Road, Mumbai 400005, India
[5] Harvard Institute for Theory and Computation, 60 Garden Street, Cambridge, MA 02138, USA
[6] Dipartimento di Fisica e Astronomia "G. Galilei," University of Padova, Vicolo dell'Osservatorio 3, I–35122, Padova, Italy
[7] INFN, Sezione di Padova, Via Marzolo 8, I–35131, Padova, Italy
Received 2019 October 31; revised 2020 February 20; accepted 2020 February 20; published 2020 March 23

Abstract

We present a set of 148 independent *N*-body simulations of globular clusters (GCs) computed using the code CMC (Cluster Monte Carlo). At an age of ∼10–13 Gyr, the resulting models cover nearly the full range of cluster properties exhibited by the Milky Way GCs, including total mass, core and half-light radii, metallicity, and galactocentric distance. We use our models to investigate the role that stellar-mass black holes play in the process of core collapse. Furthermore, we study how dynamical interactions affect the formation and evolution of several important types of sources in GCs, including low-mass X-ray binaries, millisecond pulsars, blue stragglers, cataclysmic variables, Type Ia supernovae, calcium-rich transients, and merging compact binaries. While our focus here is on old, low-metallicity GCs, our CMC simulations follow the evolution of clusters over a Hubble time, and they include a wide range of metallicities (up to solar), so that our results can also be used to study younger and higher-metallicity star clusters. Finally, the output from these simulations is available for download at https://cmc.ciera.northwestern.edu/home/.

Unified Astronomy Thesaurus concepts: Globular star clusters (656); Stellar mass black holes (1611); Computational methods (1965); Blue straggler stars (168); Binary stars (154); Cataclysmic variable stars (203); X-ray binary stars (1811); Stellar dynamics (1596)

Supporting material: animation

1. Introduction

Globular clusters (GCs) present rich opportunities for studying the importance of gravitational dynamics in dense stellar environments. In a GC, dynamical interactions play significant roles in both the evolution and survival of the system as a whole (see, e.g., Heggie & Hut 2003) and also in the formation of a number of exotic populations, including X-ray (e.g., Clark 1975; Verbunt et al. 1984; Heinke et al. 2005; Ivanova 2013; Giesler et al. 2018; Kremer et al. 2018a), radio (e.g., Lyne et al. 1987; Sigurdsson & Phinney 1995; Ivanova et al. 2008; Ransom 2008; Fragione et al. 2018c; Ye et al. 2019), and gravitational wave (GW) sources (e.g., Moody & Sigurdsson 2009; Banerjee et al. 2010; Bae et al. 2014; Ziosi et al. 2014; Rodriguez et al. 2015, 2016; Askar et al. 2017; Banerjee 2017; Fragione & Kocsis 2018; Hong et al. 2018; Rodriguez et al. 2018a; Samsing & D'Orazio 2018; Kremer et al. 2019c; Zevin et al. 2019).

About 150 GCs are known in the Milky Way (MW; e.g., Harris 1996; Baumgardt & Hilker 2018). All are sufficiently dense to have experienced significant relaxation, and many have extremely high core densities. Furthermore, all GCs appear fundamentally different from the stellar population in the Galactic field: they are generally old systems (ages 10 Gyr or more) with low metallicities (typically $Z \sim 0.1\ Z_{\odot}$), and they also appear to have much lower binary fractions ($f_b \lesssim 5\%$–30%) compared to the field ($f_b \gtrsim 50\%$; e.g., Sana et al. 2012; Kroupa & Jerabkova 2018). Over the past half century, a number of key differences among the MW GCs have been unveiled. First, GCs have individual masses that span several orders of magnitude, from $\sim 10^3$–$10^4\ M_{\odot}$ clusters that exhibit features similar to their younger open cluster counterparts all the way to giant clusters with masses well in excess of $10^6\ M_{\odot}$ that may be linked to galactic nuclei (Harris 1996; Baumgardt & Hilker 2018). Second, GCs in the MW exhibit a striking bimodal distribution in core radii separating the so-called "core-collapsed" and "non-core-collapsed" clusters (e.g., Harris 1996; McLaughlin & van der Marel 2005). Third, the numbers of various observed tracers of dynamical interactions—such as X-ray binaries, radio pulsars, cataclysmic variables (CVs), and blue stragglers (BSs)—can vary dramatically from cluster to cluster (e.g., Ransom 2008; Heinke 2010; Ferraro et al. 2012; Knigge 2012).

Much of the recent theoretical work on GC dynamics has focused on the crucial role played by stellar black hole (BH) remnants in these systems. Several studies have shown that large numbers of stellar-mass BHs can be retained in typical GCs all the way to the present, and their dynamical interactions in the cluster core over its ∼12 Gyr of evolution provide a natural physical explanation for many of the diverse cluster features alluded to in the previous paragraph (e.g., Mackey et al. 2008; Breen & Heggie 2013; Morscher et al. 2015; Askar et al. 2018; Kremer et al. 2019a). The first BH candidate in a cluster was identified in the extragalactic GC NGC 4472 by Maccarone et al. (2007) through X-ray observations. Soon thereafter, several BH candidates were identified in the MW GCs through X-ray and/or radio measurements, including M22 (Strader et al. 2012), M62 (Chomiuk et al. 2013), 47 Tuc (Miller-Jones et al. 2015), and M10 (Shishkovsky et al. 2018). Recently, the MUSE survey

team has reported a BH candidate in NGC 3201, marking the first identification of a stellar-mass BH via purely dynamical measurements (Giesers et al. 2018). Subsequent follow-up has revealed two additional radial velocity BH candidates within NGC 3201 (Giesers et al. 2019).

Computational and theoretical analyses have corroborated the recent observational evidence for BHs in GCs. In particular, it is now generally understood that a large number of BHs (hundreds to thousands) form through stellar evolution processes in clusters (e.g., Kroupa 2001; Morscher et al. 2015). The subsequent evolution of a cluster's BH population is then governed by a number of dynamical processes: once formed, the BHs will quickly mass-segregate to the center of their host cluster on a sub-gigayear timescale, assembling a BH subsystem that dominates the cluster's innermost region (e.g., Spitzer 1969; Kulkarni et al. 1993; Sigurdsson 1993). In this BH-dominated core, dynamically hard BH binaries promptly form through three-body interactions (e.g., Morscher et al. 2015). As they sink to the cluster core, these binaries provide energy to passing stars in scattering interactions, a process that further hardens the binaries while energizing the rest of the cluster (e.g., Heggie & Hut 2003; Breen & Heggie 2013). Furthermore, as BHs undergo these series of (binary-mediated) dynamical encounters within their host cluster's core, they frequently attain large dynamical kicks that temporarily eject them from the core. Once ejected, these BHs will rapidly mass-segregate back to the cluster's core, thereby depositing further energy into the cluster's stellar bulk. Cumulatively, these BH dynamics (binary burning, ejection, and mass segregation) act as an energy source for their host cluster in a process we refer to as "BH burning" (for review, see Kremer et al. 2020). These effects are now well understood, and several in-depth studies have achieved consensus (Merritt et al. 2004; Mackey et al. 2007, 2008; Breen & Heggie 2013; Peuten et al. 2016; Wang et al. 2016; Arca Sedda et al. 2018; Kremer et al. 2018b; Kremer et al. 2019a; Zocchi et al. 2019; Antonini & Gieles 2020). While a large BH population remains in a cluster, the cluster exhibits a large observed core radius owing to BH burning. The observed core radius steadily shrinks as the BH population erodes, and only when the BHs are almost fully depleted can a cluster attain a structure that would observationally be identified as "core-collapsed."

In Kremer et al. (2019a), we demonstrated that the initial cluster size (set as the initial virial radius, r_v) is the key parameter that determines the ultimate fate of a cluster and its BH population. A cluster's half-mass relaxation time is related to its virial radius through the expression

$$t_{\rm rh} \sim \frac{M^{1/2}}{\langle m\rangle G^{1/2}\ln\Lambda} r_v^{3/2} \quad (1)$$

(Equations (2)–(63) of Spitzer 1987), where M is the total cluster mass, $\langle m\rangle$ is the mean stellar mass, and $\ln\Lambda$ is the Coulomb logarithm where $\Lambda \simeq 0.4N$, where N is the total number of particles. Thus, clusters with smaller initial r_v have shorter relaxation times and are thus more dynamically evolved at their present age ($t \sim 12$ Gyr) compared to clusters born with larger initial r_v.

In Kremer et al. (2019a), we employed a small set of cluster simulations with a number of initial parameters, such as total particle number and metallicity, fixed to reflect the median values of the clusters observed in the MW. In that analysis, we developed best-fit models for a set of four MW clusters (NGC 3201, M10, M22, and NGC 6752) by matching various observed features (including surface brightness and velocity dispersion profiles). Here, we expand on the results of Kremer et al. (2019a) and explore the effect of initial virial radii, and subsequent BH dynamics, on clusters of various masses, metallicity, and locations within the Galactic tidal field. We develop a grid of 148 independent cluster simulations, run using CMC (for Cluster Monte Carlo), which covers roughly the complete range of GCs observed at present in the MW. In Section 2, we summarize the main computational methods incorporated within CMC, describe the choice of initial parameters for our grid of simulations, and define important quantities such that our models can be compared to observations. In Section 3, we compare various features of our grid to the full population of MW clusters and demonstrate the ways that stellar-mass BHs determine cluster features. In Section 4, we discuss the number of BH and neutron star (NS) binaries that appear in our models at late times and discuss the implications for both radial velocity searches for BHs and NSs in clusters and those for X-ray binaries. We discuss the total number of pulsars in our models and compare to observations in Section 5. In Section 6, we discuss white dwarf (WD) populations and applications to CVs and high-energy transient events. In Section 7, we discuss luminous star collisions and possible applications for massive BH formation. We explore the number of BSs found in our models in Section 8 and binary BH mergers plus applications to GW astronomy in Section 9. We discuss our results and conclude in Section 10.

2. Methods

2.1. Summary of CMC

To model GCs, we use CMC, a Hénon-type Monte Carlo code that computes the long-term evolution of GCs (Hénon 1971a, 1971b; Joshi et al. 2000, 2001; Fregeau et al. 2003; Chatterjee et al. 2010, 2013; Pattabiraman et al. 2013; Rodriguez et al. 2015). CMC incorporates various physical processes relevant to both a cluster's structural evolution and the evolution of its constituent objects. A detailed description of CMC that will include detailed descriptions of all the latest updates, as well as a comprehensive user guide, will be presented in an upcoming paper (C. L. Rodriguez et al. 2019, in preparation). Here, we briefly review the methods relevant to several key physical processes.

1. *Stellar and binary evolution:* We incorporate the single-star and binary-star evolution codes SSE and BSE (Hurley et al. 2000, 2002), where we have implemented up-to-date prescriptions of compact object formation (Fryer & Kalogera 2001; Vink et al. 2001; Belczynski et al. 2002; Hobbs et al. 2005; Morscher et al. 2015), as described below.

2. *Neutron star formation:* We implement two scenarios for NS formation: standard iron core-collapse supernovae (CCSNe) and electron-capture supernovae (ECSNe). We adopt the "rapid model" for stellar remnants formed through CCSNe (Fryer et al. 2012). As described in Ye et al. (2019, and references therein), ECSNe may occur through several channels, including evolution-induced collapse, accretion-induced collapse of an oxygen-neon WD that accretes to the Chandrasekhar limit, or merger-induced collapse of a pair of WDs. We direct the reader to Ye et al. (2019) for more detailed discussion of each of these different formation scenarios and simply note here that we assume that all NSs formed through CCSNe (ECSNe) receive natal kicks drawn from

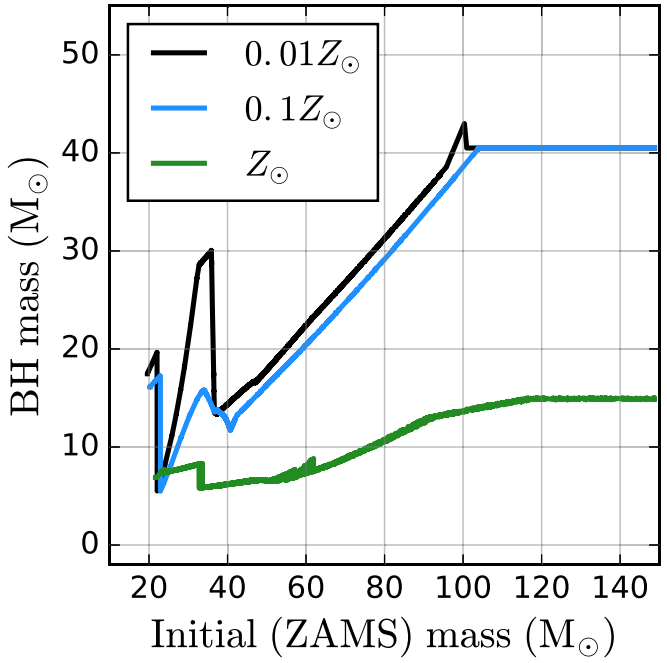

Figure 1. BH mass vs. initial (zero-age main sequence; ZAMS) mass for single stars computed using the stellar evolution prescriptions adopted in this study (see text for details). The three colors denote the three metallicities considered in this study.

a Maxwellian with dispersion $\sigma = 265$ km s^{-1} (20 km s^{-1}). Additionally, we now incorporate updated prescriptions for the formation and evolution of pulsars (relating specifically to spin period and magnetic field evolution), as described in Ye et al. (2019).

3. *Black hole formation:* We assume that BHs are formed with mass fallback (again, using the "rapid model" of Fryer et al. 2012) and calculate BH natal kicks by sampling from the same distribution as CCSN NSs but with BH kicks reduced in magnitude according to the fractional mass of fallback material: $V_{\rm BH} = V_{\rm NS}(1 - f_{\rm fb})$, where $V_{\rm NS}$ is the kick velocity drawn from the Hobbs et al. (2005) distribution for CCSN NSs and $f_{\rm fb}$ is the fallback parameter, i.e., the fraction (from 0 to 1) of the stellar envelope that falls back upon core collapse (see Belczynski et al. 2002; Fryer et al. 2012; Morscher et al. 2015, for further details).

We also implement prescriptions to treat pulsational-pair instabilities and pair-instability SNe as described in Belczynski et al. (2016a). To summarize, we assume that any star with a pre-explosion helium core mass between 45 and 65 $M_\odot$ will undergo pulsations that eject large amounts of mass, until the final product is at most 45 $M_\odot$. Assuming that 10% of the final core mass is lost during the conversion from baryonic to gravitational matter at the time of collapse, a BH of mass 40.5 $M_\odot$ remains. We assume that stars with helium core masses in excess of 65 $M_\odot$ are completely destroyed by a pair-instability SN so that no remnant is formed.

In Figure 1, we show the initial–final mass relation for single stars (i.e., neglecting any binary or dynamical effects) and the dependence of this relation on metallicity. As the figure shows (and as is discussed in detail in, e.g., Belczynski et al. 2016a), at metallicities of 0.01 (black curve) and 0.1 $Z_\odot$ (blue curve), the most massive stars ($M_{\rm ZAMS} \gtrsim 100\,M_\odot$) are subject to pulsational-pair instabilities, hence the visible flattening of the BH mass function at 40.5 $M_\odot$ for both populations. However, this is not the case at solar metallicity (green curve in Figure 1). This is because stars at high metallicity are subject to prominent stellar wind mass loss (again, adopting the stellar wind prescriptions of Vink et al. 2001), preventing the formation of helium cores above 45 $M_\odot$.

4. *Direct integration of strong encounters:* During the evolution of a GC, binary stars will often pass sufficiently close to single stars and other binaries to undergo so-called "strong" encounters (e.g., Heggie & Hut 2003). In `CMC` these binary–single and binary–binary (we neglect higher multiples) strong encounters are integrated using `Fewbody` (Fregeau et al. 2004; Fregeau & Rasio 2007). See Fregeau & Rasio (2007) for a detailed description of the use of `Fewbody` within the overall framework of `CMC`. Also, note that `Fewbody` has now been updated to include gravitational radiation reaction for all encounters involving BHs (see Rodriguez et al. 2018a, 2018b, for more information).

5. *Two-body relaxation:* Two-body relaxation is the primary physical process at play in the global evolution of a GC (e.g., Heggie & Hut 2003). We use the Hénon orbit-averaged Monte Carlo method to simulate two-body relaxation (Hénon 1971a, 1971b). We direct the reader to Joshi et al. (2000) for a detailed description of how these techniques are implemented in `CMC`.

6. *Single–single GW capture:* As described in Samsing et al. (2019), binary formation can occur through GW capture of pairs of single BHs in GCs. This mechanism plays an important role in the emerging picture of how binary BHs form and merge in GCs. Here, we allow BH binaries to form through GW capture of pairs of single BHs in our simulations.

7. *Three-body-binary formation:* As the core of a cluster collapses through gravitational instability, the innermost stars will eventually reach high enough densities to form binaries through three-body-binary (3BB) formation (e.g., Heggie & Hut 2003). We adopt the formalism for 3BB formation described in Morscher et al. (2015), with two small modifications. First, we allow binaries to form with $\eta \geqslant 2 = \eta_{\rm min}$, where η is the binary hardness ratio (binary binding energy to background star kinetic energy): $\eta = (Gm_1m_2)/(r_p\langle m\rangle\sigma^2)$. Here, m_1 and m_2 are the binary component masses, r_p is the separation of the objects at pericenter, and $\langle m\rangle$ and σ are the local average mass and velocity dispersion. Note that Morscher et al. (2015) adopted $\eta \geqslant 5 = \eta_{\rm min}$, a conservative assumption that only captures a small subset of all 3BB formation events. For example, see Aarseth & Heggie (1976), which showed that the probability a given three-body encounter leads to a binary scales as η^{-2}, indicating that roughly 80% of three-body encounters result in binary formation, even for $\eta = 2$, our assumed $\eta_{\rm min}$. Second, we allow 3BB formation to occur for *all* stars, not only BHs, as was the case in Morscher et al. (2015). The inclusion of these two effects leads to an overall increase in 3BB formation relative to the models of Morscher et al. (2015).

8. *Tidal truncation:* Real GCs are not isolated systems—they are subject to the tidal field of their host galaxy. The assumption of spherical symmetry inherent in Monte Carlo codes like `CMC` does not allow for a direct calculation of stellar loss at the tear-drop-shaped tidal boundary. Instead, we employ an effective tidal mass-loss criterion that attempts to match the tidal mass loss found in direct N-body simulations. In short, for each simulation, we assume a circular orbit around the Galactic center with radius, $R_{\rm gc}$. To calculate the tidal radius of the cluster, a logarithmic potential ($\phi R_{\rm gc} = V_{\rm gc}^2 \ln R_{\rm gc}$) for the galaxy is assumed with circular velocity $V_{\rm gc} = 220$ km s^{-1}

(assuming a flat rotation curve such that $V_{\rm gc}$ is independent of $R_{\rm gc}$). The tidal radius of the cluster is then given by

$$r_t = \left(\frac{GM_c}{2V_{\rm gc}^2}\right)^{1/3} R_{\rm gc}^{2/3}, \quad (2)$$

where M_c is the total cluster mass (see, e.g., Baumgardt & Makino 2003). For a detailed description of the implementation of Galactic tides, see Chatterjee et al. (2010) and Pattabiraman et al. (2013).

9. *Stellar collisions:* Stars in realistic clusters will frequently undergo sufficiently close passages to tidally interact. Depending on the pericenter distance (r_p), stars may undergo tidal captures, tidal disruptions, or physical collisions, all of which are expected to lead to distinct outcomes with distinct electromagnetic signatures. In CMC, we handle close encounters in the "direct collision" approximation, meaning that pairs of stars that pass close to one another are assumed to physically collide only if $r_p \leqslant R_1 + R_2$, where R_1 and R_2 are the radii of the two stars of interest. Such collisions can occur through single–single encounters, as well as during binary-mediated strong encounters that are integrated by Fewbody. See Fregeau & Rasio (2007) for a detailed description of how collisions are computed within CMC.

Over the past several decades it has become clear that (nearly) all GCs host significant chemical abundance spreads, in stark contrast to the old notion that stars in GCs have the same age and chemical abundances. These star-to-star abundance variations within clusters are known as multiple populations (MPs), and the study of MPs has emerged as a pillar of research in the field of star clusters (for a recent review, see Bastian & Lardo 2018). In particular, studies of MPs can place important constraints on various cluster processes, especially those occurring during the earliest evolutionary phases of clusters (e.g., Ventura et al. 2001; Decressin et al. 2007; de Mink et al. 2009; Denissenkov & Hartwick 2014; Gieles et al. 2018). Although examination of chemical abundance spreads and the implications to MPs are rich subjects, we do not incorporate chemical abundance variations in CMC. From the perspective of gravitational N-body dynamics, the chemical abundances of individual stars are a second-order effect; these chemical anomalies have a minimal effect on the long-term dynamical evolution of the cluster (i.e., timescales of $\sim$10 Gyr). However, the various physical processes that may produce these abundance variations may be intimately connected to dynamics in the cluster at *early* times ($t \lesssim 1$ Gyr; e.g., Sills & Glebbeek 2010). In CMC, we simply assume that all stars are born with fixed metallicity at a fixed time and bypass the early phases of cluster and stellar formation from collapse of a molecular cloud (for recent work that considers these processes, see, e.g., Fujii & Portegies Zwart 2016).

2.2. Selection of Initial Model Parameters

In this paper, we present a new set of 148 independent cluster simulations run using CMC. We vary four initial cluster parameters in this study: the total number of particles (single stars plus binaries; $N = 2 \times 10^5$, 4×10^5, 8×10^5, and 1.6×10^6), the initial cluster virial radius ($r_v/{\rm pc} = 0.5$, 1, 2, 4), the metallicity ($Z/Z_\odot = 0.01$, 0.1, 1), and the galactocentric distance ($R_{\rm gc}/{\rm kpc} = 2$, 8, 20). This gives us a $4 \times 4 \times 3 \times 3$ grid for a total of 144 models. We also run four additional models with $N = 3.2 \times 10^6$ particles to characterize the most massive clusters in the MW. For these four models, we fix the galactocentric distance to $R_{\rm gc} = 20$ kpc (for simplicity) and vary metallicity ($Z = 0.01$ and $1\ Z_\odot$) and virial radius ($r_v = 1$ and 2 pc). As a whole, this complete model set shares several similarities to previous large CMC model sets (e.g., Chatterjee et al. 2010, 2013; Morscher et al. 2015; Rodriguez et al. 2018b), with the key differences being that here we expand the range in r_v and Z and also decouple Z and R_{gc}, which, e.g., Morscher et al. (2015) coupled via an assumed Z–$R_{\rm gc}$ correlation based on MW observations. These differences from our previous model sets allow a more expansive comparison to all types of clusters observed in the MW.

A number of initial properties are fixed across all simulations. We assume that all models are initially described by King profiles (King 1962) and adopt a fixed King concentration parameter of $W_0 = 5$. We adopt the initial mass function (IMF) of Kroupa (2001) with masses in the range of 0.08–150 $M_\odot$ and assume an initial stellar binary fraction of $f_b = 5\%$. To assign binaries, an appropriate number of single stars (based on N and f_b) are randomly drawn from the IMF and assigned binary companions, with secondary masses drawn from a flat distribution in mass ratio, q, in the range $q \in [0.1, 1]$ (e.g., Duquennoy & Mayor 1991).

Binary orbital periods are drawn from a distribution flat in log-scale (e.g., Duquennoy & Mayor 1991), with the orbital separations ranging from near contact ($a \geqslant 5(R_1 + R_2)$, where R_1 and R_2 are the stellar radii) to the hard/soft boundary, while binary eccentricities are drawn from a thermal distribution (e.g., Heggie 1975). We evolve each simulation to a final time of 14 Gyr, unless the cluster disrupts or undergoes a collisional runaway, as discussed further in Section 2.3.

In Table 6 in the Appendix, we list all initial cluster properties and various features at the end of the simulations. The output for this set of simulations will be available for download at https://cmc.ciera.northwestern.edu/. These simulations will soon be accompanied by a release of the CMC source code with supplementing documentation (C. L. Rodriguez et al. 2019, in preparation).

2.3. Key Definitions

In this section, we briefly define several terms used throughout the paper that are relevant to our models. In particular, we discuss differences between "observational" and "theoretical" definitions of various terms (such as core radius) and explain our treatment of cluster dissolution and collisional runaways.

Core collapse: From an observational perspective, the term "core collapse" is traditionally used to indicate a particular cluster structure that has a central power-law surface brightness profile, as opposed to non-core-collapsed clusters with profiles that can be well fit by a King model. Thus, observational core collapse refers to a property of a cluster's luminous stars. This is in contrast to the definition occasionally used by theorists that refers to the collapse of a BH-dominated subsystem (we abbreviate as BHS, for "BH subsystem"). This BHS collapse has no direct effect on the light profile of the cluster (Chatterjee et al. 2017b). However, the formation and eventual dissipation of a BHS do have an important *indirect* effect on the cluster's structure (and light profile) through the "BH burning" process, where strong dynamical encounters within the BHS act as an energy source for the rest of the cluster (see Kremer et al. 2020, for review). In this study, we use the term "core-collapsed" in the observational sense. We define a core-collapsed cluster as

one with a luminosity profile exhibiting a prominent central cusp.

Core and half-light radii: Using SSE, CMC calculates the bolometric luminosity and temperature of all stars as a function of time, which allows us to construct Hertzsprung–Russell (H-R) diagrams (see Section 3.5), as well as calculate core and half-light radii consistent with observers' definitions. We estimate the observational half-light radius, $r_{\rm hl}$, of each model by finding the 2D-projected radius that contains half of the cluster's total light. We use the method described in Morscher et al. (2015) and Chatterjee et al. (2017b) to estimate the observational core radius, r_c. Note that the observed core radius is different from the theoretical (mass-density-weighted) core radius (which we denote as $r_{\rm c,\ theoretical}$) traditionally used by theorists (Casertano & Hut 1985).

Disrupted Clusters: As clusters evolve, they lose mass through a variety of processes, including high-mass stellar evolution, ejection of stars through dynamical encounters and natal kicks, and mass loss through the cluster's tidal boundary. In fact, given sufficient time, all tidally bound clusters will eventually disrupt completely through mass loss as a natural consequence of relaxation (see, e.g., Heggie & Hut 2003). The time to complete disruption depends on the cluster's relaxation timescale, as well as its initial "overfilling" factor, which depends on the cluster's position within the MW potential. A handful of models considered in this study undergo complete disruption before reaching the 14 Gyr maximum integration time.

As a cluster begins to tidally disrupt, several of the basic assumptions at the heart of our Monte Carlo approach break down, in particular spherical symmetry and the assumption that the relaxation timescale is significantly longer than the dynamical timescale (disrupting clusters can lose mass on a timescale much shorter than the relaxation time). Therefore, we assume that the cluster has completely disrupted once $t_{\rm relax} > M/\dot{M}$, where $t_{\rm relax}$ and M denote relaxation time and total cluster mass, respectively. In practice, our model clusters typically contain 10,000 stars or less when they meet this criterion. All clusters that disrupt before 14 Gyr are labeled as such in Table 6.

Collisional runaway: As pointed out in a number of recent analyses, clusters with sufficiently high initial densities may lead to large numbers of stellar collisions within the first few megayears, potentially leading to the formation of a very massive star. Such objects may have important implications for the formation of intermediate-mass BHs (IMBHs; e.g., Ebisuzaki et al. 2001; Portegies Zwart & McMillan 2002; Gürkan et al. 2004; Freitag et al. 2006; Portegies Zwart et al. 2010; Goswami et al. 2012). Here, we assume that a cluster has undergone collisional runaway when a star with mass in excess of 500 $M_\odot$ is formed, with this specific limit chosen simply in accordance with earlier work (e.g., Gürkan et al. 2004). Treatment of the runaway process and, in particular, treatment of the various physical processes relevant when an IMBH is present are outside the computational scope of the present version of CMC (however, for a recent attempt at incorporating within CMC the various processes relevant to the presence of an IMBH, see Umbreit et al. 2012). Therefore, in the event of a runaway, we stop the integration of the model. In total, only three models meet the collisional runaway requirement: N16-RV0.5-RG2-Z0.01, N16-RV0.5-RG8-Z0.01, and N16-RV0.5-RG20-Z0.01, marked with asterisks in Table 6. We hope to explore this topic further in future projects.

3. Results

In Table 6 in the Appendix, we list initial conditions and various cluster parameters at the end of each simulation for all models in this study. Models marked with a "–" denote clusters that disrupted before reaching the end of the simulation. In this section, we discuss a number of broad-brush features of our population of models. In Sections 4–9, we go on to explore the formation rates of specific objects in our models.

3.1. Comparison with the MW Cluster Population

In Figure 2, we compare various features of our models to the MW GC data taken from Baumgardt & Hilker (2018).[8] The size of the circle coinciding with a given MW cluster is scaled by the integrated V-band magnitude of that cluster (taken from Harris 1996). Thus, larger circles correspond to clusters that are more luminous in the V band. In the top four panels (panels (a)–(d)), we show comparisons involving the total cluster mass and the "observed" core and half-light radii (r_c and r_h, respectively; see definitions in Section 2.3). The color scale shows the initial virial radius of the GCs, which goes from 0.5 (lightest blue) to 4 pc (darkest blue). To reflect the uncertainty in the ages of MW GCs, we simply show here all model snapshots with evolutionary times in the range of 10–13 Gyr. Each of these separate model snapshots can be viewed as a distinct (although not necessarily statistically independent) realization of a particular cluster.

In panel (e), we compare our models to the Galactocentric distances and metallicities of the MW clusters, with crosses indicating the discrete values of these parameters chosen for our models. Finally, in panel (f), we assign colors based on the total number of BHs retained in each model at the time of the particular snapshot shown.

The four gold-colored symbols in the various panels of Figure 2 mark the locations of four simulations that roughly characterize common cluster types observed in the MW: N8-RV2-RG8-Z0.01 (gold star), representing typical non-core-collapsed clusters with average mass ($2 \times 10^5\ M_\odot$) that have many BHs at present (e.g., NGC 3201 or M22); N8-RV0.5-RG8-Z0.01 (gold circle), representing typical core-collapsed clusters with average mass (e.g., NGC 6752); N2-RV2-RG8-Z0.01 (gold triangle), a low-mass cluster with $M = 5 \times 10^4\ M_\odot$ (e.g., NGC 6144 or Terzan 3); and N32-RV2-RG20-Z0.01 (gold diamond), a massive cluster ($>10^6\ M_\odot$) with well over 1000 BHs at present (e.g., NGC 2808). In Sections 4–8, we discuss the numbers of various stellar sources within each of these four characteristic clusters.

As shown in Figure 2, a clear relation exists between clusters' present-day core radii and their initial virial radii: cluster models with small initial r_v (light-blue scatterpoints) tend to occupy the leftmost regions of the plots shown in panels (a) and (c), while the opposite is true for models with large initial r_v (dark-blue scatterpoints). This is consistent with our understanding of cluster evolution. Through the natural diffusion of energy from core to halo, clusters naturally evolve toward more compact configurations (r_c decreases over time; see, e.g., Heggie & Hut 2003, for an overview). Clusters with smaller r_v have shorter relaxation times and thus approach more

[8] We also compared our models to the observed clusters in Harris (1996) and found similarly good agreement. We show comparisons to Baumgardt & Hilker (2018) simply because that analysis quotes total cluster masses directly (as opposed to V-band magnitudes), which circumvents the need to assume a mass-to-light ratio in order to obtain cluster masses.

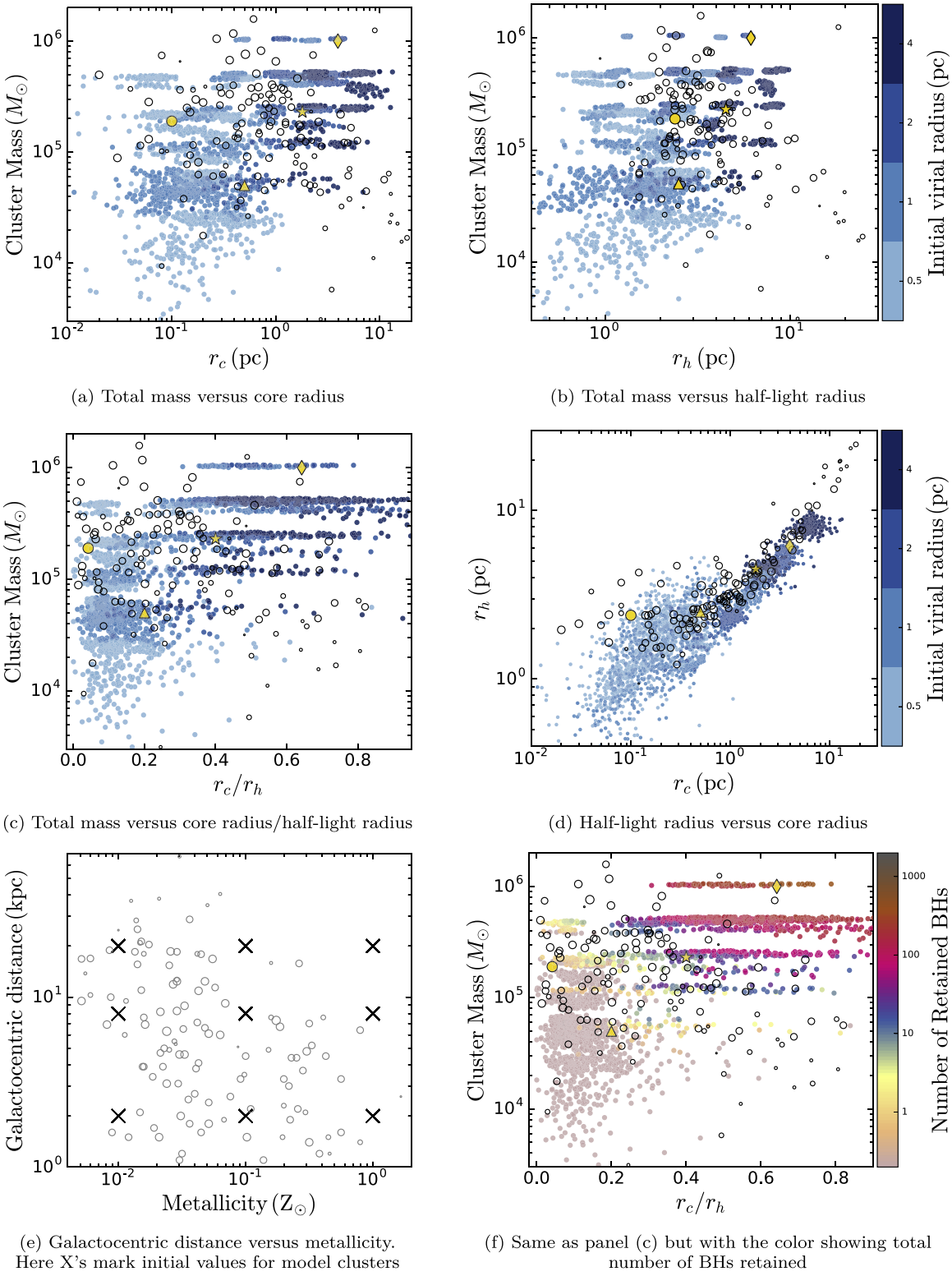

(a) Total mass versus core radius

(b) Total mass versus half-light radius

(c) Total mass versus core radius/half-light radius

(d) Half-light radius versus core radius

(e) Galactocentric distance versus metallicity. Here X's mark initial values for model clusters

(f) Same as panel (c) but with the color showing total number of BHs retained

Figure 2. All late-time snapshots (t = 10–13 Gyr) for model clusters (blue points) compared to observational data for MW clusters (black points), taken from Baumgardt & Hilker (2018). The size of each black point corresponds to the integrated V-band magnitude of each cluster (Harris 1996) such that the larger symbols denote clusters that are best observed. In panels (a)–(d), the various shades of blue show, from light to dark, models with increasing initial virial radii, from r_v = 0.5 to 4 pc. In panel (f), the color scheme denotes the total number of retained BHs. The panels compare various observed features, including total cluster mass, core radius (r_c), half-light radius (r_h), metallicity, and Galactocentric distance (as labeled in each of the figure subcaptions). The four gold-colored symbols in the various panels correspond to the locations of the four "characteristic" clusters described in the text.

compact configurations relatively quickly. Thus, by varying r_v (here, from 0.5 to 4 pc), the full distribution of cluster core radii is naturally captured. This same result was demonstrated in Kremer et al. (2019a) for a much smaller set of models of fixed particle number and metallicity. Here, we demonstrate this result for a much broader set of cluster properties.

Furthermore, the relation between initial r_v and the evolution of a cluster's core crucially depends on the cluster's BH population. When a large number of BHs are present, the internal dynamics of the BH subsystem introduces a substantial energy source that supports the core of the cluster against its natural tendency to collapse. As the BH population is depleted through dynamical ejection of BHs in binary-mediated encounters within the core, the energy generated via this "BH burning" process gradually becomes less dynamically important. Ultimately, the core is no longer adequately supported, and the cluster undergoes core collapse, at which point the core is supported by "burning" of stellar binaries (Chatterjee et al. 2013). The depletion rate of the BHs is determined by the initial r_v: smaller r_v corresponds to higher BH interaction rates and therefore more rapid BH depletion (Kremer et al. 2019a). Therefore, we expect the cluster models with larger initial r_v to retain more BHs at present and, as a consequence, have larger cores. This exact result is shown in panel (f) of Figure 2. We detail the evolution of BH populations across all models in Section 3.2.

Figure 2 shows that our model clusters span effectively the full parameter space of the observed MW GCs. That being said, two regions of the MW cluster parameter space are visibly less well covered than others: the most massive and most compact clusters (i.e., upper left corner of panel (c)) and the least massive and least compact clusters (i.e., lower right corner of panel (c)). The poor coverage in these regions can be attributed to the intentionally chosen limits in our simulation grid. More massive and compact cluster simulations are more expensive computationally. As shown in Figure 2, the most massive clusters observed in the MW are reproduced best by simulations with initial $N = 3.2 \times 10^6$. It is beyond the present scope of CMC to run such massive simulations with sufficiently small initial r_v (0.5 pc) to reproduce the most massive and most compact GCs observed in the MW. Not only are such simulations extremely computationally expensive, but, as discussed in Section 2.3, these high-density models also feature frequent collisional runaway episodes, producing massive stars (and ultimately BHs) that CMC in its present form is ill-equipped to handle accurately.

On the other hand, the least massive and least compact clusters (lower right corners of panels (a), (b), (c), and (e) and upper right corner of panel (d)) are best captured by simulations with low N and initial sizes outside the current range of our grid (i.e., $r_v = 8$ pc or larger). Although such models are relatively inexpensive computationally, we neglect to include them here simply because these diffuse low-mass clusters constitute a low fraction of the total mass of the MW GC system and also because these clusters straddle the boundary between GCs and open clusters, the latter of which are well known to be better suited for direct N-body modeling (e.g., Aarseth 2003, for a review). With these considerations in mind, and in order to avoid fine-tuning of our simulation grid to match specific regions of the parameter space, we simply acknowledge relatively sparse coverage in the aforementioned regions and reserve more detailed studies of these regions for future work.

The total number of models (148), the total final mass of the complete set (roughly $3 \times 10^7\,M_\odot$), and the fraction of clusters that are core-collapsed at the end of the simulation (roughly 20%) are all roughly consistent with the respective values of the full population of MW GCs. These agreements between models and observations motivate the use of this model set to explore various features of the MW cluster population, as is done in Sections 4–8.

3.2. Black Hole Populations

In Figure 3, we show the total number of retained BHs versus time for all models with $R_{\rm gc} = 20$ kpc (a fixed value here for simplicity). The four rows show, from top to bottom, models increasing in N, and the three columns show, from left to right, models increasing in Z. As in Figure 2, curves of lighter to darker shades of blue indicate increasing r_v.[9]

In all models, the total number of BHs decreases throughout the lifetime of the cluster. The differences in the total number of BHs formed, the total number of BHs retained at simulation end, and the depletion rate of the BH population throughout the simulation can be attributed to the modulation in N, r_v, and Z. We discuss each in turn below.

Initial particle number (N): For models of fixed r_v and Z, the initial number of stars determines the total number of BHs that form in the cluster through stellar evolution. Because we adopt a binary fraction of 5% for all models in this study, stellar evolution here refers primarily to *single*-star evolution. As Figure 3 shows, the total number of BHs retained in the cluster at birth scales roughly linearly with N: as N is doubled, the initial number of retained BHs roughly doubles.

Metallicity (Z): For the purposes of BH populations, metallicity determines the mass lost through stellar winds in high-mass stars, which, in turn, determines the masses of the BHs at formation. As described in Section 2, we adopt the wind mass-loss prescriptions of Vink et al. (2001). In short, higher metallicity means higher line-driven winds, resulting in less massive stars just before collapse to a BH. Thus, higher-metallicity clusters yield lower-mass BHs. Because our BH formation prescriptions assume that, in general, lower-mass BHs receive larger natal kicks (because lower-mass BHs form with less fallback; see Section 2.1 and Morscher et al. 2015), a larger fraction of low-mass BHs formed in higher-metallicity clusters are ejected promptly at formation. Thus, higher-metallicity clusters will retain fewer BHs at birth, as can be seen by comparing columns 1–3 in Figure 3.

Initial virial radius (r_v): The initial r_v affects BH retention in two ways: immediately at time of BH formation ($t \lesssim$ tens of megayears), and subsequently over a long dynamical timescale ($t \sim 1$ Gyr). Clusters with larger r_v have shallower potential wells ($U \sim GM_{\rm tot}/r_v$). Thus, a larger fraction of BHs will be ejected promptly from their host cluster through natal kicks (see Section 2 for details of our BH natal kick prescriptions). This effect is most pronounced for higher metallicities (right column of Figure 3), for the reasons discussed above. As a side note, the initial retention fraction of NSs also varies with r_v in the same manner: more NSs are retained at birth in clusters with smaller r_v.

Once the population of BHs forms in a cluster through stellar evolution, the BHs rapidly mass-segregate to the cluster core. As described in Kremer et al. (2019a), smaller r_v means shorter relaxation time, which means quicker mass segregation. In addition, smaller r_v also leads to higher central densities, which leads to a higher rate of superelastic strong encounters, leading to quicker depletion of BHs via dynamical ejections. For fixed

[9] Note that the model with $r_v = 0.5$ pc is absent from the bottom left panel. As discussed in Section 2, this particular model undergoes collisional runaway within the first few megayears. Treatment of this process is beyond the scope of the present version of CMC, so we exclude this model from our study.

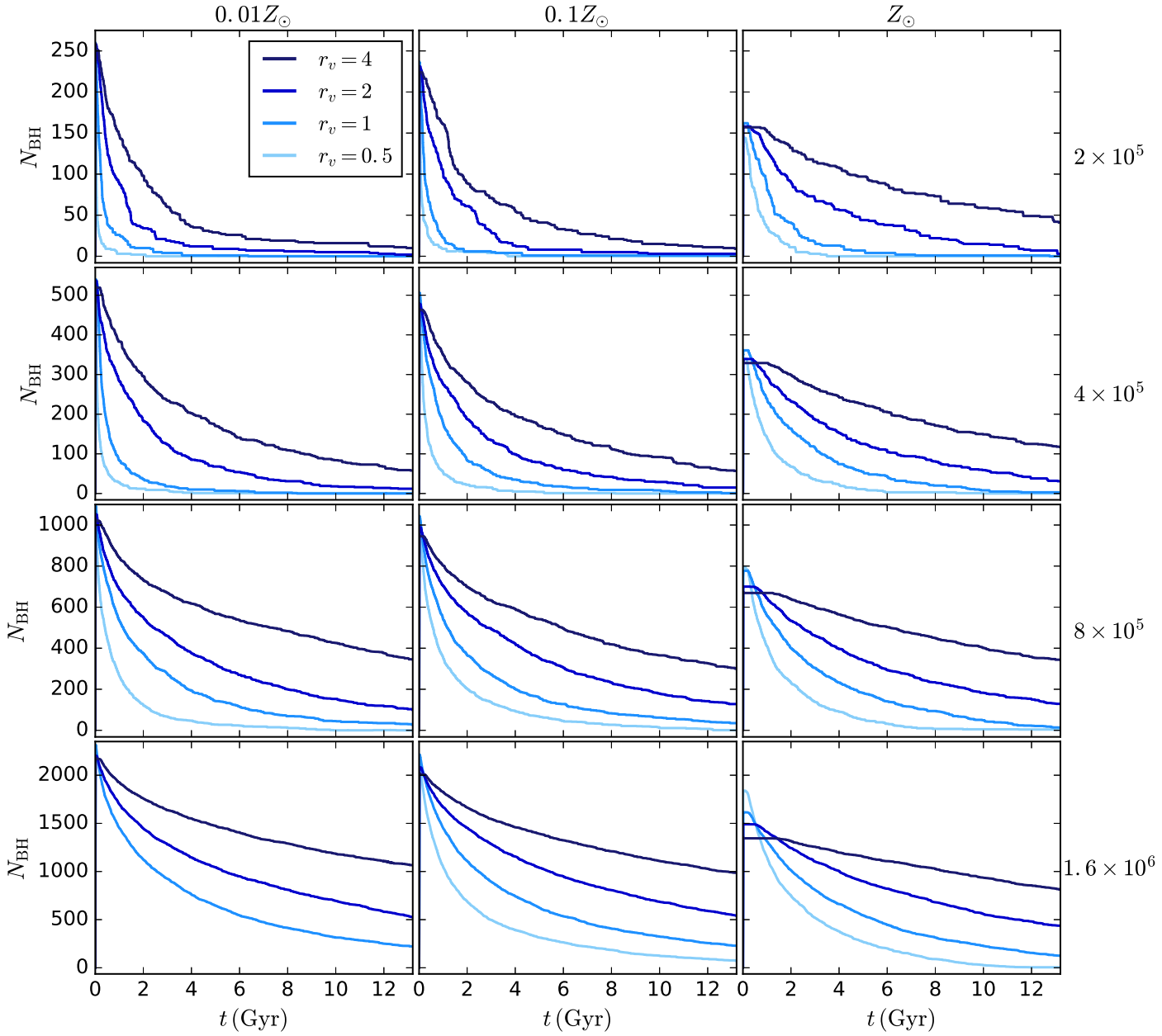

Figure 3. Total number of retained BHs vs. time for all models with $R_{\rm gc} = 20$ kpc. The three columns show models of different metallicity (from left to right, $Z = 0.01$, 0.1, and 1 $Z_\odot$), and the four rows show models of different initial particle number (from top to bottom, $N = 2 \times 10^5$, 4×10^5, 8×10^5, and 1.6×10^6. As in Figure 2, lighter to darker shades of blue indicate increasing initial r_v.

N and Z, clusters with lower r_v (lightly shaded blue curves in Figure 3) have higher initial densities and shorter relaxation times and therefore eject their BHs relatively quickly compared to models with higher r_v (darkly shaded blue curves).

3.3. Radial Profiles

In Figure 4, we show cumulative radial distributions at three separate cluster ages ($t = 0.1$, 1, and 10 Gyr). For simplicity, we limit this figure to clusters with $N = 8 \times 10^5$, $R_{\rm gc} = 8$ kpc, and $Z = 0.01\ Z_\odot$ but emphasize that all models exhibit similar behavior. From top to bottom, we show models 15, 51, 87, and 123 (see Table 6), which have initial $r_v = 0.5$, 1, 2, and 4 pc, respectively. In each panel, we show radial distributions for all different stellar populations: main-sequence (MS) stars (yellow), giants (orange), WDs (blue), NSs (red), and BHs (black).

The vertical dashed gray lines mark the core radius of each cluster snapshot, as defined in Section 2.3. For a fixed cluster age (i.e., a single column in Figure 4), models with smaller r_v typically have smaller core radii than models with larger r_v. This is also a direct consequence of the BH burning mechanism described previously. Furthermore, if the number of BHs (black curves) is compared across models, we see that the models with the smallest core radii at a specific time also have, on average, the fewest BHs.

As seen in all panels, the innermost regions of clusters are typically dominated by the BHs (in some cases, mixed with MS stars, particularly when the MS stars are bound to BH binary companions). This is a consequence of mass segregation and is consistent with predictions from a number of recent analyses (e.g., Kulkarni et al. 1993; Sigurdsson 1993; Breen & Heggie 2013;

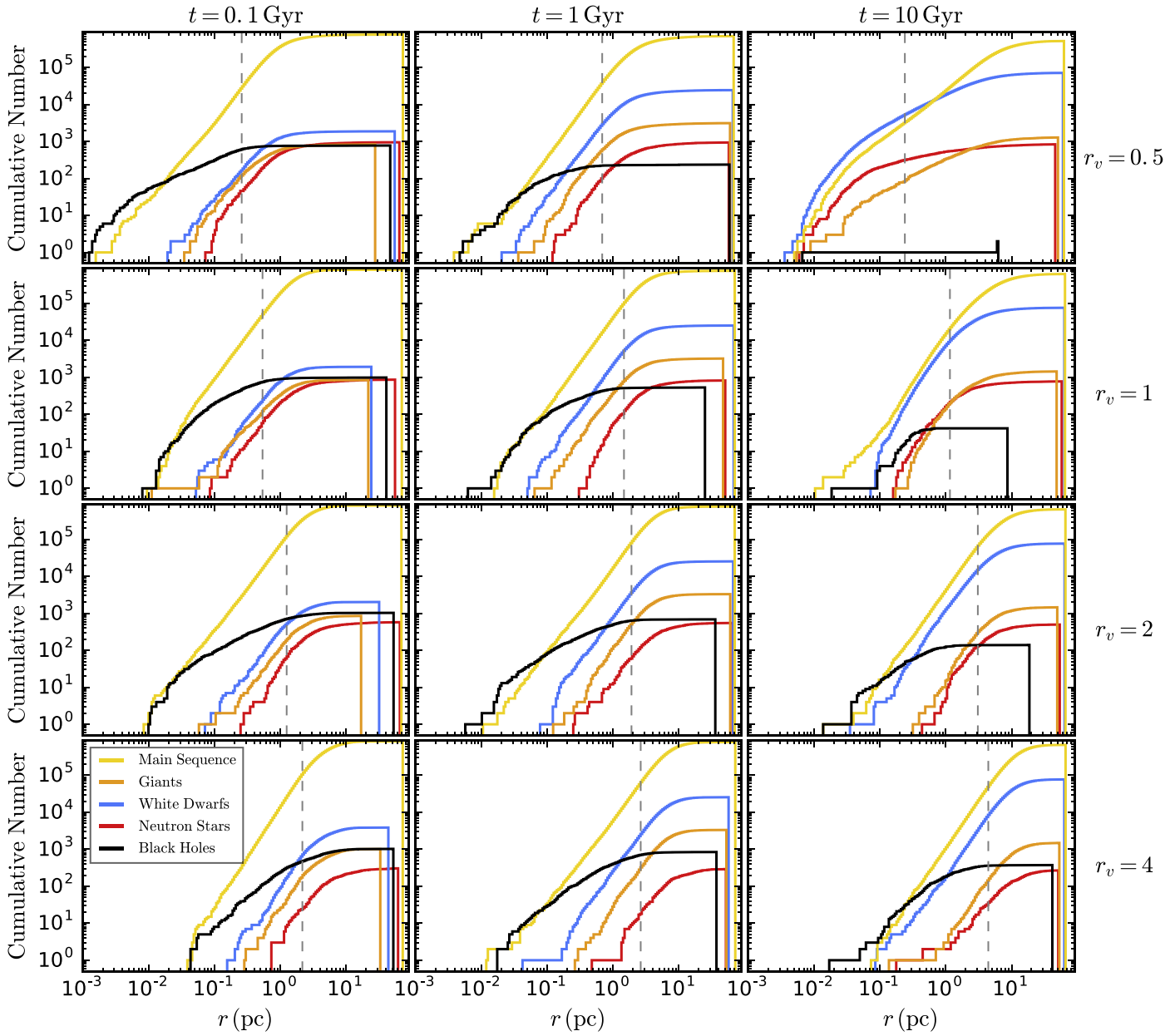

Figure 4. Cumulative radial distributions of all stellar populations (colors denoted in legend) for three cluster snapshots in time (from left to right, $t = 0.1$, 1, and 10 Gyr). From top to bottom, we show clusters of varying initial virial radius, r_v. All other initial cluster parameters are fixed. The vertical dashed gray lines mark the core radius of each cluster snapshot. Note that models with smaller initial r_v have fewer BHs and smaller core radii than their large-r_v counterparts.

Morscher et al. 2015; Chatterjee et al. 2017b; Askar et al. 2018; Kremer et al. 2019a). Notably, this is not the case for the $r_v = 0.5$ and $r_v = 1$ models at $t = 10$ Gyr. As described in Section 3.2, the dynamical clock of a cluster is determined by the initial r_v. Clusters with smaller initial r_v are more dynamically evolved by $t = 10$ Gyr and thus have ejected a larger fraction of their BHs compared to models with larger r_v. For the $r_v = 0.5$ and $r_v = 1$ models, only 2 and 30 BHs (out of roughly 1000 total retained in the clusters at birth) remain at $t = 10$ Gyr. These BH populations no longer provide sufficient energy to the cluster through BH burning to prevent lower-mass luminous stars from entering the cluster's innermost region. The "collapse" of the cluster's core is most prominently seen in the $r_v = 0.5$ model, as evidenced by both the core radius (dashed gray line) and the visible shift in the distribution of non-BH populations. Indeed, as discussed in Section 3.4, this particular cluster has a surface density profile representative of a "core-collapsed" cluster at the conclusion of the simulation.

The same effect is apparent in the $r_v = 1$ model, where, at $t = 10$ Gyr, the MS stars have begun to infiltrate the cluster's innermost region, although not as prominently as in the $r_v = 0.5$ model. This is expected: the transition from a BH-dominated cluster with a large core to a core-collapsed cluster is smooth (for illustration of this point, see Figure 5). This means that as the number of BHs decreases, the core becomes increasingly dominated by MS stars (the exact number of MS stars is dependent on statistical fluctuations governed by the chaotic strong encounters in the core). The MS star distributions shown in the four $t = 10$ Gyr panels in Figure 4 show clearly this transition.

Several key points can also be made regarding the NS populations in Figure 4 (red curves). Through the BH burning

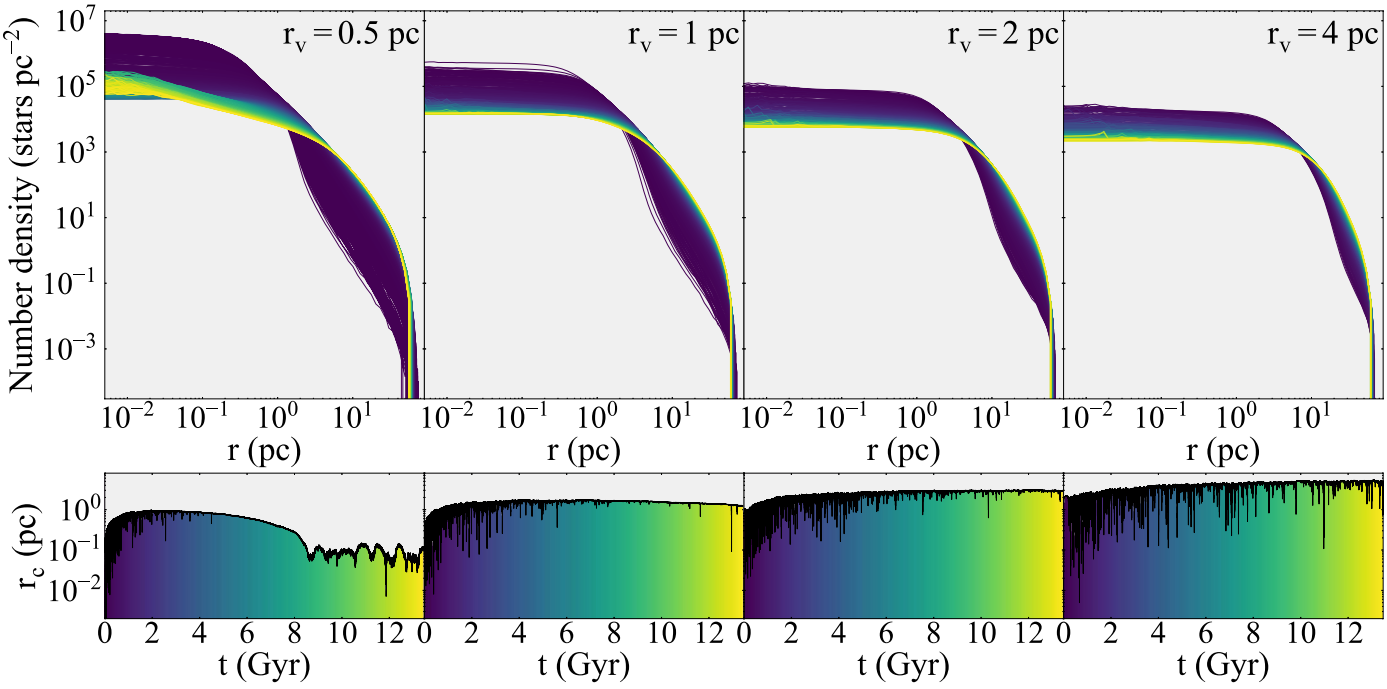

Figure 5. Top: stellar number surface density profiles throughout time for models with different initial virial radii (from left to right: models N8-RV0.5-RG8-Z0.01, N8-RV1-RG8-Z0.01, N8-RV2-RG8-Z0.01, and N8-RV4-RG8-Z0.01). Bottom: time evolution of the theoretical core radii of these models. Model N8-RV0.5-RG8-Z0.01 is a prototypical example of a cluster that would be core-collapsed by the present day. In contrast, models N8-RV2-RG8-Z0.01 and N8-RV4-RG8-Z0.01 represent clusters whose core collapses have been halted. Model N8-RV1-RG8-Z0.01 represents clusters that have only barely avoided core collapse by the present day. Colors denote cluster age. The three panels in the video show the number density profile, core radius, and total number of BHs, respectively, as they evolve in time. The video begins at $t = 0$ Gyr and ends at ≈13.3 Gyr. The real-time duration of the video is 61 s.

(An animation of this figure is available.)

mechanism discussed previously, mass segregation of NSs is prevented when significant numbers of BHs are present in the host cluster core (e.g., Banerjee 2018; Fragione et al. 2018c; Ye et al. 2019). As a result, NSs tend to be found at relatively large radial offsets compared to the BHs. Furthermore, unlike the BHs, the total number of NSs remains roughly constant across the three snapshots in time shown for each cluster in this figure. This is simply because NSs remain relatively inactive dynamically compared to the BHs that preferentially occupy the densest regions of their host clusters, where high rates of strong encounters lead to rapid depletion of BHs via dynamical ejections. The notable exception is the $r_v = 0.5$ model at $t = 10$ Gyr (top right panel), where NSs occupy the cluster's innermost regions. Here, because this cluster has already ejected all but two of its BHs, NSs are the most massive stellar population remaining in the cluster and therefore have begun to efficiently mass-segregate to the core. This is in line with the predictions made in Ye et al. (2019), which noted that only in the absence of BHs (i.e., in core-collapsed clusters) will a significant fraction of NSs be found in the core of a cluster. As Ye et al. (2019) noted, this sets the stage for dynamical formation of millisecond pulsars (MSPs), and we thus expect an anticorrelation between the number of MSPs in a cluster and the total number of BHs. We return to the topic of MSPs in Section 5.

Several similar points can be made for the WD populations (blue curves). Unlike NSs, the number of WDs increases throughout the lifetime of the cluster, simply due to stellar evolution as less massive stars are converted to WDs at later times. Like the NSs, WDs are generally found outside the cluster's core until the BH population is sufficiently depleted. However, in core-collapsed clusters like the $r_v = 0.5$ pc model shown here, WDs can dominate the core by number. Thus, core-collapsed clusters are likely ideal factories for dynamical formation of WD binaries, SNe Ia, and CVs. We discuss several of these possibilities in Section 6.

3.4. Core-collapsed versus Non-core-collapsed Clusters

Figure 5 illustrates how initial virial radius and BH burning affect the density profile in clusters. In the top row of panels, we show the number density profile at each snapshot in time for the same four models shown in Figure 4. From left to right, we show models increasing in r_v. In the bottom row, we show the evolution of (theoretical) core radius as a function of time. The snapshot time of each profile is colored from dark purple (early times) to yellow (late times), as indicated by the color spectrum in the bottom panels.

In all cases, the core radius expands at early times ($t \lesssim 1$ Gyr) owing to mass loss associated with evolution of high-mass stars, as well as BH burning once a BH core forms. The subsequent evolution varies from model to model, depending on r_v. For $r_v = 4$ pc, the core continues to expand throughout the cluster's evolution as a result of prolonged BH burning; as seen in Figures 3 and 4, this model retains a large population of BHs throughout its entire lifetime. This is in stark contrast to the $r_v = 0.5$ pc case, where the BH population is rapidly depleted (less than 10% of the initial BH population is still retained in the cluster by $t \approx 4$ Gyr). In this case, the core radius begins to contract relatively, only steadying out once binary burning (involving regular stellar binaries) begins at $t \approx 8$ Gyr. Comparing the number density profiles, we see that where the $r_v = 4$ pc case retains a King profile through the entire simulation, the

$r_v = 0.5$ pc model clearly reaches (and maintains) a core-collapse architecture once binary burning has begun.

In the electronic version of the manuscript, we also include animated illustrations of the four models show in Figure 5. In the left panel of these animations, we show the cluster luminosity profiles as they evolve in time. In the upper right corner of this panel, we indicate the current cluster age, as well as the total number of retained BHs and the maximum BH mass at this age. Note that the maximum BH mass decreases as the cluster evolves (see, e.g., Morscher et al. 2015, for detailed discussion of this point). Note also that at early times, the maximum BH mass may exceed the $40.5\,M_\odot$ limit from the pulsational pair-instability supernova. prescriptions described in Section 2. These massive BHs are formed through either repeated BH mergers (e.g., Rodriguez et al. 2018b) or stellar collisions (see Section 7). In the middle panel of the animations, we show the theoretical core radius as it evolves over time, and in the right panel, we show the total number of retained BHs versus time.

3.5. Hertzsprung–Russell Diagrams

In Figure 6, we show H-R diagrams for the four clusters seen in Figures 4 and 5 at $t = 12$ Gyr. We plot here the bolometric luminosity versus temperature of all stars, which are both given by SSE (see Hurley et al. 2000, for further details).

The location of the MS turnoff (defined as in Weatherford et al. 2018) is identical in all four panels, as expected given that these clusters have identical metallicities and ages. One noticeable difference between the four clusters here concerns the BSs (blue circles), the population of stars lying leftward (hotter) and upward (brighter) of the MS turnoff (e.g., Sandage 1953). We discuss BSs in more detail in Section 8.

4. Low-mass X-Ray Binaries

X-ray sources have been well observed in GCs dating back to the 1970s (Clark 1975; Heinke 2010). It is understood that various dynamical processes relevant in GCs lead to formation of low-mass X-ray binaries (LMXBs) at a significantly higher rate per unit stellar mass in clusters compared to isolated binary evolution in the Galactic field (e.g., Clark 1975). For several decades, the LMXBs observed in GCs came exclusively in the NS accretor variety. In fact, the conspicuous absence of BH LMXBs in clusters was traditionally used to argue that clusters have very few (if any) stellar-mass BHs at present (e.g., Kulkarni et al. 1993).

This picture has begun to change within the past 10 years as the first stellar-mass BH candidates have been identified in both Galactic and extragalactic GCs, primarily as accreting LMXBs (Maccarone et al. 2007; Strader et al. 2012; Chomiuk et al. 2013; Miller-Jones et al. 2015; Shishkovsky et al. 2018). The discovery of these BH LMXBs, as well as the detached BH–MS binaries found in NGC 3201 by the MUSE survey (Giesers et al. 2018, 2019), have motivated more detailed studies of how BH binaries may form in GCs. For example, Ivanova et al. (2010) noted that ultracompact BH LMXBs with degenerate donors (similar perhaps to the X-ray source observed in 47 Tuc; Bahramian et al. 2017; Church et al. 2017) may form as a result of BH–giant collisions. Later work by Kremer et al. (2018a) noted that accreting BH binaries can form through exchange encounters at rates consistent with the number of BH X-ray sources observed in clusters to date.

In Table 7 in the Appendix, we show the average numbers of NS and BH binaries in each model for snapshots with ages in the range of 10–13 Gyr. We distinguish between various types of luminous companions (MS stars, giants, and WDs) and also between those binaries that are accreting and detached. Here, we define accreting binaries as in BSE, where the donor star must fill its Roche radius in the zero-eccentricity limit: $R > R_L$, where R is the stellar radius and

$$R_L = a\frac{0.49q^{2/3}}{0.6q^{2/3} + \log(1 + q^{1/3})}, \quad (3)$$

where a is the binary semimajor axis and q is the mass ratio. In reality, an eccentricity-dependent definition for the onset of Roche lobe overflow may be more appropriate (e.g., $R > R_L(1-e)$). However, as shown in Kremer et al. (2018a), such a definition is unlikely to change the results significantly in the context of forming LMXBs.

In Table 1, we show the total numbers of BH and NS binaries (both accreting and detached) in the four simulations that characterize common cluster types observed in the MW, as described in Section 3.1.

Although we reserve a thorough study of BH/NS binary formation and their potential observability as X-ray sources for a future study dedicated specifically to the topic, we comment here on two general trends. First, the number of accreting BH binaries scales very weakly with cluster properties, consistent with several recent analyses (e.g., Chatterjee et al. 2017a; Kremer et al. 2018a). In order for BHs and luminous stars to form binaries through dynamical encounters, the two populations must overlap within a "mixing zone" in the cluster's core. The dynamical encounter rate between BHs and luminous stars within this zone is approximately $n_{\rm LC}\Sigma v_\infty N_{\rm BH}$, where $n_{\rm LC}$ is the typical number density of luminous companions and v_∞ is the typical relative velocity at infinity in the mixing zone. Σ is the cross section for encounters and $N_{\rm BH}$ is the total number of BHs in the mixing zone. As discussed in Section 3, $N_{\rm BH}$ determines the density of luminous stars within clusters through BH burning; as $N_{\rm BH}$ increases, $n_{\rm LC}$ decreases. Thus, we expect the total formation rate of BH–LC binaries to remain roughly constant with $N_{\rm BH}$, as suggested by Table 1 and as described in detail in Kremer et al. (2018a).

However, no such self-regulating dynamical process is expected for NS binaries; formation of these systems is expected to depend simply on the density of the cluster core, and thus on $N_{\rm BH}$. Among clusters with comparable mass, those with fewer BHs have relatively dense cores (see Section 3) and therefore form more NS binaries. This is analogous to the results of Ye et al. (2019), which showed that MSP formation also anticorrelates with the total BH population size. We further discuss pulsars in the following section.

5. Pulsars

In excess of 150 millisecond radio pulsars have been observed in various GCs in the MW (for a recent review, see Ransom 2008). MSPs are generally thought to form when an old, slowly spinning NS is spun up through mass transfer from a Roche-lobe-filling binary companion (e.g., Rappaport et al. 1995; Tauris et al. 2012). Thus, MSPs are likely intimately linked to NS LMXBs (see Section 4), with the former being direct descendants of the latter. As with LMXBs, the MSP formation rate is expected to be more pronounced in GCs, due

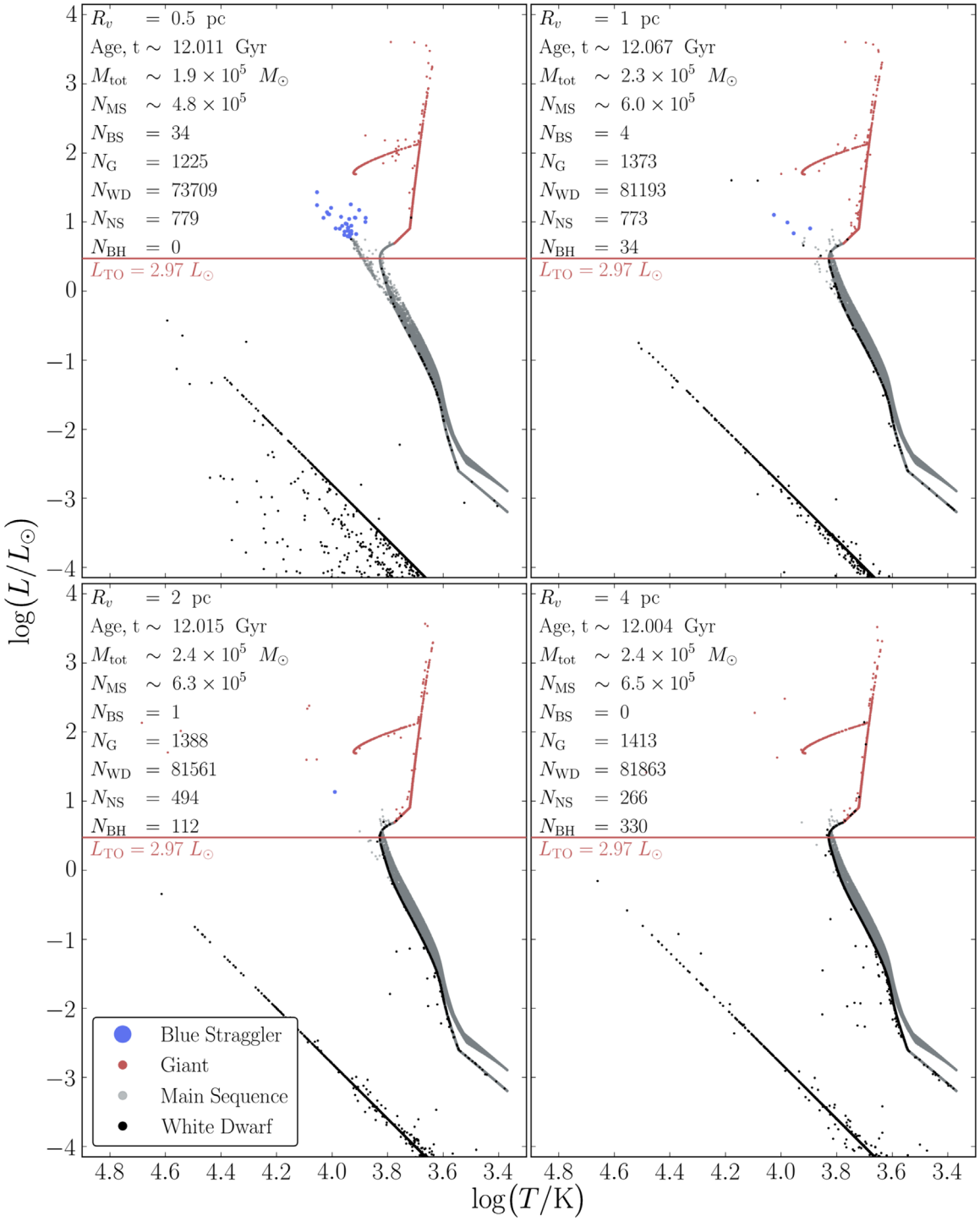

Figure 6. H-R diagrams of the four clusters shown in Figures 4 and 5. Each dot represents a single or binary star (all binaries are considered unresolved), with BSs colored in blue, giants in red, the MS stars in gray, and any single or binary containing a WD in black. Note that for binaries, the summed luminosity and luminosity-weighted mean temperature are plotted. To select BSs, the MS turnoff is first defined as the luminosity, L_{TO}, corresponding to the point on the MS branch with the highest median temperature, T_{TO}. L_{TO} is indicated by the red horizontal line. BSs are then defined as any MS single (or binary containing an MS star) where the above-defined luminosity and temperature exceed $L_{BS} = 2 \cdot L_{TO}$ and T_{TO}. For a more detailed view, see Figure 11.

to dynamical processes, relative to isolated binary evolution (e.g., Clark 1975; Hut et al. 1992; Bahramian et al. 2013; Ye et al. 2019).

Recently, Ye et al. (2019) showed that MSP formation also directly relates to a cluster's stellar-mass BH retention. When a large population of BHs is present, BH burning heats the cluster's core, delaying core collapse, regulating the central density, and, of relevance to the formation of MSPs, limiting the dynamical encounter rate for NSs. As a cluster's BH population becomes depleted, NSs grow more dynamically active, ultimately increasing the MSP formation rate (see also Fragione et al. 2018c). Hence, as shown in Ye et al. (2019), we expect an anticorrelation between BH number and MSP number in clusters of equal mass. GCs with the fewest BHs

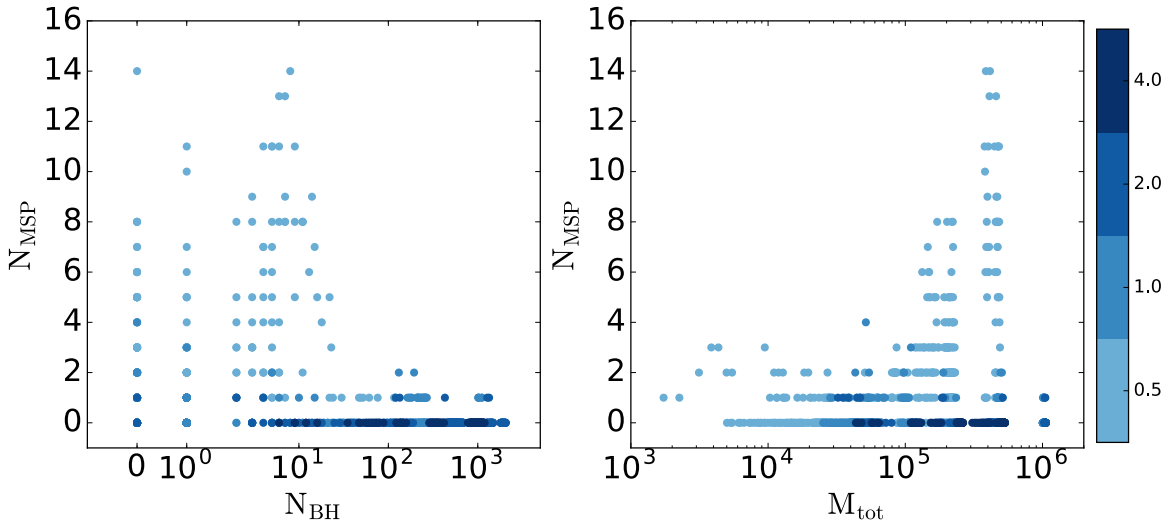

Figure 7. Number of MSPs vs. number of BHs (left panel) and the total cluster mass (right panel) in all model snapshots in the range of 10–13 Gyr.

Table 1
Black Hole and Neutron Star Binaries in Four Representative Clusters

	$M_{tot}(M_\odot)$	Total BHs	Det. BH Binaries	Acc. BH Binaries	Total NS	Det. NS Binaries	Acc. NS Binaries
Typical	2.3×10^5	105–140	0–5	0–1	494–498	0–1	1
Core-collapsed	1.9×10^5	0–3	0–2	0	751–837	7–14	4–6
Low-mass	5×10^4	0–3	0–1	0	25	0	0
High-mass	10^6	1812–2061	1–7	0-1	4157–4190	3–4	2

Note. Ranges of total number of BH and NS binaries with luminous companions in both detached and accreting configurations for all snapshots in the range of 10–13 Gyr for four representative clusters. Here, "typical" denotes model N8-RV2-RG8-Z0.01 (a non-core-collapsed cluster with mass, metallicity, and Galactocentric position typical for MW clusters), "core-collapsed" denotes model N8-RV0.5-RG8-Z0.01, "low-mass" denotes model N2-RV2-RG8-Z0.01, and "high-mass" denotes model N32-RV2-RG20-Z0.01.

(i.e., core-collapsed clusters) are expected to host the largest numbers of MSPs.

Ye et al. (2019) controlled BH retention in cluster models by varying the magnitude of BH natal kicks, a proxy for more physically motivated processes that may determine BH retention such as the cluster's initial r_v. In this analysis, we expand on the results of Ye et al. (2019) by modulating BH retention by varying r_v while fixing the BH natal kick physics, and also by exploring pulsar formation in cluster models with a wider range in particle number and metallicity. All physics relevant to the formation of pulsars and MSPs is the same here as in Ye et al. (2019). Briefly, we randomly select NS spin periods and magnetic field strengths using values consistent with the young pulsars observed in the MW ($B \sim 10^{12}$ G and $P > 30$ ms). All NSs form as young pulsars in our models. MSPs can form through stable mass transfer in binaries. We assume that the spin period evolves through dipole radiation and that the magnetic fields of single or detached pulsars decay exponentially with time (Kiel et al. 2008). For pulsars that have been through mass transfer, we assume the "magnetic field burying" scenario and lower the pulsars' magnetic fields according to how much material is accreted (Kiel et al. 2008). These pulsars exhibit faster spins due to angular momentum transfer (Hurley et al. 2002).

In the left panel of Figure 7, we show the number of retained MSPs versus the total number of retained BHs for all model snapshots with age in the range 10–13 Gyr. Each scatter point indicates a distinct cluster snapshot. As in earlier figures, shades of blue denote the cluster's initial r_v, with lighter to darker shades indicating increasing r_v. For reference, the average numbers of pulsars and MSPs retained at late times in each model are also listed in Table 9.

Comparing specifically to Figure 4 of Ye et al. (2019), we see a similar trend: clusters with smaller BH populations are capable of producing larger numbers of MSPs (here, up to 14), while clusters with large numbers of BHs are unlikely to contain more than one to two MSPs. As Figure 7 shows, this relation is determined primarily by the initial r_v. Models with $r_v = 0.5$ pc (light blue) that have the highest central densities at late times (see Figures 4 and 5) generally produce more MSPs than models with larger values of r_v.

For models with few BHs, we predict a slightly smaller number of MSPs compared to Ye et al. (2019). For models with similar N (8×10^5) and metallicity ($0.1Z_\odot$), we find up to roughly seven MSPs in models with zero to one BH, compared to up to roughly 16 for similar models in Ye et al. (2019). This makes sense given the differences in the two methods. In the limiting case of Ye et al. (2019), nearly all BHs are ejected from the cluster at birth through natal kicks. For such a cluster, BH burning is nonexistent from the outset, and the cluster's core quickly collapses. This allows dynamical processes relevant to pulsar formation to operate over essentially the full lifetime of the cluster, yielding many more opportunities for pulsar and MSP formation. However, when the BH natal kick physics is fixed, as in this analysis, the NSs must first wait for the BH population to be sufficiently depleted before the core

Table 2
Pulsars in Four Representative Clusters

	$M_{\rm tot}$ ($M_\odot$)	Total NS	Pulsars	MSPs
Typical	2.3×10^5	494–498	1	1
Core-collapsed	1.9×10^5	751–837	4–13	4–7
Low-mass	5×10^4	25	0	0
High-mass	10^6	4157–4190	3–4	3

Note. Ranges of total number of NSs, pulsars, and millisecond pulsars for all snapshots in the range of 10–13 Gyr for four representative clusters, as defined in Table 1.

can collapse. As shown in Figure 5, for $N = 8 \times 10^5$, this takes roughly 8 Gyr. Because clusters with smaller total mass (total N) have shorter relaxation times (Equation (1)), models with smaller N will tend to core-collapse sooner; however, even small-N clusters must wait some characteristic length of time before NSs become dynamically active in the core. Hence, models in the present study spend a much shorter portion of their life in a core-collapsed state relative to those in Ye et al. (2019), limiting the number of pulsars compared to those earlier models. However, we do stress that this effect amounts to only a factor of roughly 2. Most importantly, the general trend between MSP number and BH number is preserved.

In Table 2, we show the range in total numbers of pulsars and MSPs in the same four characteristic clusters shown in Table 1. Generally, the numbers quoted in this table are in rough agreement with observations of clusters of comparable total mass (reviewed in Ransom 2008). We predict up to 13 pulsars in core-collapsed clusters with total mass comparable to the characteristic core-collapsed model shown in Table 2 ($M_{\rm tot} \approx 2 \times 10^5$), e.g., NGC 6752 (five observed pulsars). In our four massive simulations, we identify up to eight pulsars, which admittedly is less than the number, for example, in 47 Tuc, which has comparable total mass to our massive models. However, 47 Tuc has a very high central density, and previous work has predicted that this cluster likely retains a fairly small population of BHs (Weatherford et al. 2018). As described in Section 2, the most massive branch of our parameter space (initial $N = 3.2 \times 10^6$) does not extend to sufficiently small initial r_v to produce a core-collapsed cluster at late times, simply due to computational limitations. However, Ye et al. (2019) modeled a single massive cluster that reached central densities comparable to 47 Tuc at late times (by assuming that all BHs are ejected at birth through natal kicks as a computationally inexpensive proxy for efficient BH ejection associated with small r_v) and showed that, in this limiting case, the number of model pulsars is roughly consistent with the observed number in a cluster like 47 Tuc. We direct the reader to Ye et al. (2019) for more detailed discussion on this topic.

6. White Dwarfs

WDs are expected to be abundant in GCs and, as shown in Figure 4, may even be the dominant stellar population within the cores of some clusters at late times. Unlike BH and NS populations, which are expected to form early in the evolution of their host cluster ($t_{\rm formation} \lesssim 100$ Myr) and then slowly decrease throughout the remainder of the cluster lifetime (see, e.g., Figure 4), WDs continue to form throughout the full lifetime of their host cluster such that the number of WDs increases with time.

To handle WD formation and evolution, we adopt the treatment implemented in BSE (for details, we direct the reader to Hurley et al. 2002). In Column (12) of Table 6, we show the total number of WDs retained in each simulation at simulation end. The number of WDs at late times generally varies from roughly 10^4 to over 10^5, depending on the various simulation parameters. As can be seen from Table 6, the WD number depends most sensitively on the total number of stars (N), with weaker dependence on initial r_v and metallicity.

When WDs interact with other stars, through either binary evolution or various dynamical processes, WDs have been associated with a number of high-energy astrophysical phenomena such as CVs (Knigge 2012; Ivanova et al. 2006) and SNe Ia (e.g., Shara & Hurley 2002). In the following subsections, we briefly explore the processes leading to such events in our model set and discuss various implications.

6.1. Accreting White Dwarf Binaries

WDs that are stably accreting material from a binary companion constitute a number of different astrophysical sources. One type of accreting WD binary is the CV, a system in which a WD accretes material from a donor on the MS (e.g., Warner 1995; Knigge et al. 2011). As their name suggests, CVs are variable stars characterized by novae or nova-like outbursts. For some CVs, where the WD accretor has a strong magnetic field, magnetic activity leads to specific classes of novae. Closely related to the CVs are the AM CVn systems, compact binaries (orbital periods $\lesssim$1 hr) where a WD accretes hydrogen-poor material from either an He WD or naked He star (e.g., Paczyński 1967; Marsh et al. 2004; Nelemans 2005). Depending on the various features of the system (i.e., accretion rate, mass ratio, etc.), some AM CVn may be observed as soft X-ray sources (e.g., Nelemans et al. 2004) and, for mHz GW detectors like LISA, as GW sources (e.g., Nelemans et al. 2004; Kremer et al. 2017).

Accreting WD binaries are valuable tools for studying important aspects of binary evolution, including mass transfer processes, super-Eddington accretion, and common envelope physics. In the coming decades, WD binaries will play an emerging role in GW astronomy, as WD binaries will be the most abundant source for the upcoming low-frequency GW observatory, LISA (Amaro-Seoane et al. 2017). GW plus electromagnetic observations of accreting WD systems will shed new light on the mass transfer and tidal physics at work in these systems (e.g., Breivik et al. 2018). Additionally, some accreting WD binaries are expected to be the progenitors of SNe Ia (e.g., Webbink 1984; Shara & Hurley 2002).

All massive GCs are expected to host populations of accreting WD binaries. Populations of CVs, in particular, are well observed in many GCs (see, e.g., Knigge 2012). As with cluster X-ray binaries, some fraction of CVs in GCs are expected to be formed through dynamical processes, thus opening up alternative channels for CV formation beyond the channels relevant to binary stellar evolution alone. A number of analyses have explored the various ways accreting WD binaries may form dynamically in GCs (e.g., Grindlay et al. 1995; Ivanova et al. 2006; Belloni et al. 2016, 2019).

Table 3 lists the total number of WDs and the total number of (detached and accreting) WD binaries for the four representative cluster models shown in Tables 1 and 2. In Table 9, we list more expansive information on the WD binaries found in every simulation.

Table 3
White Dwarf Properties in Four Representative Clusters

	$M_{\rm tot}$ ($M_\odot$)	Total WDs ($\times 10^4$)	Det. WD Binaries	Acc. WD Binaries	WD–WD Coll.	WD–NS Coll.	WD–BH Coll.
Typical	2.3×10^5	7.7–8.4	400–463	32–35	0	0	0
Core-collapsed	1.9×10^5	7.1–7.5	85–125	10–18	66	17	0
Low-mass	5×10^4	1.8–1.9	321–336	44–51	0	0	0
High-mass	10^6	32–35	858–1029	145–181	2	1	0

Note. Ranges of total numbers of WDs, WD binaries, and WD collisions with other compact remnants across the four characteristic models defined as in Table 1.

As discussed in Section 4, the number of NS binaries formed in a cluster correlates in an intuitive way with various cluster properties, especially the cluster mass and density; the denser the cluster, the more dynamical encounters an NS undergoes, presenting more opportunities to form both detached and accreting NS binaries. Given that the most massive WDs in a cluster ($\approx$1.2–1.4 $M_\odot$) have masses comparable to the typical NS, one may expect similar trends to hold for WD binaries. However, inspection of Tables 1 and 3 reveals the opposite: unlike NS binaries, the WD binary population *decreases* with increasing core density.

This stems from the fact the WD binary (WD–MS, WD–G, WD–WD; both detached and accreting) population derives primarily from the primordial binary population. Thus, for WD binaries, dynamical encounters are in fact more likely to *destroy* binaries destined to become accreting/detached WDs as opposed to forming them. As a consequence, with increasing cluster density (i.e., as a cluster approaches core collapse), the WD binary population is depleted owing to enhanced ionization and dynamical ejections. In this context, Davies (1997) noted that the destruction of CV progenitors may be particularly relevant in the cores of dense clusters. The idea that dynamical interactions may commonly lead to destruction of WD binaries was also explored in, e.g., Knigge (2012). This is in contrast to NS binaries and BH binaries (see Sections 4, 5, and 9), which mostly are formed dynamically, suggesting that the formation processes for NS/BH binaries become more efficient with increasing density.

In this case, the specific numbers of accreting/detached WD binaries with different donor types depend sensitively on assumptions about binary evolution, especially concerning the critical mass ratio for stable mass transfer (see, e.g., Hurley et al. 2002), as well as common envelope physics. A careful study of the role these parameters play is beyond the scope of the current study. However, for recent work on the subject see, e.g., Belloni et al. (2017). For simplicity, we adopt here the default assumptions in BSE and reserve a detailed study of the interplay between the dynamical and binary evolution processes for later work.

6.2. White Dwarf Collisions—Connecting to High-energy Transients

In addition to their application to accreting systems such as CVs and AM CVn, WDs are also associated with a number of high-energy events. In GCs specifically, dynamical collisions of WDs with other stellar populations (particularly other stellar remnants) have been linked to various transients. For example, Shara & Hurley (2002) showed that dynamical interactions amplify the rates of WD–WD mergers and collisions that may lead to SNe Ia. Ivanova et al. (2006) demonstrated similar results regarding the contribution of cluster WDs to the SN Ia rate. WD–NS collisions in GCs have been proposed as a possible mechanism of calcium-rich gap transients observed at high radial offsets in metal-poor galaxies (Kasliwal et al. 2012; Lunnan et al. 2017; De et al. 2018; Shen et al. 2019). Additionally, tidal disruptions of WDs by BHs (especially IMBHs) in GCs have been examined in several analyses (Rosswog et al. 2009; MacLeod et al. 2016; Fragione et al. 2018b). It has been proposed that such WD TDEs serve as viable mechanisms for a number of observed high-energy events (e.g., Krolik & Piran 2011; Jonker et al. 2013). In this section, we examine WD–remnant collisions in our models and discuss the implications of these events for a number of possible transients.

In Columns (6)–(8) of Table 3, we list the total number of WD–WD, WD–NS, and WD–BH collisions occurring during dynamical encounters (e.g., single–single or binary-mediated encounters) in the characteristic cluster models from before. Because we are focusing here on only those WD collisions that occur dynamically (unlike, e.g., the CVs discussed in the previous subsection, which are sensitive to binary evolution processes that complicate potential correlations with various cluster parameters), we can explain the relative rates of these events in the models shown in Table 3 through simple dynamical arguments. As discussed in Section 3 (see especially Figure 4), when large numbers of BHs are present in a cluster, dynamical interactions in less massive stellar populations (e.g., WDs) are less frequent simply because the less massive populations tend to be driven out to larger radial positions owing to BH burning. Only when the BH population decreases sufficiently do less massive populations like WDs become dynamically active. Of the four clusters shown in Table 3, only the core-collapsed model (N8-RV0.5-RG8-Z0.01) has a dynamically insignificant population of BHs (which, in turn, is what allowed this cluster to undergo core collapse in the first place). As expected, it is in this model that we see the most WD collisions. Indeed, the radial profiles of various stellar populations are shown for this particular model in the top panel of Figure 4. We see clearly from that figure that at late times the WDs are actually the dominant stellar population by number in the cluster's innermost regions. Thus, we expect core-collapsed clusters (e.g., M15 and NGC 6752) to be the most likely candidates for WD collisions and the transient electromagnetic signatures associated with these events.

In our full set of 148 simulations, we identify 672 WD–WD collisions (of which 153, 356, and 163 occur through single–single, binary–single, and binary–binary encounters, respectively), 92 WD–NSs (of which 10, 47, and 35 occur through single–single, binary–single, and binary–binary encounters, respectively), and 57 WD–BHs (of which 10, 27, and 20 occur through single–single, binary–single, and binary–binary encounters, respectively). The exact number of single–single versus binary-mediated events depends on the assumed initial binary fraction. Here, the initial binary fraction is fixed to 5%.

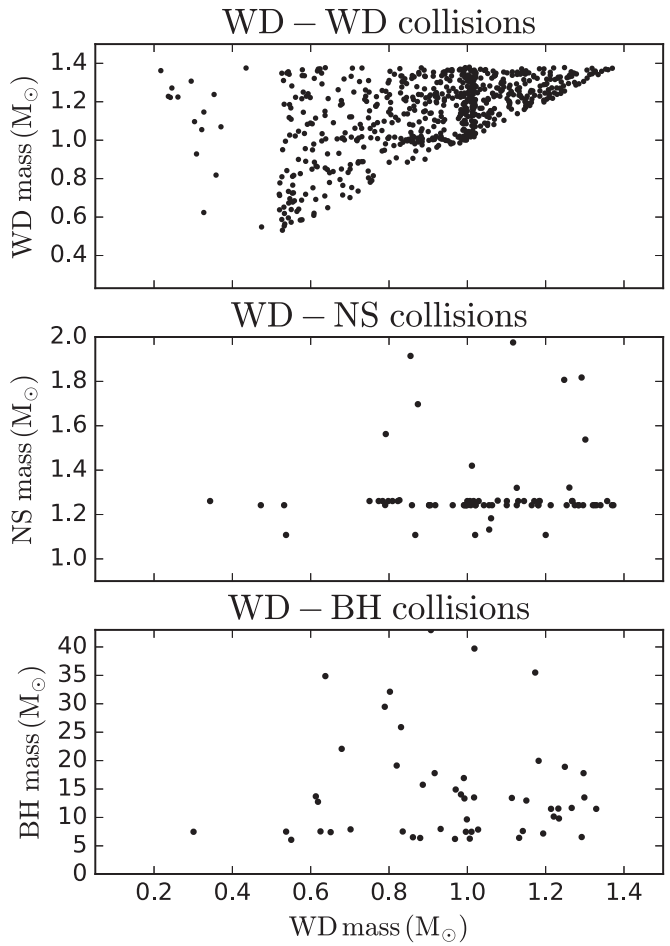

Figure 8. All dynamically mediated WD collisions with various compact remnants identified in our models. Top panel: WD–WD collisions; middle panel: WD–NS collisions; bottom panel: WD–BH collisions. These collisions may be associated with a number of high-energy transients, as discussed in the text.

We reserve for future studies a detailed exploration of the effect of binary fraction on the total number of WD collisions of various channels.

As suggested by Table 3, these dynamically mediated collisions occur most frequently in those models with initial $r_v = 0.5$ pc that undergo core collapse. Indeed, roughly 70% of all WD collisions occur in the 36 simulations with $r_v = 0.5$ pc, while roughly 25% occur in the 36 simulations with $r_v = 1$ and 5% in the remaining simulations with $r_v \geqslant 2$ pc. In Figure 8, we show masses for all collisions of WDs with compact remnant targets.

Furthermore, because dynamically mediated WD collisions occur most frequently only after a cluster has undergone core collapse (which typically takes ∼1 Gyr; see Figure 5), we find that WD collisions occur primarily at late times. This is in contrast to, for example, binary BH mergers, which begin to occur as soon as the BHs mass-segregate and become dynamically active in the BH-dominated core. In Figure 9, we show the cumulative distribution of collision times for all types of WD collisions compared to the distribution of merger times for binary BH mergers (which will be discussed in more detail in Section 9). Here we simply show the distribution of collision times relative to the birth time of the cluster. Cluster birth times are of course not fixed, and a more realistic estimate of the time distribution of WD collisions would need to

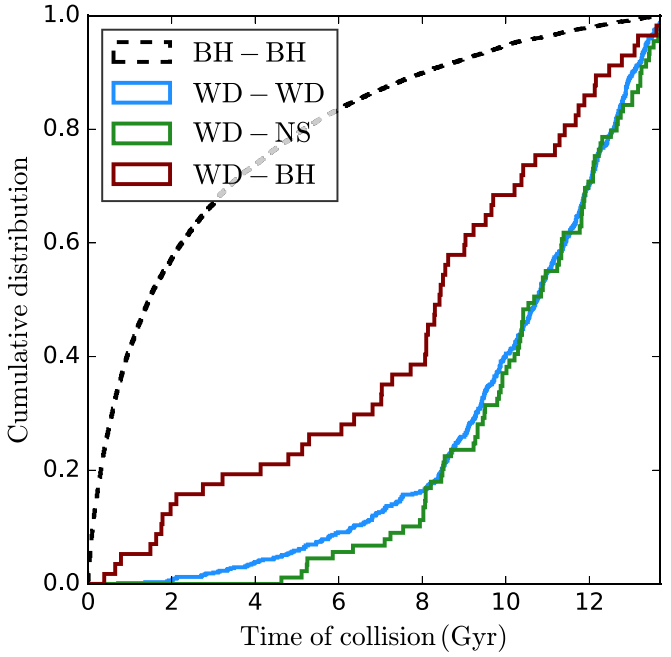

Figure 9. Cumulative distribution of collision times (relative to birth time of cluster) for all WD–WD (blue), WD–NS (green), and WD–BH (red) collisions, compared to the distribution for binary BH mergers (dashed black). We show here distributions for all collisions/mergers occurring in our complete set of models.

incorporate a cluster age distribution. Indeed, the time distributions shown in Figure 9 imply that for old clusters with present-day ages $\lesssim$6 Gyr, WD collisions may have never occurred. We reserve this more detailed analysis for future work and simply emphasize here that, in general, WD collisions preferentially occur in old GCs.

Grouping all models together, we estimate that WD–WD collisions occur at a rate of roughly 10^{-7} yr^{-1} in old ($t \gtrsim 6$ Gyr) GCs in an MW-like galaxy (assuming 150 total clusters), while the rates for WD–NS and WD–BH collisions are roughly 10^{-8} yr^{-1}.

As described in Section 2, we record collisions during close dynamical encounters in the "physical collision" limit: in order for two objects to undergo a collision, they must satisfy the requirement $r_p < R_1 + R_2$. However, more distant close encounters that fall in the tidal disruption or even tidal capture regime may also ultimately lead to a "collision-like" event.[10] The minimum pericenter distance that leads to tidal capture for WD encounters is likely a few times the physical radius (e.g., Samsing et al. 2018). Hence, the collision rates reported in the above paragraph may underestimate the true number of dynamically mediated collisions by a factor of a few to perhaps an order of magnitude, relative to the ideal where tidal disruptions/captures are included. Even so, these rates are several orders of magnitude lower than the observed rates of SNe Ia and Ca-rich transients, which are both estimated to

[10] Recent work (e.g., Rodriguez et al. 2018a; Samsing & D'Orazio 2018) has also shown that GW emission during close fly-bys during fewbody encounters plays an important role in the formation of BH binaries and mergers in GCs. It is essential to include post-Newtonian corrections in these resonant encounters to capture this merger channel. However, post-Newtonian effects do not have an analogous effect for WDs, because the characteristic distance for post-Newtonian effects to become a dynamically significant source of energy dissipation for WDs lies within the WD's tidal disruption radius.

occur at rates of roughly a few $\times 10^{-3}$ yr^{-1} for MW-like galaxies (e.g., Frohmaier et al. 2018).

In addition to WD collisions arising through dynamical interactions, WDs may also be driven to merger with other compact remnants through binary evolution processes, in particular gravitational inspiral (e.g., Kremer et al. 2015; Shen 2015). These inspiral WD binaries may form either through dynamical exchange encounters or through binary evolution processes (where, e.g., a common envelope event brings the WD components close enough to inspiral within a Hubble time). Like the collision events discussed to this point, these WD mergers may similarly contribute to the total rate of high-energy transients (e.g., Shara & Hurley 2002; Shen et al. 2019). These WD merger events may occur inside the host cluster or outside of the cluster if the WD binary is ejected through dynamical recoil associated with dynamical formation or through natal kicks associated with the formation of an NS/BH companion. Indeed, these various formation channels for WD merger events (collisions during dynamical encounters, in-cluster mergers, and ejected mergers) are analogous to the merger channels that have been discussed at length in various recent papers in the context of binary BH mergers (e.g., D'Orazio & Samsing 2018; Rodriguez et al. 2018a; Samsing & D'Orazio 2018; Kremer et al. 2019c; Zevin et al. 2019), which we discuss in detail in Section 9. However, unlike binary BH mergers in GCs, which are essentially driven entirely by dynamical processes (primordial BH mergers constitute $\lesssim$5% of all mergers; Rodriguez et al. 2018b) and are thus largely insensitive to the initial binary properties assumed, the evolution of WD binaries is influenced less significantly by dynamical interactions, as discussed in Section 6.1. This indicates that the exact numbers of these events depend sensitively on both the assumed primordial binary fraction and the binary evolution physics that governs the formation of compact WD binaries, especially common envelope physics (e.g., Shara & Hurley 2002). We reserve a detailed exploration of the effect these various processes have on WD mergers for a more focused study.

7. Stellar Collisions

As hinted at in the previous section in the context of WDs, stellar collisions can occur at significant rates in dense systems like GCs. In addition to the WD collisions discussed in the previous section, which may lead to SNe Ia or Ca-rich transients, stellar collisions involving BHs and NSs may lead to a variety of distinct transients with implications for a number of astrophysical phenomena. For example, collisions of BHs/NSs with MS stars may lead to luminous flares and possibly ultralong gamma-ray bursts (e.g., Perets et al. 2016; Fragione et al. 2019b; Kremer et al. 2019b), and collisions of BHs/NSs with giants may lead to ultracompact X-ray binaries with WD donors (e.g., Ivanova et al. 2005, 2010; Kremer et al. 2019b).

Although collisions between compact objects and luminous stars may be most exciting for the study of high-energy transients, these types of collisions tend to be rare simply because compact objects, particularly BHs and NSs, constitute only a small fraction of the total population in a typical cluster (see Figure 4 and Table 6). More common are collisions where both objects are luminous stars (i.e., MS–MS collisions or MS–giant collisions), events that have been well studied theoretically (Hills & Day 1976; Bacon et al. 1996; Lombardi et al. 2002; Fregeau & Rasio 2007; Leigh et al. 2011; Antognini & Thompson 2016). In particular, collisions between luminous stars may have important implications for the formation of BSs (to be discussed in detail in Section 8). In some cases, the post-collision evolution of these events may be observed as optical transients (e.g., Tylenda et al. 2011; MacLeod et al. 2017; Metzger & Pejcha 2017). In Table 8 in the Appendix, we list the total number of various stellar collision types (i.e., MS–MS, MS–giant, MS–BH, etc.) occurring in each simulation of this study.

In Figure 10, we show masses of all collisions between luminous stars occurring in our simulations. In panels (a) and (b) we show those collisions that occur early in the host cluster's evolution ($t < 30$ Myr), while in panels (c) and (d) we show late-time collisions ($t > 8$ Gyr). The left panels show MS–MS collisions, and the right panels show MS–giant collisions.

At early times, when massive stars are still present in the cluster, 100 $M_\odot$–0.1 $M_\odot$ MS–MS collisions and 30 $M_\odot$–0.1 $M_\odot$ giant–MS collisions are most typical. These typical values are determined by a combination of the stellar IMF and gravitational focusing. Stars of some specific mass M_1 and radius R_1 will undergo collisions with "target" stars of mass M_2 and radius R_2 at a rate given by

$$\Gamma_{\rm coll} = n_2 \pi r_p^2 v_\infty \left(1 + \frac{2G(M_1+M_2)}{r_p v_\infty^2}\right) N_1, \quad (4)$$

where n_2 is the number density of the targets, $r_p = R_1 + R_2$ is the minimum pericenter distance that leads to a collision, v_∞ is the relative velocity of the pair of objects at infinity, and N_1 is the total number of stars having the selected mass of interest, M_1.

As described in Section 2, we adopt the IMF of Kroupa (2001), which peaks at roughly 0.1 $M_\odot$, a typical M dwarf. For this IMF, M dwarfs dominate over 100 $M_\odot$ stars by a factor of roughly 1000. By using Equation (4) and adopting parameters typical of young massive clusters, we can estimate the relative rates of various collision types to make sense of the trends exhibited in Figure 10.

We assume a typical cluster core radius of 1 pc, a typical $v_\infty = 10$ km s^{-1}, and that 0.1 and 100 $M_\odot$ stars have radii of roughly 0.1 and 30 $R_\odot$, respectively. We also assume that, for a typical cluster containing 8×10^5 stars at birth, roughly 10^5 stars are M dwarfs ($M \sim 0.1\ M_\odot$), while roughly 100 are high-mass stars with $M \sim 100\ M_\odot$. In this case, from Equation (4), the rates of 0.1 $M_\odot$–0.1 $M_\odot$, 0.1 $M_\odot$–100 $M_\odot$, and 100 $M_\odot$–100 $M_\odot$ collisions in young massive clusters are roughly 0.02, 2, and 0.007 Myr^{-1}, respectively. Thus, as shown in the top panels of Figure 10, 0.1 $M_\odot$–100 $M_\odot$ collisions are most common. Although the collision cross section for 100 $M_\odot$–100 $M_\odot$ is higher, these events are limited by the relatively low number of objects. Also, though the number of possible targets is largest for 0.1 $M_\odot$–0.1 $M_\odot$ collisions, the rate here is limited by the relatively small cross section and the decreased effect of the gravitational focusing term.

In our simulations, we assume no primordial mass segregation. Thus, at $t = 0$, all stars of all masses are equally mixed within the cluster radially. However, a number of recent studies (e.g., Baumgardt et al. 2008; Šubr et al. 2008; Habibi et al. 2013; Pang et al. 2013; Pavlík et al. 2019) suggest that primordial mass segregation may be a more appropriate initial

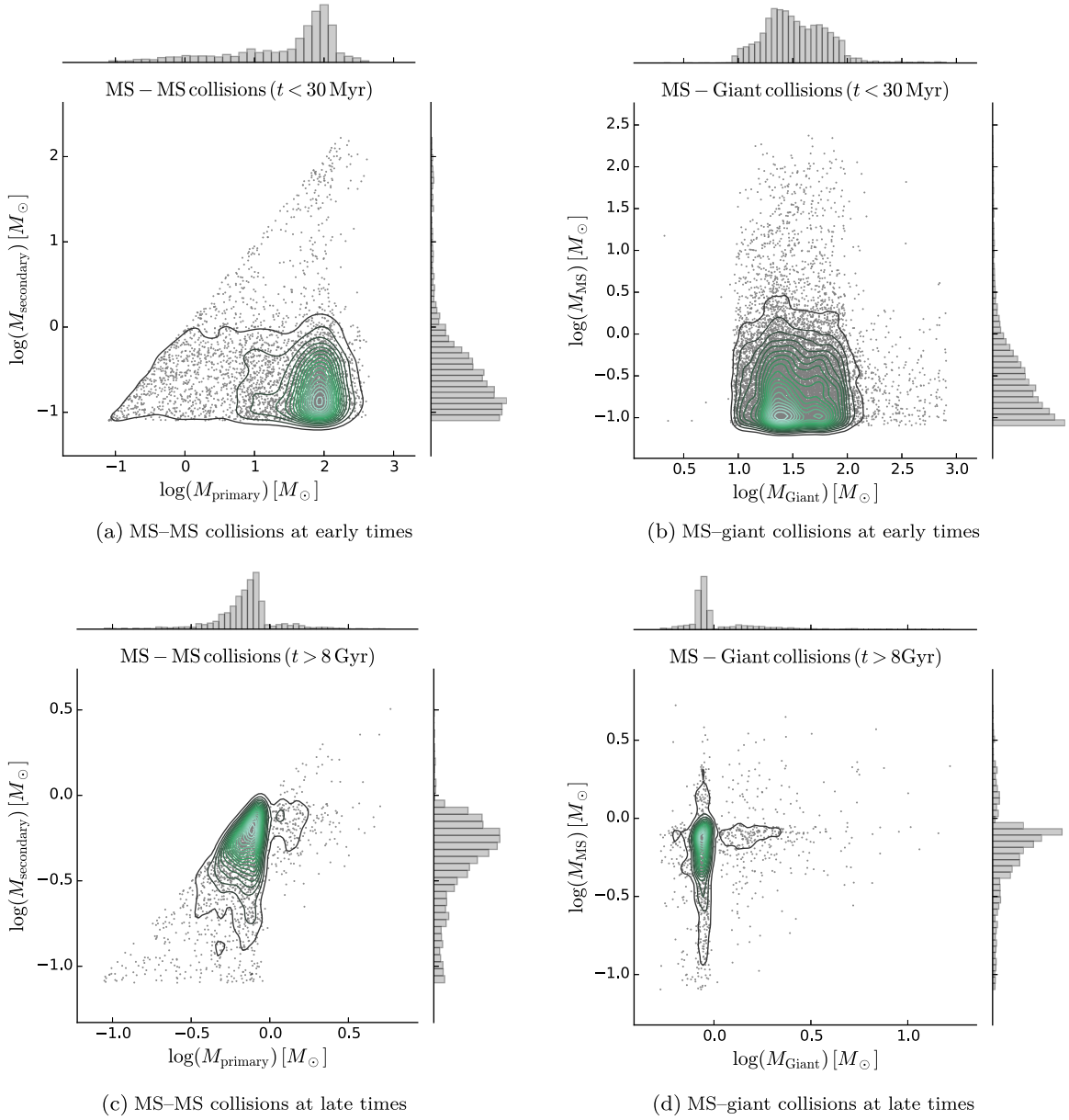

(a) MS–MS collisions at early times

(b) MS–giant collisions at early times

(c) MS–MS collisions at late times

(d) MS–giant collisions at late times

Figure 10. All luminous star collisions occurring in our simulations separated by collision component types and by time. Here, "early times" refers to $t < 30$ Myr after cluster formation, while "late times" refers to $t > 8$ Gyr.

condition. In this case, because the most massive stars would be preferentially found closer to the cluster's center, where densities are higher, collisions where both components are massive stars may dominate the overall rate. To this point, as shown in the bottom two panels of Figure 10, at late times ($t > 8$ Gyr), when the clusters have evolved sufficiently toward a mass-segregated configuration, collisions of equal-mass components become most common. In this case, the most massive stars (for $t \sim 10$ Gyr, the MS turnoff mass is roughly 0.8 $M_\odot$) are preferentially found in the dense core of the cluster and are therefore more likely to undergo collisions through dynamical encounters.

We note that a detailed, incompleteness-corrected comparison of mass segregation (Δ) in all our models to Δ observed in 50 MW GCs shows that our simulations accurately reproduce the Δ distribution in GCs (see Figure 3 of Weatherford et al. 2019), suggesting that primordial mass segregation may be unnecessary. We reserve a more detailed examination of the effects of primordial mass segregation for a later study.

As discussed in, e.g., Spera et al. (2019) and Banerjee et al. (2019), massive stellar mergers occurring through binary evolution may have important consequences for the formation of massive BHs, specifically BHs lying within the so-called upper mass gap expected from (pulsational) pair-instability SNe (e.g., Belczynski et al. 2016a; Woosley 2016; Spera & Mapelli 2017). In principle, dynamically mediated stellar collisions of massive stars in GCs may have similar implications for BH formation. Indeed, if appropriate conditions are met (i.e., if a cluster is sufficiently dense at early times), stellar collisions may lead to a runaway scenario, resulting in the formation of a very massive star and, ultimately, an IMBH (e.g., Portegies Zwart et al. 2004; Freitag et al. 2006; Giersz et al. 2015; Mapelli 2016). For now, we simply note that, as motivated by the collision rates demonstrated in Table 8 and

Figure 10, collisions may indeed play a role in massive-star evolution, with specific applications to BH formation. We will more fully explore the implications of stellar collisions for BH formation in an upcoming paper.

Finally, as shown in Equation (4), the overall collision rate depends on the number density of objects, which is specified in our simulations at early times by the initial r_v. Thus, we expect that clusters with smaller r_v (that are more likely to undergo core collapse by the present day, as discussed in Section 3.4) will feature more stellar collisions than models with higher initial r_v. To quantify, in the $r_v = 0.5$ pc simulation, N8-RV0.5-RG8-Z0.01, which has undergone core collapse by $t = 12$ Gyr (see Figure 5), we identify 811 MS–MS and 3044 MS–giant collisions at early times and 886 MS–MS and 121 MS–giant collisions at late times. In contrast, in the $r_v = 2$ pc model, N8-RV2-RG8-Z0.01—which still retains a large population of BHs at late times and does not undergo core collapse—we identify only 3 MS–MS and 45 MS–giant collisions at early times, but 48 MS–MS and 16 MS–giant collisions at late times. Hence, if stellar collisions in young clusters indeed play a role in BH formation, we expect this effect to be most pronounced in the clusters that are most dense initially and ultimately undergo core collapse. Similarly, because these clusters also exhibit higher stellar collision rates at late times, we expect clusters with smaller r_v to feature an increased number of BS stars. We discuss the specific application to BSs in the following section.

8. Blue Stragglers

BSs are hydrogen-burning stars that are photometrically bluer and brighter than the MS turnoff for stars of similar ages (Sandage 1953). A star may become a BS when it undergoes one of several possible stellar interactions that lead to an increase in the star's mass. Such interactions could include accretion of material from a binary companion during Roche lobe overflow or a physical collision with another star, as described in Section 7. The latter channel is expected to become important in dense stellar systems like open clusters and GCs, where stellar collisions are common. BSs are well observed in nearly all GCs in the MW (e.g., Piotto et al. 2002; Ferraro et al. 2012) and also in many open clusters (e.g., Mathieu & Geller 2009). A number of analyses have explored the formation channels for BSs in clusters (e.g., Ferraro et al. 2012; Chatterjee et al. 2013; Hypki & Giersz 2017). Chatterjee et al. (2013) noted that in dense GCs (central densities $\gtrsim 10^3$ pc^{-3}), stellar collisions appear to be the dominant formation channel for BSs, while for lower-density open clusters, binary mass transfer appears to dominate. This is consistent with recent observational work (e.g., Geller & Mathieu 2011; Gosnell et al. 2019) that showed that mass transfer indeed appears to be the dominant formation mechanism in open clusters. Ferraro et al. (2012) noted that BSs can be used as probes of cluster dynamical evolution. Specifically, Ferraro et al. (2012) pointed out that GCs can be grouped into distinct dynamical age families based on their BS radial distributions. Thus, BSs can be used as important observational constraints of cluster properties.

We use the following procedure to count the total number of BSs in our models: First, the MS turnoff is defined as the luminosity, $L_{\rm TO}$, corresponding to the point on the MS branch with the highest median temperature, $T_{\rm TO}$. BSs are then defined as any single or (unresolved) binary containing an MS star where the total luminosity and temperature (luminosity-weighted mean temperature for binaries) exceed $L_{\rm BS} = 2L_{\rm TO}$ and $T_{\rm TO}$, respectively. Figure 11 shows a zoomed-in portion of the H-R diagram of simulation N8-RV0.5-RG8-Z0.01 at 12 Gyr, shown earlier in the top left panel of Figure 6. In this figure, the BS selection criterion is visually represented by the blue shaded region, within which any single or binary containing an MS star is counted as a BS. Column (11) of Table 9 lists the mean number of BSs in each simulation at late times, while Table 4 lists the total number of BSs in the four characteristic models from previous sections.

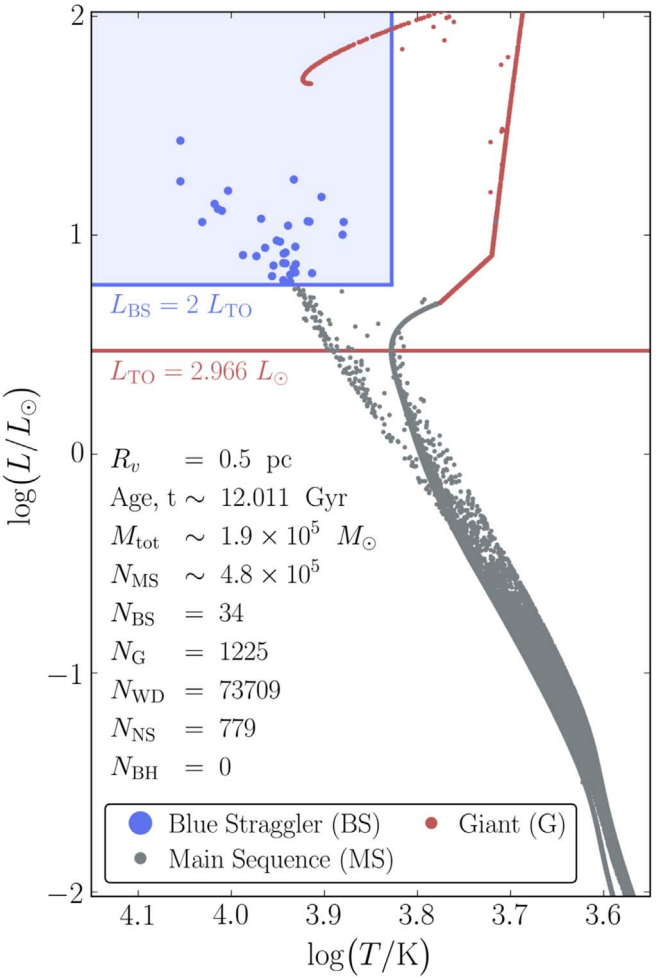

Figure 11. H-R diagram of the core-collapsed model N8-RV0.5-RG8-Z0.01 at $t = 12$ Gyr illustrating the BS selection algorithm. Each dot represents a single or binary star (all binaries are considered unresolved), with BSs colored in blue, giants in red, and the MS in gray. Note that for binaries the summed luminosity and luminosity-weighted mean temperature are plotted. To select BSs, the turnoff is first defined as the luminosity, $L_{\rm TO}$, corresponding to the point on the MS with the highest median temperature, $T_{\rm TO}$. $L_{\rm TO}$ is indicated by the red horizontal line. BSs are then defined as any single or binary containing an MS star where the luminosity and temperature (defined above for binaries) exceed $L_{\rm BS} = 2L_{\rm TO}$ and $T_{\rm TO}$, respectively (see the blue shaded region).

Figure 12 shows the total number of BSs versus the total number of BHs for all snapshots with ages in the range of 10–13 Gyr from $Z = 0.1\ Z_\odot$ models (chosen simply to reflect the median metallicity of MW GCs; see Figure 2). Here, we show only low-metallicity models simply because these are most representative of the old GCs observed in the MW. From top to bottom, the different panels correspond to models with $N = 1.6 \times 10^6$, 8×10^5, 4×10^5, and 2×10^5, respectively.

Table 4
Blue Stragglers in Four Representative GCs

	$M_{\rm tot}(M_\odot)$	Blue Stragglers
Typical	2.3×10^5	0–2
Core-collapsed	1.9×10^5	28–91
Low-mass	5×10^4	0–2
High-mass	10^6	2–16

Note. Ranges in total number of BSs for all snapshots in the age range 10–13 Gyr for the four characteristic clusters defined as in Table 1.

A clear anticorrelation exists between the number of BSs and the number of retained BHs. Furthermore, models with smaller initial r_v have, on average, more BSs than models with larger initial r_v.

Previous analyses (e.g., Ferraro et al. 2012; Alessandrini et al. 2016; Ferraro et al. 2019) have noted that BS populations can be used to trace clusters' dynamical ages. Here, we demonstrate this same result with an important addendum: the link between BSs and dynamical age is intertwined with the clusters' evolving BH populations. As discussed in Section 3, the most dynamically evolved clusters retain the fewest BHs and are most likely to be found in more centrally concentrated or even core-collapsed configurations. Through mechanisms identical to those relevant for MSP formation (Section 5) and WD collisions (Section 6.2), these dynamically evolved clusters where BH burning is dynamically insignificant facilitate an increased rate of dynamical interactions of MS stars and thus produce more BSs.

9. Binary Black Hole Mergers

As the catalog of GW detections of merging binary BHs (BBHs) continues to grow (The LIGO Scientific Collaboration et al. 2019a), there is mounting evidence suggesting that dynamical interactions in GCs play a prominent role in the formation of merging BBHs in the local universe. In particular, key features of the LIGO/Virgo detections made to date—including the masses, spins, and detection rates—point toward dynamical origins for at least some BBH mergers. The existence of a significant cluster dynamics merger channel is further motivated by observational and theoretical evidence showing that GCs similar to those observed in the MW likely host large populations of BHs at present, as discussed in Section 3. Of course, the story is far from complete, and many other BBH merger channels have been proposed, including isolated evolution of high-mass stellar binaries (e.g., Dominik et al. 2012, 2013; Belczynski et al. 2016a, 2016b), GW capture of primordial BHs (e.g., Bird et al. 2016; Sasaki et al. 2016), secular interactions in hierarchical triple systems (e.g., Antonini & Rasio 2016; Antonini et al. 2017; Silsbee & Tremaine 2017; Hoang et al. 2018; Leigh et al. 2018; Rodriguez & Antonini 2018; Fragione & Kocsis 2019; Fragione et al. 2019a), and dynamical interactions within the disks of active galactic nuclei (e.g., Bartos et al. 2017; Yang et al. 2019).

In this section, we discuss the formation of merging BBHs in this new set of cluster simulations. We specifically explore how the rates and properties of BBH mergers vary with cluster r_v. In Section 9.1, we discuss specific subchannels for merging BBHs in GCs, including (for the first time in CMC simulations) the contribution of single–single capture mergers. In Section 9.2, we examine how the BBH merger rate scales with cluster mass.

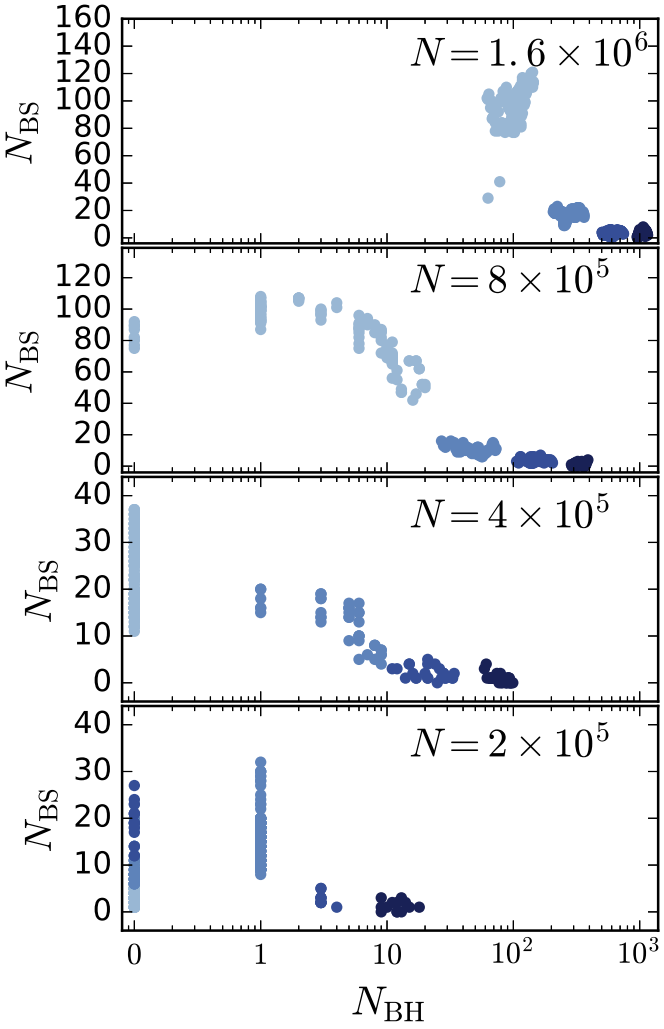

Figure 12. Number of BSs ($N_{\rm BS}$) vs. total number of retained BHs ($N_{\rm BH}$) for snapshots in the age range 10–13 Gyr. Shown here are models with 0.1 $Z_\odot$, the most typical metallicity value for old GCs in the MW (see Figure 2). From top to bottom, we show models of decreasing total particle number. Different shades of blue denote different initial r_v, as in previous figures.

In Section 9.3, we calculate the cosmological rates of BBH mergers, while we explore in Section 9.4 how BBH properties vary with the simulation parameters considered in this study.

9.1. Dynamical Merger Channels

As explored in a number of recent analyses, BBH mergers are expected to occur through four distinct dynamical channels in dense star clusters (D'Orazio & Samsing 2018; Rodriguez et al. 2018a; Samsing & D'Orazio 2018; Kremer et al. 2019c; Zevin et al. 2019). Each of these channels is expected to produce BBHs with distinct GW frequency and eccentricity distributions. We summarize each of these channels and their main features below.

Ejected mergers: As BBHs undergo hardening encounters in the core of a cluster, they receive dynamical recoil kicks of magnitudes that scale with the binary orbital velocity (e.g., Rodriguez et al. 2016). Thus, as BBHs are hardened to increasingly compact orbital separations, they recoil at higher velocities, until, eventually, the dynamically attained recoil velocity exceeds the escape velocity of the cluster and the BBH is ejected. Depending on the orbital parameters at the time of

ejection, such a BBH may inspiral and merge owing to GW emission within the age of the universe. Such a binary is labeled an "ejected merger." In a typical cluster, these mergers constitute roughly 50% of all BBH mergers.

In-cluster two-body mergers: Binaries still retained in their host clusters that merge *between* resonant dynamical encounters (henceforth referred to as the "two-body merger" channel). In a typical cluster, two-body mergers constitute roughly 35% of all BBH mergers.

In-cluster fewbody mergers: Binaries that merge through gravitational capture *during* resonant encounters (henceforth referred to as the "fewbody capture" channel). In a typical cluster, fewbody capture mergers constitute roughly 10% of all BBH mergers, with roughly 5% occurring through binary–single and binary–binary encounters, respectively.

In-cluster single–single captures: Most recently, Samsing et al. (2019) pointed out that BBHs also form through GW capture in single–single BH encounters in clusters. In a typical cluster, "single–single capture mergers" constitute roughly 5% of all BBH mergers.

All of the above dynamical channels produce BBHs with unique and potentially distinguishable properties that should, in principle, be detectable as GW sources by LIGO/Virgo, as well as lower-frequency third-generation GW detectors such as LISA (Amaro-Seoane et al. 2017), DECIGO (Kawamura et al. 2011; Isoyama et al. 2018), and Tian Qin (Luo et al. 2016). We list the total number of BBH mergers catalyzed by each of these channels in Table 10 in the Appendix.

9.2. Average Number of Mergers per Cluster

The models considered in this study have present-day cluster masses of up to roughly $10^6\,M_\odot$. Although this is appropriate for modeling only those clusters observed in the MW (see Figure 2), the cluster mass function for the full population of clusters in the local universe is expected to extend up to larger masses (e.g., Harris et al. 2014; El-Badry et al. 2019). In order to estimate a realistic cosmological rate of BBH mergers in GCs, we must take into account the full cluster mass function. We do so by adopting a method similar to that of Rodriguez et al. (2015) and Rodriguez et al. (2016), as summarized below.

As described in Rodriguez et al. (2015), the number of mergers per cluster scales roughly linearly with the total cluster mass. We show this relation for all cluster models in Figure 13, separating clusters by initial r_v, as in previous figures. For all models of a given r_v, we fit the $N_{\rm merger}$–$M_{\rm tot}$ relation shown in Figure 13 using a linear regression, as in Rodriguez et al. (2015). The best-fit curves for the $N_{\rm merger}$–$M_{\rm tot}$ relation shown in Figure 13 are given for each value of r_v by

$$N_{\rm merger} = 82 \times \left(\frac{M_{\rm tot}}{10^5\,M_\odot}\right);\ r_v = 0.5\ {\rm pc},$$
$$= 57 \times \left(\frac{M_{\rm tot}}{10^5\,M_\odot}\right);\ r_{\rm v} = 1\ {\rm pc},$$
$$= 36 \times \left(\frac{M_{\rm tot}}{10^5\,M_\odot}\right);\ r_{\rm v} = 2\ {\rm pc},$$
$$= 16 \times \left(\frac{M_{\rm tot}}{10^5\,M_\odot}\right);\ r_{\rm v} = 4\ {\rm pc}.$$

In order to compute the average number of BBH mergers per cluster of a given r_v, we then integrate each of the linear relations over a normalized cluster mass function from 0 to $2 \times 10^7\,M_\odot$. As in Rodriguez et al. (2015), we assume a lognormal distribution for the cluster mass function with mean $\log M_0 = 5.54$ and width $\sigma_M = 0.52$, based on the GC luminosity functions described in Harris et al. (2014) and assuming a mass-to-light ratio of 2 (Bell et al. 2003). In Table 5, we list the average number of BBH mergers per cluster for each r_v. In Columns (2)–(5), we distinguish between BBH mergers occurring through the various channels described in Section 9.1. As shown, the number of mergers occurring through each formation channel (and the total number of mergers) varies inversely with initial r_v. Clusters with smaller r_v are denser (see Section 3) and therefore feature a higher rate of interactions that form BBHs. This is consistent with the results shown in a number of previous analyses (e.g., Rodriguez et al. 2016; Choksi et al. 2018; Zevin et al. 2019). It is clear from Section 3 that an initial r_v of 0.5 pc is appropriate for a fraction of observed clusters in the MW (specifically, those that are most centrally concentrated at present). Thus, in order to estimate a realistic BBH merger rate from clusters, models with $r_v = 0.5$ pc must be incorporated.

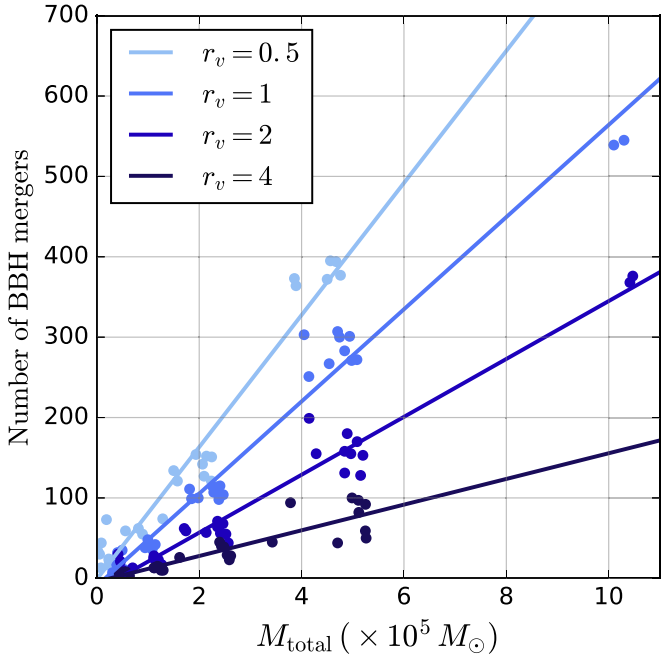

Figure 13. Total number of BBH mergers vs. final cluster mass for all simulations separated by r_v (various shades of blue as in previous figures). Solid lines show the linear fit to the data for each r_v as described in the text, and as given by Equation (5).

Table 5
Average Number of BBH Mergers per Cluster for Various Initial Virial Radii Computed by Integrating over the Cluster Mass Function as Described in Section 9.2

r_v	In-cluster			Ejected	Total
	s–s	Fewbody	Two-body		
0.5	26	85	336	299	746
1	25	55	233	196	510
2	9	35	123	140	308
4	4	17	49	70	140

9.3. Merger Rates

In order to calculate the cosmological rate of BBH mergers, we adopt a method similar to Rodriguez et al. (2015). The cumulative merger rate is given by

$$R(z) = \int_0^z \mathcal{R}(z') \frac{dV_c}{dz'} (1+z')^{-1} dz', \quad (5)$$

where dV_c/dz is the comoving volume at redshift z and $\mathcal{R}(z)$ is the comoving (source) merger rate. The comoving rate is given by

$$\mathcal{R}(z) = f \times \rho_{\rm GC} \times \frac{dN(z)}{dt}. \quad (6)$$

Here $\rho_{\rm GC}$ is the volumetric number density of clusters, assuming a constant value of $\rho_{\rm GC} = 2.31\,{\rm Mpc}^{-3}$ (consistent with Rodriguez et al. 2015; Rodriguez & Loeb 2018), f is a scaling factor intended to incorporate the contribution of the cluster mass function's high-end tail not covered by our models (see Section 9.2), and $dN(z)/dt$ is the number of mergers per unit time at a given redshift.

We compute $dN(z)/dt$ using the following procedure: first, we generate a complete list of merger times ($t_{\rm merger}$) for all BBHs that merge within a Hubble time in our model set (roughly 10^4 total mergers). For each of these mergers, we draw 10 random ages ($t_{\rm age}$) for the host cluster from which the merger originated. We then compute the effective merger time for each BBH merger as $t_{\rm effective} = t_{\rm Hubble} - t_{\rm age} + t_{\rm merger}$. As in Rodriguez et al. (2018b), we draw cluster ages from the metallicity-dependent age distributions of El-Badry et al. (2019). We then compute the number of mergers per time, $dN(z)/dt$, by dividing this list of effective merger times into separate redshift bins. Note that we also scaled down these rates to correct for oversampling—caused by drawing 10 cluster ages for each merger and by drawing mergers from a large set of cluster models. To correct for the former oversampling, we simply divide the rates by a factor of 10. To correct the latter, we divide by the total number of models sampled (weighting all models equally for simplicity).

We include the scaling factor f in Equation (6) to account for the contribution of the cluster mass function's high-mass tail not covered by our models. This factor is calculated as the ratio of the average number of mergers per cluster (computed by integrating over the cluster mass function; see Section 9.2 and Table 5) to the average number of mergers per cluster counted from the models sampled. We compute f separately for each r_v, as in Table 5. In practice, $f \approx 4$ is typical across all r_v values, so that high-mass clusters ($M \gtrsim 5 \times 10^5\,M_\odot$) contribute roughly four times more mergers than low-mass clusters ($M \lesssim 5 \times 10^5\,M_\odot$).

In Figure 14, we show the cumulative rate ($R(z)$) and comoving rate ($\mathcal{R}(z)$) as functions of redshift for the four r_v values considered in this study (blue curves). The combined rate (dashed black curves) is calculated assuming equal contribution from all four values of r_v.[11]

For the reasons discussed in Section 9.2, we also see that the merger rate increases significantly as r_v decreases. Thus, as shown in Figure 14, if initial virial radii of $r_v = 0.5$ pc or smaller are typical for clusters in the universe, the BBH merger rate from clusters may be roughly twice as high as previous estimates (e.g., Rodriguez & Loeb 2018).

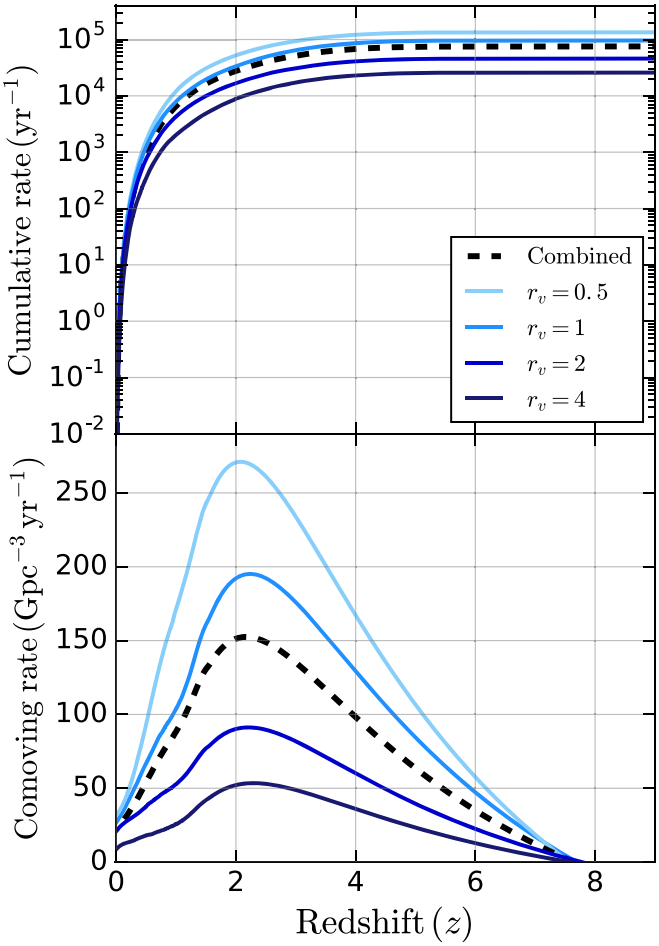

Figure 14. Cumulative and comoving BBH merger rates for clusters, colored by initial virial radius (blue curves). The dashed black curve shows the total combined merger rate.

Overall, the rates shown in Figure 14 for models with $r_v = 1$ or 2 pc are roughly consistent with those of Rodriguez & Loeb (2018), which also used CMC models, but implemented a slightly different rate calculation accounting for metallicity's effect on the cluster mass function. The latest results from the LIGO/Virgo Collaboration suggest a local universe BBH merger rate of $53.2^{+58.5}_{-28.8}\,{\rm Gpc}^{-3}\,{\rm yr}^{-1}$ (The LIGO Scientific Collaboration et al. 2019a, 2019b). Here, we estimate local universe rates ($z = 0$) ranging from roughly 9 to 30 $\rm Gpc^{-3}\,yr^{-1}$, depending on r_v, and a combined rate of roughly 22 $\rm Gpc^{-3}\,yr^{-1}$.

It is worth noting that some uncertainties are left unexplored here, potentially affecting the estimated rates. For instance, we have focused on only the contribution from clusters that have survived to the present day. However, as noted by, e.g., Gnedin et al. (2014) and Fragione et al. (2018a), there likely existed a significant population of clusters that did not survive to the present. The remnants of these disrupted clusters may contribute significantly to the BBH merger rate (e.g., Fragione & Kocsis 2018; Rodriguez & Loeb 2018). Furthermore, in this study we have considered only GCs; however, previous analyses (e.g., Ziosi et al. 2014; Banerjee 2018; Di Carlo et al. 2019) have shown that lower-mass open clusters may also contribute to the BBH merger rate. In this sense, the rates based on this study's

[11] This is likely an oversimplification, but a detailed study of the r_v distribution corresponding to present-day GCs is beyond the scope of this study. See Choksi et al. (2018) for further discussion on this point. We hope to perform a more detailed study on cluster models incorporating more realistic r_v-weighting in a later paper.

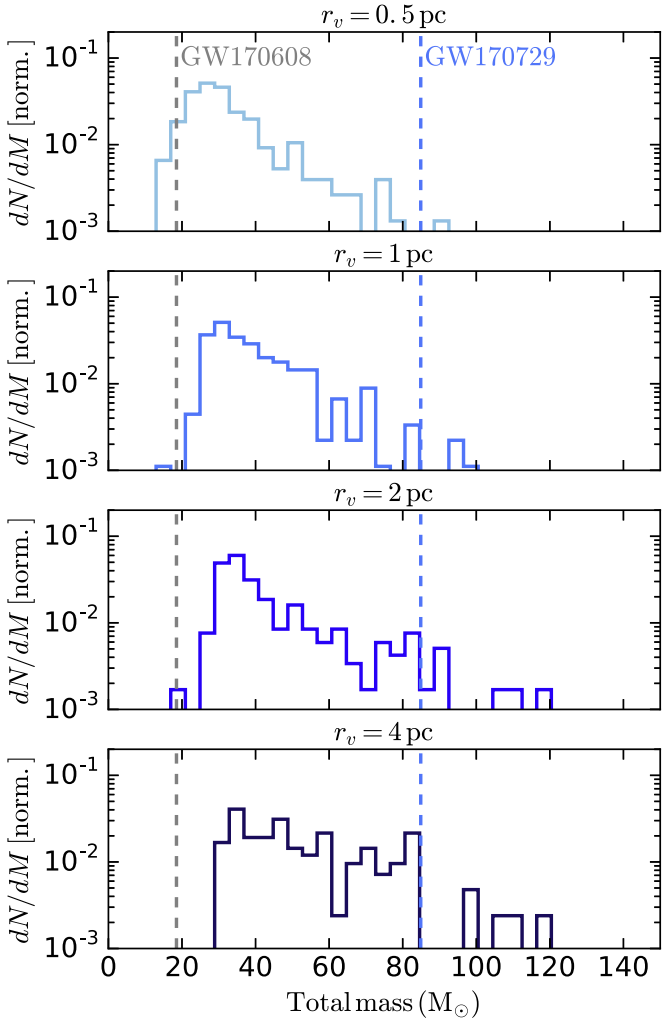

Figure 15. Total mass of all BBH mergers occurring at $z < 0.5$ ($t_{\rm mergers} \gtrsim 6$ Gyr), assuming cluster ages of 12 Gyr. We exclude all solar-metallicity models from the plot and show only low-metallicity models that are more generally representative of old GCs. From top to bottom, we show models with increasing initial r_v. The vertical dashed lines show the total masses of the lowest- and highest-mass BBH mergers detected to date by LIGO/Virgo: GW170608 (gray) and GW170729 (blue).

particular model set can be viewed as lower limits on the total contribution from clusters.

9.4. Effect of r_v on BBH Masses

As a final point, we discuss the different expected properties of BBHs that originate from clusters of varying r_v. In Figure 15, we show the total mass of all BBH mergers in low-metallicity cluster models occurring at redshift <0.5 (representative of local universe mergers, which are most relevant to potential detections by LIGO/Virgo). From top to bottom, we show the distributions for models with $r_v = 0.5$–4 pc. The BBH mass distribution shifts toward smaller masses as r_v decreases. As shown in Figure 3, the depletion rate of BHs directly relates to r_v, such that clusters with smaller r_v retain fewer BHs at late times. As discussed in, e.g., Morscher et al. (2015), the most massive BHs in a cluster are generally among the first to be ejected from the cluster and among the first to merge. The most massive BHs sink farthest into the cluster's core, undergoing more frequent dynamical encounters that lead to both ejection and mergers. The lower-mass BHs ($M \lesssim 15\,M_\odot$) become dynamically active only after the most massive BHs have been ejected. In clusters with smaller initial r_v, high-mass BHs are dynamically processed and ejected relatively quickly. Therefore, in these clusters, high-mass BHs ($M \gtrsim 30\,M_\odot$) tend to merge relatively early (at high redshift).

By late times (low redshift), most of the high-mass BHs in low-r_v models have already been ejected or have merged with other BHs, leaving only the least massive BHs in any significant quantity. As a consequence, the mass distribution of BBH mergers shifts to lower masses in clusters with lower r_v. For clusters with high r_v, the initial relaxation time is longer, so many high-mass BHs still remain at late times. Hence, BBH mergers tend to have higher component masses in these models.

In Figure 15, we show the total masses (dashed vertical lines) for the least and most massive BBH mergers observed to date by LIGO/Virgo (The LIGO Scientific Collaboration et al. 2019a). By considering cluster models with varied r_v, we are able to span the full distribution of observed merger masses. Also note that high-metallicity clusters—which preferentially form lower-mass BH populations owing to the differences in wind mass loss at high metallicities—provide an alternative way to dynamically form low-mass BBH mergers similar to GW170608. Indeed, Chatterjee et al. (2017a) noted that young high-metallicity clusters may be the *only* way such BBHs can be formed dynamically in GCs. Here, we amend this earlier work and show that low-mass BBHs can also form in low-metallicity clusters, provided that the clusters have sufficiently short initial relaxation times.

10. Conclusions and Discussion

10.1. Summary

In this paper, we have introduced a set of 148 cluster simulations (computed using the Monte Carlo code CMC) that span wide ranges in initial cluster mass, size, metallicity, and Galactocentric distance. We showed that these models collectively cover nearly the complete range of parameters of the GCs observed in the MW. Specifically, by varying the clusters' initial virial radii (and therefore their initial relaxation time), we showed that our simulations reproduce both clusters that have undergone core collapse by the present day and those that have not. The onset (or delay) of core collapse is related to the evolution of a cluster's stellar-mass BH population. When a cluster retains a large fraction of its primordial BH population at late times, the energy generated via "BH burning" in the core is sufficient to delay core collapse. Only when a sufficiently large fraction of primordial BHs have been ejected through dynamical interactions within the BH-dominated core will a cluster be able to reach a core-collapsed state. By examining models with initial star counts ranging from $N = 2 \times 10^5$ to $N = 3.2 \times 10^6$, we demonstrate that the process of BH burning and eventual collapse is relevant for clusters of all realistic present-day masses.

With this model set in hand, we explored the application of these models to the formation of various objects in GCs. We briefly summarize the main results below.

1. We showed that BH–luminous companion binaries (in both detached and mass-transferring configurations) form at rates consistent with the numbers of accreting and detached BH binaries currently observed in GCs. As shown in previous work, the number of BH binaries does

not exhibit strong dependence on cluster parameters. Meanwhile, the NS binary formation rate anticorrelates with the total number of BHs in the cluster. NS binaries are most likely to form dynamically in core-collapsed clusters with small BH populations.

2. We showed that the number of pulsars (and MSPs) in a cluster is expected to depend on the BH population in a manner similar to NS binaries. In line with the previous results of Ye et al. (2019), the number of pulsars anticorrelates with the number of BHs. We demonstrate here that, for clusters of similar total mass, those with smaller initial r_v generally host more pulsars at late times compared to clusters with initially larger r_v.
3. We demonstrated that up to dozens of accreting WD binaries can form in typical GCs. These binaries may be observed as CVs or AM CVn, which are well observed in a number of GCs. Unlike NS binaries and MSPs, the numbers of accreting (and detached) WD binaries in clusters do not vary in an obvious manner with initial r_v or with the total numbers of BHs. Previous analyses have suggested that dynamical interactions may actually lead to *disruption* of CV progenitors. Furthermore, WD binary formation is particularly sensitive to assumptions about binary evolution.
4. We also explored the collision rates of WDs with other stellar remnants and discussed implications for potential high-energy transients. Because WD collisions are primarily driven dynamically (unlike CVs, for example), the number of WD collisions per cluster exhibits a clear dependence on initial r_v and BH number; core-collapsed clusters hosting few BHs at present are ideal candidates for WD collisions.
5. We discussed the number of luminous star collisions in our models. We showed that, at early times, massive MS stars and giants most frequently undergo collisions with low-mass ($M \sim 0.1\,M_{\odot}$) M dwarfs, simply because these low-mass stars dominate the assumed cluster IMF. This result may be sensitive to assumptions regarding the amount of primordial mass segregation in clusters. These various early-time stellar collisions may have important implications for BH formation, which will be explored in later work.
6. Additionally, we explored luminous star collisions that occur at late times ($t > 8$ Gyr) and discussed the implications for BS star formation. We showed that clusters can contain up to 100 BSs or more. Generally, the number of BSs is anticorrelated with the number of stellar-mass BHs. This shows that the link between BS populations and cluster dynamical age (see, e.g., Ferraro et al. 2012) is connected to stellar-mass BH populations, not independent of, as asserted in previous work (Ferraro et al. 2019).
7. Finally, we examined the number of BBH mergers in our model set. We explored the total number of mergers that occur through four distinct dynamical channels and discussed how the relative rates from these channels may depend on various cluster features. We computed cosmological BBH merger rates in our models and showed that if a large number of clusters form with small initial r_v ($r_v \lesssim 1$ pc), the BBH merger rate may be higher than previous estimates by a factor of a few. From all of our models together, we estimate a BBH merger rate of roughly $20\,\mathrm{Gyr}^{-3}\,\mathrm{yr}^{-1}$ in the local universe.

10.2. Discussion and Future Work

There are, of course, several complexities pertaining to the evolution of GCs that are not captured in the present work. In this section, we describe several such complexities and discuss avenues for future work.

In the present version of CMC, we assume fixed circular orbits within the Galactic potential. This determines the influence of the Galactic tidal field on the cluster evolution. In reality, true GC orbits are not circular (for a recent review, see Baumgardt et al. 2019), and thus the mass loss of GCs is affected also by, e.g., disk shocking and passages close to the Galactic center. The mass-loss prescriptions in the simulations presented in this work are at least moderately affected in the absence of the effect of their orbits' eccentricities and inclinations with respect to the Galactic disk (see, e.g., Baumgardt & Makino 2003, for a discussion of some of these effects). We intend to incorporate such effects in future work.

In this paper, we examined the evolution of clusters for three distinct metallicities (0.01, 0.1, and 1 $Z_{\odot}$), which overall span the range in observed metallicities of the MW GCs (see Figure 2). As discussed in Section 3, the average mass, the maximum mass, and the nature of the mass distribution of the BHs in clusters govern the dynamical evolution of both the BH subsystem and the cluster as a whole. As illustrated in Figure 1, the mass distribution of BHs varies with cluster metallicity. In particular, the BH distribution varies significantly as the metallicity approaches 0.1 $Z_{\odot}$ from 1 $Z_{\odot}$, and, since (pulsational) pair-instability SNe are assumed, the retained BH mass distribution varies relatively little between 0.1 and 0.01 $Z_{\odot}$ (see also, e.g., Belczynski et al. 2016a; Banerjee et al. 2019). Thus, an intermediate-metallicity grid point (i.e., 0.5 $Z_{\odot}$, similar to the observed metallicity of clusters in the Large Magellanic Cloud) may yield interesting extensions of the results presented in this study. Indeed, such intermediate-metallicity CMC models were computed in Chatterjee et al. (2017a), where it was shown that the metallicity can have a substantial effect on the mass distribution of BBH mergers. In the future, we plan to expand the present set of CMC models to include finer grid points that will capture such details.

Throughout this work, we demonstrated that our set of cluster models match well the bulk features of the MW GC population (see Figure 2). However, it is also worth asking if specific models from our set are able to effectively match individual observed clusters. Such an exercise was performed in Kremer et al. (2019a) using a much smaller set of CMC models (with generally identical physics). In that analysis, the CMC models were used to effectively match a small number of MW clusters with similar total mass (NGC 3201, M22, M10, and NGC 6752). In a forthcoming study (N. Z. Rui et al. 2019, in preparation), we will perform a similar exercise for this complete set of cluster models and specifically demonstrate the techniques one may use to identify which model in a large set best fits any particular observed cluster. Furthermore, recent work by Weatherford et al. (2018) used observed measurements of mass segregation to predict the number of stellar-mass BHs retained in three MW GCs with known BH candidates (M10, M22, and 47 Tuc). A follow-up analysis (Weatherford et al. 2019) implements the complete set of cluster models introduced here along with observed mass segregation

measurements for 50 GCs in the ACS Survey for MW GCs (Sarajedini et al. 2007). This work further constrains the number of BHs retained in specific GCs.

We have touched briefly here on a wide range of stellar sources that are observed in GCs, including BSs, LMXBs, MSPs, and CVs. The goal of this analysis is to simply demonstrate that, to "zeroth order," these various sources are formed in our models at rates roughly consistent with what is observed. However, more detailed analyses are necessary to explore a number of questions. For example, in the case of BSs, how do various formation channels (e.g., stellar collisions vs. binary mass transfer) contribute to the overall BS population observed in realistic clusters? How do these channels depend on various initial conditions, such as r_v and metallicity, as well as BH properties? Pertaining to MSPs, what are the binary companions expected for dynamically formed pulsars, and are the companions found in our models consistent with the array of companions (e.g., helium WDs, redbacks, black widows) identified for observed pulsars in GCs? Furthermore, what is the role of tidal capture in pulsar formation? The list of more focused topics motivated by this study's results is extensive. Indeed, several of these more detailed analyses are already underway.

We thank the anonymous referee for many helpful comments and suggestions that have improved the manuscript. We also thank Scott Coughlin for assistance setting up the CMC web platform. This work was supported by NSF grant AST-1716762 and through the computational resources and staff contributions provided for the Quest high-performance computing facility at Northwestern University. Quest is jointly supported by the Office of the Provost, the Office for Research, and Northwestern University Information Technology. This work also used computing resources at CIERA funded by NSF PHY-1726951. K.K. acknowledges support by the National Science Foundation Graduate Research Fellowship Program under grant No. DGE-1324585. C.S.Y. acknowledges support from NSF grant DGE-0948017. S.C. acknowledges support from NASA through *Chandra* award No. TM5-16004X issued by the Chandra X-ray Observatory Center (operated by the Smithsonian Astrophysical Observatory for and on behalf of NASA under contract NAS8-03060). M.S. acknowledges funding from the European Union's Horizon 2020 research and innovation program under the Marie-Sklodowska-Curie grant agreement No. 794393. G.F. acknowledges support from a CIERA Fellowship at Northwestern University.

Appendix

We include in the Appendix five tables containing more detailed information for each simulation. In Table 6, we list all initial cluster properties and various features at the end of the simulations. In Table 7, we include information concerning BH and NS binaries at late times. In Table 8, we list the total number of stellar collisions occurring in each simulation. In Table 9, we list the mean total number of WD binaries, pulsars, and blue stragglers in each simulation. In Table 10, we list the total number of binary BH mergers occurring in each simulation.

Table 6
Initial Cluster Parameters and Various Populations at End of Simulation for All Model GCs

	Simulation	N ($\times 10^5$)	r_v (pc)	R_{gc} (kpc)	Z ($Z_\odot$)	M_{tot} ($\times 10^5\ M_\odot$)	$r_{c,theoretical}$ (pc)	r_h (pc)	σ_v (km s^{-1})	N_{MS}	N_G	N_{WD}	N_{NS}	N_{BH}	N_{final}
1	N2-RV0.5-RG2-Z0.01	2	0.5	2	0.01					Disrupted					15719
2	N4-RV0.5-RG2-Z0.01	4	0.5	2	0.01					Disrupted					15719
3	N8-RV0.5-RG2-Z0.01	8	0.5	2	0.01	1.10	0.31	2.04	9.32	221131	808	54524	593	0	265985
4	N16-RV0.5-RG2-Z0.01[†]	16	0.5	2	0.01	…	…	…	…	…	…	…	…	…	…
5	N2-RV0.5-RG2-Z0.1	2	0.5	2	0.1					disrupted					15719
6	N4-RV0.5-RG2-Z0.1	4	0.5	2	0.1					disrupted					15719
7	N8-RV0.5-RG2-Z0.1	8	0.5	2	0.1	1.40	0.31	1.62	6.09	316698	1612	62257	248	1	365516
8	N16-RV0.5-RG2-Z0.1	16	0.5	2	0.1	3.70	0.29	1.13	9.92	949522	4145	153586	729	20	1062282
9	N2-RV0.5-RG2-Z1.0	2	0.5	2	1.0					disrupted					15719
10	N4-RV0.5-RG2-Z1.0	4	0.5	2	1.0					disrupted					15719
11	N8-RV0.5-RG2-Z1.0	8	0.5	2	1.0	1.40	0.11	1.23	6.82	324571	2125	50754	272	0	362588
12	N16-RV0.5-RG2-Z1.0	16	0.5	2	1.0	3.70	0.10	1.13	9.50	955147	4757	122836	762	1	1041570
13	N2-RV0.5-RG8-Z0.01	2	0.5	8	0.01					disrupted					15719
14	N4-RV0.5-RG8-Z0.01	4	0.5	8	0.01	0.20	0.88	2.67	2.69	33035	189	12864	68	0	44332
15	N8-RV0.5-RG8-Z0.01	8	0.5	8	0.01	1.90	0.14	2.39	6.15	457193	1103	74899	731	1	512605
16	N16-RV0.5-RG8-Z0.01[†]	16	0.5	8	0.01	…	…	…	…	…	…	…	…	…	…
17	N2-RV0.5-RG8-Z0.1	2	0.5	8	0.1	0.20	0.18	1.90	2.71	38505	281	9548	13	0	46328
18	N4-RV0.5-RG8-Z0.1	4	0.5	8	0.1	0.80	0.36	2.49	4.45	187675	871	32520	77	0	212383
19	N8-RV0.5-RG8-Z0.1	8	0.5	8	0.1	2.00	0.17	1.81	6.58	535190	2073	78615	278	0	591360
20	N16-RV0.5-RG8-Z0.1	16	0.5	8	0.1	4.40	0.39	1.54	9.24	1213412	4649	170036	750	52	1332749
21	N2-RV0.5-RG8-Z1.0	2	0.5	8	1.0	0.00	0.15	2.98	2.08	5537	178	2264	5	0	7879
22	N4-RV0.5-RG8-Z1.0	4	0.5	8	1.0	0.30	0.16	2.35	2.62	81778	483	11401	25	0	86161
23	N8-RV0.5-RG8-Z1.0	8	0.5	8	1.0	2.00	0.13	0.84	6.29	542329	2544	62714	252	1	583541
24	N16-RV0.5-RG8-Z1.0	16	0.5	8	1.0	4.40	0.10	1.27	8.75	1221517	5262	136408	784	4	1311062
25	N2-RV0.5-RG20-Z0.01	2	0.5	20	0.01	0.20	0.38	4.12	1.72	34507	131	9649	28	0	42509
26	N4-RV0.5-RG20-Z0.01	4	0.5	20	0.01	0.40	0.14	1.89	5.18	86713	298	20065	153	1	103167
27	N8-RV0.5-RG20-Z0.01	8	0.5	20	0.01	2.10	0.18	2.28	6.75	532153	1206	80843	801	0	590332
28	N16-RV0.5-RG20-Z0.01[†]	16	0.5	20	0.01	…	…	…	…	…	…	…	…	…	…
29	N2-RV0.5-RG20-Z0.1	2	0.5	20	0.1	0.20	0.47	2.78	1.95	44634	285	9871	11	0	52590
30	N4-RV0.5-RG20-Z0.1	4	0.5	20	0.1	0.90	0.46	3.03	3.65	221228	923	35034	75	0	247047
31	N8-RV0.5-RG20-Z0.1	8	0.5	20	0.1	2.20	0.23	1.92	7.13	598223	2214	83547	307	1	656581
32	N16-RV0.5-RG20-Z0.1	16	0.5	20	0.1	4.60	0.45	1.77	9.39	1291333	4739	174035	812	63	1411456
33	N2-RV0.5-RG20-Z1.0	2	0.5	20	1.0	0.40	0.11	1.03	2.88	100490	568	13226	19	0	109652
34	N4-RV0.5-RG20-Z1.0	4	0.5	20	1.0	1.00	0.20	1.91	5.44	271772	1284	31421	84	0	292413
35	N8-RV0.5-RG20-Z1.0	8	0.5	20	1.0	2.20	0.16	1.17	6.74	600306	2634	66031	275	1	642777
36	N16-RV0.5-RG20-Z1.0	16	0.5	20	1.0	4.60	0.13	1.25	9.35	1316742	5377	139418	765	5	1406005
37	N2-RV1-RG2-Z0.01	2	1	2	0.01					disrupted					15718
38	N4-RV1-RG2-Z0.01	4	1	2	0.01	0.10	0.10	1.58	2.22	9220	109	7677	76	0	15719
39	N8-RV1-RG2-Z0.01	8	1	2	0.01	1.70	0.33	1.92	6.56	383276	1129	72596	673	7	436917
40	N16-RV1-RG2-Z0.01	16	1	2	0.01	3.90	1.68	2.97	8.09	995346	2334	151829	1776	147	1101482
41	N2-RV1-RG2-Z0.1	2	1	2	0.1					disrupted					15719

Table 6
(Continued)

	Simulation	N ($\times 10^5$)	r_v (pc)	$R_{\rm gc}$ (kpc)	Z ($Z_\odot$)	$M_{\rm tot}$ ($\times 10^5\ M_\odot$)	$r_{c,\rm theoretical}$ (pc)	r_h (pc)	σ_v (km s^{-1})	$N_{\rm MS}$	$N_{\rm G}$	$N_{\rm WD}$	$N_{\rm NS}$	$N_{\rm BH}$	$N_{\rm final}$
42	N4-RV1-RG2-Z0.1	4	1	2	0.1	0.30	0.26	1.19	3.22	40170	549	16545	46	0	54751
43	N8-RV1-RG2-Z0.1	8	1	2	0.1	1.70	0.60	1.78	5.69	437164	2028	73153	202	20	489449
44	N16-RV1-RG2-Z0.1	16	1	2	0.1	4.00	1.07	2.52	8.51	1087257	4302	155671	555	143	1377149
45	N2-RV1-RG2-Z1.0	2	1	2	1.0					disrupted					15719
46	N4-RV1-RG2-Z1.0	4	1	2	1.0	0.10	0.02	0.11	4.64	12071	375	4097	30	1	15719
47	N8-RV1-RG2-Z1.0	8	1	2	1.0	1.80	0.06	1.09	6.71	449625	2622	62603	200	0	492832
48	N16-RV1-RG2-Z1.0	16	1	2	1.0	4.40	0.24	1.01	9.57	1176869	6000	139277	561	67	1265252
49	N2-RV1-RG8-Z0.01	2	1	8	0.01	0.20	1.03	2.59	3.27	50409	198	12157	28	0	60082
50	N4-RV1-RG8-Z0.01	4	1	8	0.01	0.90	0.49	2.50	6.20	220144	589	37821	199	1	247615
51	N8-RV1-RG8-Z0.01	8	1	8	0.01	2.20	0.65	2.26	5.69	583517	1337	85045	769	27	641429
52	N16-RV1-RG8-Z0.01	16	1	8	0.01	4.70	1.46	3.25	8.71	1239571	2679	173456	2005	183	1357141
53	N2-RV1-RG8-Z0.1	2	1	8	0.1	0.30	0.22	2.48	3.04	81654	423	14997	9	0	93045
54	N4-RV1-RG8-Z0.1	4	1	8	0.1	1.00	0.39	1.63	4.22	280957	1116	40939	67	1	308930
55	N8-RV1-RG8-Z0.1	8	1	8	0.1	2.20	0.61	2.03	5.83	617548	2306	84467	237	25	673931
56	N16-RV1-RG8-Z0.1	16	1	8	0.1	4.60	1.25	2.73	8.28	1302983	4799	172926	610	189	1418183
57	N2-RV1-RG8-Z1.0	2	1	8	1.0	0.40	0.12	1.64	2.81	104888	581	13949	5	0	114515
58	N4-RV1-RG8-Z1.0	4	1	8	1.0	1.00	0.11	1.71	4.19	280702	1355	32887	63	0	301996
59	N8-RV1-RG8-Z1.0	8	1	8	1.0	2.30	0.10	1.11	6.76	639517	2992	70660	219	7	683127
60	N16-RV1-RG8-Z1.0	16	1	8	1.0	4.90	0.34	1.15	9.46	1377732	6276	146443	563	94	1465649
61	N2-RV1-RG20-Z0.01	2	1	20	0.01	0.40	0.44	3.56	3.12	100873	276	17439	47	0	113732
62	N4-RV1-RG20-Z0.01	4	1	20	0.01	0.90	0.75	3.10	3.58	216736	573	36943	184	0	243741
63	N8-RV1-RG20-Z0.01	8	1	20	0.01	2.40	0.97	2.55	8.19	633461	1393	88343	791	24	692627
64	N16-RV1-RG20-Z0.01	16	1	20	0.01	4.90	1.60	3.47	8.61	1314978	2780	177177	2049	214	1430591
65	N2-RV1-RG20-Z0.1	2	1	20	0.1	0.40	0.08	2.61	3.36	90289	455	15250	11	1	101592
66	N4-RV1-RG20-Z0.1	4	1	20	0.1	1.10	0.36	2.23	4.60	305006	1152	42204	81	1	333348
67	N8-RV1-RG20-Z0.1	8	1	20	0.1	2.30	0.98	2.25	6.06	659786	2365	86974	243	33	717040
68	N16-RV1-RG20-Z0.1	16	1	20	0.1	4.80	1.43	2.99	8.99	1357309	4855	176878	616	217	1474265
69	N2-RV1-RG20-Z1.0	2	1	20	1.0	0.50	0.17	1.67	3.08	137577	656	15837	18	0	147736
70	N4-RV1-RG20-Z1.0	4	1	20	1.0	1.10	0.08	1.19	4.16	315257	1435	34601	73	2	336743
71	N8-RV1-RG20-Z1.0	8	1	20	1.0	2.40	0.11	1.37	6.81	683933	3058	72346	220	12	727459
72	N16-RV1-RG20-Z1.0	16	1	20	1.0	5.00	0.36	1.12	9.80	1430711	6386	148170	578	108	1518535
73	N2-RV2-RG2-Z0.01	2	2	2	0.01					disrupted					15719
74	N4-RV2-RG2-Z0.01	4	2	2	0.01	0.20	0.21	1.27	3.83	17153	175	12238	65	0	28091
75	N8-RV2-RG2-Z0.01	8	2	2	0.01	1.50	1.99	3.36	5.00	365880	1074	66401	417	47	413975
76	N16-RV2-RG2-Z0.01	16	2	2	0.01	3.90	3.62	5.17	6.82	1024891	2284	148100	1281	418	1125828
77	N2-RV2-RG2-Z0.1	2	2	2	0.1					disrupted					15719
78	N4-RV2-RG2-Z0.1	4	2	2	0.1	0.30	0.15	1.06	3.66	41352	554	17272	28	1	55744
79	N8-RV2-RG2-Z0.1	8	2	2	0.1	1.60	2.44	3.58	4.75	400030	1850	66439	112	72	447165
80	N16-RV2-RG2-Z0.1	16	2	2	0.1	4.10	3.07	4.39	7.03	1137096	4279	154147	371	418	1240077
81	N2-RV2-RG2-Z1.0	2	2	2	1.0					disrupted					15719

Table 6
(Continued)

	Simulation	N ($\times 10^5$)	r_v (pc)	$R_{\rm gc}$ (kpc)	Z ($Z_\odot$)	$M_{\rm tot}$ ($\times 10^5\ M_\odot$)	$r_{c,\rm theoretical}$ (pc)	r_h (pc)	σ_v (km s^{-1})	$N_{\rm MS}$	$N_{\rm G}$	$N_{\rm WD}$	$N_{\rm NS}$	$N_{\rm BH}$	$N_{\rm final}$
82	N4-RV2-RG2-Z1.0	4	2	2	1.0	0.50	0.13	0.97	4.10	85234	1154	22241	46	3	102859
83	N8-RV2-RG2-Z1.0	8	2	2	1.0	2.00	0.55	1.91	5.10	515156	2926	66265	157	86	558122
84	N16-RV2-RG2-Z1.0	16	2	2	1.0	4.70	1.06	2.29	8.24	1307924	6278	143468	418	360	1394809
85	N2-RV2-RG8-Z0.01	2	2	8	0.01	0.50	0.51	2.50	3.24	112783	303	19537	25	0	126328
86	N4-RV2-RG8-Z0.01	4	2	8	0.01	1.10	1.27	3.57	3.56	279165	666	41776	150	9	307164
87	N8-RV2-RG8-Z0.01	8	2	8	0.01	2.30	2.31	4.51	5.27	618244	1369	85609	494	93	674796
88	N16-RV2-RG8-Z0.01	16	2	8	0.01	4.80	3.35	5.75	7.72	1275522	2730	174385	1602	534	1392285
89	N2-RV2-RG8-Z0.1	2	2	8	0.1	0.40	0.17	1.98	2.18	115689	504	18079	6	0	128413
90	N4-RV2-RG8-Z0.1	4	2	8	0.1	1.10	1.14	2.92	3.51	297896	1153	41177	44	11	324896
91	N8-RV2-RG8-Z0.1	8	2	8	0.1	2.30	2.82	3.86	4.79	654814	2346	85668	160	89	710590
92	N16-RV2-RG8-Z0.1	16	2	8	0.1	4.80	3.13	4.97	7.40	1343418	4791	173770	452	478	1457480
93	N2-RV2-RG8-Z1.0	2	2	8	1.0	0.50	0.39	1.76	2.71	142238	751	16966	9	3	152734
94	N4-RV2-RG8-Z1.0	4	2	8	1.0	1.20	0.65	2.10	3.87	329861	1599	35810	45	32	351198
95	N8-RV2-RG8-Z1.0	8	2	8	1.0	2.50	0.73	2.05	5.56	704393	3217	73327	161	121	747356
96	N16-RV2-RG8-Z1.0	16	2	8	1.0	5.10	1.11	2.23	7.92	1456068	6523	149126	484	360	1543088
97	N2-RV2-RG20-Z0.01	2	2	20	0.01	0.50	0.48	3.27	2.67	131819	317	20531	33	2	145647
98	N4-RV2-RG20-Z0.01	4	2	20	0.01	1.20	2.57	3.29	3.86	316980	696	43948	142	8	345573
99	N8-RV2-RG20-Z0.01	8	2	20	0.01	2.40	2.62	4.97	4.91	657018	1424	89056	542	94	715412
100	N16-RV2-RG20-Z0.01	16	2	20	0.01	5.00	4.82	5.52	7.42	1344240	2832	181373	1668	502	1464969
101	N2-RV2-RG20-Z0.1	2	2	20	0.1	0.50	0.63	2.58	2.75	149969	587	20628	6	3	163444
102	N4-RV2-RG20-Z0.1	4	2	20	0.1	1.20	1.37	3.37	3.31	327950	1184	43009	46	15	355655
103	N8-RV2-RG20-Z0.1	8	2	20	0.1	2.40	2.29	4.19	5.00	678654	2381	87079	171	123	734958
104	N16-RV2-RG20-Z0.1	16	2	20	0.1	4.90	2.56	4.96	10.22	1386308	4936	177962	450	503	1502959
105	N2-RV2-RG20-Z1.0	2	2	20	1.0	0.60	0.36	1.33	2.62	168168	772	17759	18	3	178496
106	N4-RV2-RG20-Z1.0	4	2	20	1.0	1.20	1.18	2.23	3.79	354679	1620	36591	52	29	375872
107	N8-RV2-RG20-Z1.0	8	2	20	1.0	2.50	0.98	2.38	5.55	730566	3246	74113	166	119	773267
108	N16-RV2-RG20-Z1.0	16	2	20	1.0	5.10	0.96	2.37	9.20	1479067	6533	149816	488	403	1565984
109	N2-RV4-RG2-Z0.01	2	4	2	0.01					disrupted					14508
110	N4-RV4-RG2-Z0.01	4	4	2	0.01					disrupted					9884
111	N8-RV4-RG2-Z0.01	8	4	2	0.01					disrupted					77728
112	N16-RV4-RG2-Z0.01	16	4	2	0.01	2.40	7.75	7.52	4.43	574874	1428	95511	560	778	643215
113	N2-RV4-RG2-Z0.1	2	4	2	0.1					disrupted					14923
114	N4-RV4-RG2-Z0.1	4	4	2	0.1					disrupted					11270
115	N8-RV4-RG2-Z0.1	8	4	2	0.1					disrupted					6075
116	N16-RV4-RG2-Z0.1	16	4	2	0.1	3.30	5.89	7.35	6.68	859255	3424	123785	233	814	943294
117	N2-RV4-RG2-Z1.0	2	4	2	1.0					disrupted					15697
118	N4-RV4-RG2-Z1.0	4	4	2	1.0					disrupted					15714
119	N8-RV4-RG2-Z1.0	8	4	2	1.0	1.40	3.55	3.38	4.21	317646	2360	50098	39	248	352284
120	N16-RV4-RG2-Z1.0	16	4	2	1.0	4.50	2.78	4.31	6.97	1244082	6055	137066	191	740	1326141
121	N2-RV4-RG8-Z0.01	2	4	8	0.01	0.40	2.40	4.49	1.72	97753	264	17271	17	3	109547

Table 6
(Continued)

	Simulation	N ($\times 10^5$)	r_v (pc)	$R_{\rm gc}$ (kpc)	Z ($Z_\odot$)	$M_{\rm tot}$ ($\times 10^5\ M_\odot$)	$r_{c,\rm theoretical}$ (pc)	r_h (pc)	σ_v (km s^{-1})	$N_{\rm MS}$	$N_{\rm G}$	$N_{\rm WD}$	$N_{\rm NS}$	$N_{\rm BH}$	$N_{\rm final}$
122	N4-RV4-RG8-Z0.01	4	4	8	0.01	1.10	3.84	6.77	3.01	285876	639	40700	46	44	311954
123	N8-RV4-RG8-Z0.01	8	4	8	0.01	2.40	3.67	8.10	4.47	635823	1380	85662	261	294	690891
124	N16-RV4-RG8-Z0.01	16	4	8	0.01	5.00	7.24	8.55	6.88	1327711	2784	177202	1057	1008	1443059
125	N2-RV4-RG8-Z0.1	2	4	8	0.1	0.40	2.79	5.52	1.85	119190	513	18000	4	6	131062
126	N4-RV4-RG8-Z0.1	4	4	8	0.1	1.10	3.67	6.66	2.97	304908	1117	40580	20	47	330726
127	N8-RV4-RG8-Z0.1	8	4	8	0.1	2.30	4.66	7.12	4.49	661605	2358	84716	75	269	715520
128	N16-RV4-RG8-Z0.1	16	4	8	0.1	4.90	6.26	7.69	6.43	1369462	4886	174686	334	914	1482084
129	N2-RV4-RG8-Z1.0	2	4	8	1.0	0.50	1.76	4.85	1.82	148704	745	17109	2	27	158950
130	N4-RV4-RG8-Z1.0	4	4	8	1.0	1.20	1.72	4.04	3.32	347318	1613	36061	18	113	367794
131	N8-RV4-RG8-Z1.0	8	4	8	1.0	2.50	2.90	4.78	4.72	731599	3251	73829	70	303	773337
132	N16-RV4-RG8-Z1.0	16	4	8	1.0	5.20	1.96	4.69	6.87	1488087	6549	150042	256	776	1573612
133	N2-RV4-RG20-Z0.01	2	4	20	0.01	0.60	2.68	5.00	2.16	149394	317	21155	16	9	162744
134	N4-RV4-RG20-Z0.01	4	4	20	0.01	1.20	5.41	7.75	3.02	322954	704	43847	75	53	350621
135	N8-RV4-RG20-Z0.01	8	4	20	0.01	2.50	6.72	8.21	4.54	672648	1427	89537	271	330	729944
136	N16-RV4-RG20-Z0.01	16	4	20	0.01	5.20	6.94	8.75	6.63	1373006	2839	182327	1099	1036	1491773
137	N2-RV4-RG20-Z0.1	2	4	20	0.1	0.60	1.62	4.60	2.25	156780	584	20711	8	8	169795
138	N4-RV4-RG20-Z0.1	4	4	20	0.1	1.20	5.77	6.55	3.03	329794	1187	42675	22	55	356593
139	N8-RV4-RG20-Z0.1	8	4	20	0.1	2.40	6.31	7.97	4.48	693645	2437	87763	106	285	749357
140	N16-RV4-RG20-Z0.1	16	4	20	0.1	5.00	5.87	7.74	6.51	1417843	5005	179354	345	957	1533435
141	N2-RV4-RG20-Z1.0	2	4	20	1.0	0.60	1.98	4.31	2.07	179146	787	18142	5	38	189143
142	N4-RV4-RG20-Z1.0	4	4	20	1.0	1.30	2.13	4.60	3.23	368729	1636	36939	19	111	389277
143	N8-RV4-RG20-Z1.0	8	4	20	1.0	2.60	2.59	4.69	5.06	745125	3278	74454	84	323	786950
144	N16-RV4-RG20-Z1.0	16	4	20	1.0	5.20	2.86	5.16	7.95	1496449	6587	150482	259	791	1582117
145	N32-RV1-RG20-Z0.01	32	1	20	0.01	10.00	2.01	4.23	14.71	2668299	5669	362665	4900	852	3071351
146	N32-RV2-RG20-Z0.01	32	2	20	0.01	10.30	3.95	6.15	11.91	2725951	5720	365278	4144	1714	3039922
147	N32-RV1-RG20-Z1.0	32	1	20	1.0	10.10	0.48	1.25	13.79	2916889	12819	297140	1411	518	3147560
148	N32-RV2-RG20-Z1.0	32	2	20	1.0	10.40	1.14	2.49	12.46	2980508	13129	299958	1349	1165	3155027

Note. The final cluster mass $M_{\rm tot}$, core radius r_c, half-light radius r_h, central velocity dispersion σ_v, and number of main-sequence stars $N_{\rm MS}$, giants $N_{\rm G}$, white dwarfs $N_{\rm WD}$, neutron stars $N_{\rm NS}$, and black holes $N_{\rm BH}$ for each model. Models marked with a dagger (†) indicates that the model was stopped owing to onset of collisional runaway (see Section 2.3).

Table 7
Mean Numbers of Black Hole and Neutron Star Binaries in All Models at Late Times

			Detached			Accreting				Detached			Accreting		
	Simulation	BH	BH–MS	BH–G	BH–WD	BH–MS	BH–G	BH–WD	NS	NS–MS	NS–G	NS–WD	NS–MS	NS–G	NS–WD
1	N2-RV0.5-RG2-Z0.01	…		disrupted			…		…		disrupted			…	
2	N4-RV0.5-RG2-Z0.01	…		disrupted			…		…		disrupted			…	
3	N8-RV0.5-RG2-Z0.01	0	0.00	0.00	0.00	0.00	0.00	0.00	658	0.75	0.00	2.64	0.04	0.04	2.70
4	N16-RV0.5-RG2-Z0.01[†]	…	…	…	…	…	…	…	…	…	…	…	…	…	…
5	N2-RV0.5-RG2-Z0.1	…		disrupted			…		…		disrupted			…	
6	N4-RV0.5-RG2-Z0.1	…		disrupted			…		…		disrupted			…	
7	N8-RV0.5-RG2-Z0.1	0	0.00	0.00	0.00	0.00	0.00	0.00	262	1.09	0.00	1.31	0.01	0.04	3.04
8	N16-RV0.5-RG2-Z0.1	50	2.15	0.00	0.75	1.21	0.02	0.00	732	2.98	0.00	0.79	0.00	0.23	6.65
9	N2-RV0.5-RG2-Z1.0	…		disrupted			…		…		disrupted			…	
10	N4-RV0.5-RG2-Z1.0	…		disrupted			…		…		disrupted			…	
11	N8-RV0.5-RG2-Z1.0	0	0.00	0.00	0.00	0.00	0.00	0.00	285	1.74	0.00	0.38	0.73	0.10	6.10
12	N16-RV0.5-RG2-Z1.0	2	0.22	0.00	0.03	0.08	0.03	0.07	743	3.88	0.00	1.22	2.68	0.17	11.21
13	N2-RV0.5-RG8-Z0.01	…		disrupted			…		…		disrupted			…	
14	N4-RV0.5-RG8-Z0.01	0	0.00	0.00	0.00	0.00	0.00	0.00	96	0.01	0.00	0.51	0.00	0.00	0.01
15	N8-RV0.5-RG8-Z0.01	2	0.01	0.00	0.28	0.00	0.00	0.08	782	3.73	0.00	3.76	1.01	0.03	3.82
16	N16-RV0.5-RG8-Z0.01[†]	…	…	…	…	…	…	…	…	…	…	…	…	…	…
17	N2-RV0.5-RG8-Z0.1	0	0.00	0.00	0.00	0.00	0.00	0.00	17	0.11	0.00	0.05	0.00	0.00	0.00
18	N4-RV0.5-RG8-Z0.1	0	0.00	0.00	0.00	0.00	0.00	0.00	87	0.18	0.00	0.35	0.00	0.00	0.13
19	N8-RV0.5-RG8-Z0.1	2	0.16	0.00	0.25	0.06	0.00	0.01	284	2.24	0.00	2.12	0.30	0.07	2.21
20	N16-RV0.5-RG8-Z0.1	73	1.33	0.00	0.09	0.25	0.00	0.00	753	4.76	0.00	0.15	0.00	0.00	6.00
21	N2-RV0.5-RG8-Z1.0	0	0.00	0.00	0.00	0.00	0.00	0.00	10	0.00	0.00	0.00	0.00	0.00	0.00
22	N4-RV0.5-RG8-Z1.0	0	0.00	0.00	0.00	0.00	0.00	0.00	27	0.36	0.00	0.02	0.00	0.00	0.01
23	N8-RV0.5-RG8-Z1.0	1	0.37	0.00	0.23	0.12	0.10	0.12	264	4.32	0.00	0.46	0.44	0.00	3.28
24	N16-RV0.5-RG8-Z1.0	10	0.58	0.00	0.29	0.15	0.12	0.19	751	4.43	0.00	1.46	0.98	0.25	7.06
25	N2-RV0.5-RG20-Z0.01	0	0.00	0.00	0.00	0.00	0.00	0.00	36	0.08	0.00	0.12	0.00	0.00	0.01
26	N4-RV0.5-RG20-Z0.01	1	0.05	0.00	0.75	0.06	0.02	0.04	168	0.06	0.00	0.25	0.00	0.00	0.19
27	N8-RV0.5-RG20-Z0.01	0	0.00	0.00	0.08	0.00	0.00	0.00	849	3.21	0.00	5.58	1.30	0.01	2.00
28	N16-RV0.5-RG20-Z0.01[†]	…	…	…	…	…	…	…	…	…	…	…	…	…	…
29	N2-RV0.5-RG20-Z0.1	0	0.00	0.00	0.00	0.00	0.00	0.00	14	0.03	0.00	0.10	0.00	0.00	1.11
30	N4-RV0.5-RG20-Z0.1	0	0.00	0.00	0.00	0.00	0.00	0.00	81	0.25	0.00	0.25	0.00	0.04	1.04
31	N8-RV0.5-RG20-Z0.1	4	0.29	0.00	0.59	0.04	0.00	0.03	310	2.10	0.00	2.68	0.03	0.15	1.07
32	N16-RV0.5-RG20-Z0.1	94	1.36	0.00	0.36	0.97	0.02	0.00	812	2.40	0.00	1.02	1.00	0.22	11.03
33	N2-RV0.5-RG20-Z1.0	0	0.00	0.00	0.00	0.00	0.00	0.00	20	0.17	0.00	0.00	0.10	0.00	0.08
34	N4-RV0.5-RG20-Z1.0	0	0.00	0.00	0.00	0.00	0.00	0.00	87	0.29	0.00	0.46	0.03	0.08	0.86
35	N8-RV0.5-RG20-Z1.0	4	0.25	0.00	0.36	0.09	0.06	0.02	281	1.58	0.00	1.18	0.61	0.19	2.25
36	N16-RV0.5-RG20-Z1.0	9	0.41	0.00	0.37	0.64	0.04	0.01	748	4.00	0.00	2.73	1.87	0.25	8.97
37	N2-RV1-RG2-Z0.01	…		disrupted			…		…		disrupted			…	
38	N4-RV1-RG2-Z0.01	0	0.00	0.00	0.00	0.00	0.00	0.00	132	0.27	0.00	0.76	0.00	0.01	0.09
39	N8-RV1-RG2-Z0.01	13	1.06	0.00	0.56	0.33	0.00	0.00	677	2.94	0.00	1.00	0.00	0.06	0.00
40	N16-RV1-RG2-Z0.01	208	0.68	0.00	0.29	3.00	0.00	0.00	1790	1.00	0.00	0.00	0.00	0.00	1.00

Table 7
(Continued)

			Detached			Accreting				Detached			Accreting		
	Simulation	BH	BH–MS	BH–G	BH–WD	BH–MS	BH–G	BH–WD	NS	NS–MS	NS–G	NS–WD	NS–MS	NS–G	NS–WD
41	N2-RV1-RG2-Z0.1	…		disrupted			…		…		disrupted			…	
42	N4-RV1-RG2-Z0.1	0	0.00	0.00	0.00	0.00	0.00	0.00	55	0.45	0.00	0.44	0.00	0.01	0.07
43	N8-RV1-RG2-Z0.1	27	1.10	0.00	0.30	1.90	0.00	0.03	202	1.50	0.00	0.23	0.00	0.00	1.00
44	N16-RV1-RG2-Z0.1	201	1.05	0.00	0.12	0.14	0.00	0.00	555	0.00	0.00	0.56	0.00	0.00	3.00
45	N2-RV1-RG2-Z1.0	…		disrupted			…		…		disrupted			…	
46	N4-RV1-RG2-Z1.0	1	0.28	0.00	0.46	0.10	0.09	0.06	44	0.36	0.00	0.02	0.00	0.02	0.01
47	N8-RV1-RG2-Z1.0	12	0.56	0.00	0.37	0.07	0.12	0.09	198	1.53	0.00	1.56	0.05	0.00	1.81
48	N16-RV1-RG2-Z1.0	140	5.30	0.00	0.76	1.39	0.65	0.17	563	2.91	0.00	0.11	0.00	0.02	2.30
49	N2-RV1-RG8-Z0.01	0	0.00	0.00	0.00	0.00	0.00	0.00	34	0.00	0.00	0.34	0.00	0.00	0.00
50	N4-RV1-RG8-Z0.01	1	0.11	0.00	0.70	0.10	0.00	0.04	212	0.54	0.00	1.20	0.96	0.00	1.28
51	N8-RV1-RG8-Z0.01	34	0.42	0.00	0.26	1.42	0.00	0.00	774	0.74	0.00	0.00	0.00	0.00	1.00
52	N16-RV1-RG8-Z0.01	246	1.74	0.00	0.18	1.00	0.00	0.00	2019	3.30	0.00	2.19	0.00	0.00	3.00
53	N2-RV1-RG8-Z0.1	1	0.16	0.00	0.31	0.07	0.00	0.05	12	0.06	0.00	0.09	0.00	0.00	0.00
54	N4-RV1-RG8-Z0.1	3	0.33	0.00	0.38	0.00	0.00	0.00	69	0.05	0.00	0.14	0.00	0.00	0.00
55	N8-RV1-RG8-Z0.1	33	1.96	0.00	0.15	0.19	0.04	0.00	238	0.77	0.00	0.00	0.00	0.00	0.00
56	N16-RV1-RG8-Z0.1	233	1.18	0.00	0.15	2.74	0.01	0.00	613	0.00	0.00	1.00	0.00	0.00	3.00
57	N2-RV1-RG8-Z1.0	0	0.00	0.00	0.00	0.00	0.00	0.00	6	0.00	0.00	0.05	0.17	0.00	0.07
58	N4-RV1-RG8-Z1.0	1	0.08	0.00	0.03	0.32	0.05	0.00	65	0.50	0.00	0.11	0.00	0.03	2.34
59	N8-RV1-RG8-Z1.0	22	2.06	0.00	0.44	0.06	0.12	0.65	219	2.03	0.00	0.12	0.18	0.06	1.41
60	N16-RV1-RG8-Z1.0	151	3.85	0.00	1.02	3.34	0.34	0.41	564	5.05	0.00	1.66	1.00	0.00	2.29
61	N2-RV1-RG20-Z0.01	0	0.00	0.00	0.00	0.00	0.00	0.00	50	0.00	0.00	0.48	0.00	0.00	0.00
62	N4-RV1-RG20-Z0.01	0	0.00	0.00	0.00	0.00	0.00	0.00	205	1.88	0.00	2.08	0.02	0.00	0.18
63	N8-RV1-RG20-Z0.01	34	1.08	0.00	0.38	0.00	0.00	0.00	796	2.50	0.00	0.00	0.00	0.00	0.00
64	N16-RV1-RG20-Z0.01	268	1.94	0.00	0.28	0.38	0.00	0.00	2053	0.00	0.00	0.00	0.00	0.00	1.00
65	N2-RV1-RG20-Z0.1	1	0.15	0.00	0.54	0.30	0.00	0.01	13	0.01	0.00	0.04	0.00	0.00	0.00
66	N4-RV1-RG20-Z0.1	2	0.16	0.00	0.00	1.00	0.00	0.00	82	0.96	0.00	1.24	0.00	0.00	0.00
67	N8-RV1-RG20-Z0.1	45	0.97	0.00	0.24	2.00	0.12	0.00	245	1.06	0.00	0.00	0.00	0.00	0.00
68	N16-RV1-RG20-Z0.1	266	1.29	0.00	0.07	1.46	0.00	0.00	618	1.00	0.00	0.00	0.00	0.00	3.75
69	N2-RV1-RG20-Z1.0	1	0.06	0.00	0.34	0.14	0.00	0.00	19	0.00	0.00	0.00	0.00	0.00	0.00
70	N4-RV1-RG20-Z1.0	4	0.50	0.00	0.12	0.80	0.17	0.00	75	0.30	0.00	0.70	0.00	0.05	1.00
71	N8-RV1-RG20-Z1.0	24	1.04	0.00	0.30	0.81	0.48	0.00	220	2.85	0.00	0.48	0.00	0.33	2.22
72	N16-RV1-RG20-Z1.0	170	4.58	0.00	0.40	1.77	0.40	0.07	577	4.72	0.00	1.98	0.00	0.03	2.40
73	N2-RV2-RG2-Z0.01	…		disrupted			…		…		disrupted			…	
74	N4-RV2-RG2-Z0.01	2	0.13	0.00	0.18	0.00	0.00	0.00	82	0.63	0.00	0.32	0.00	0.00	0.03
75	N8-RV2-RG2-Z0.01	73	1.50	0.00	0.46	0.00	0.00	0.00	426	0.00	0.00	0.00	0.00	0.00	0.00
76	N16-RV2-RG2-Z0.01	496	3.31	0.00	1.13	0.00	0.01	0.00	1315	4.00	0.00	0.00	0.00	0.00	0.00
77	N2-RV2-RG2-Z0.1	…		disrupted			…		…		disrupted			…	
78	N4-RV2-RG2-Z0.1	3	0.21	0.00	0.58	0.00	0.00	0.00	30	0.05	0.00	0.74	0.00	0.00	0.00
79	N8-RV2-RG2-Z0.1	100	2.13	0.00	0.20	0.00	0.03	0.00	114	0.00	0.00	1.00	0.00	0.00	0.00
80	N16-RV2-RG2-Z0.1	498	3.26	0.00	0.16	0.00	0.15	0.04	376	0.00	0.00	0.00	0.00	0.00	1.00

Table 7
(Continued)

			Detached			Accreting				Detached			Accreting		
	Simulation	BH	BH–MS	BH–G	BH–WD	BH–MS	BH–G	BH–WD	NS	NS–MS	NS–G	NS–WD	NS–MS	NS–G	NS–WD
81	N2-RV2-RG2-Z1.0	…		disrupted			…		…		disrupted			…	
82	N4-RV2-RG2-Z1.0	20	1.59	0.00	0.18	0.00	0.00	0.00	47	0.00	0.00	0.00	0.00	0.00	1.00
83	N8-RV2-RG2-Z1.0	123	1.92	0.00	0.08	0.69	0.08	0.00	158	1.35	0.00	0.19	0.00	0.38	2.00
84	N16-RV2-RG2-Z1.0	437	3.26	0.00	0.04	0.33	0.00	0.04	420	2.23	0.00	0.00	0.00	0.00	1.00
85	N2-RV2-RG8-Z0.01	2	0.00	0.00	0.20	0.00	0.00	0.00	25	0.00	0.00	0.00	0.00	0.00	0.00
86	N4-RV2-RG8-Z0.01	14	1.00	0.00	0.73	0.00	0.00	0.00	151	0.00	0.00	0.00	0.00	0.00	0.00
87	N8-RV2-RG8-Z0.01	117	2.12	0.00	0.56	0.00	0.00	0.00	495	1.00	0.00	0.00	0.00	0.00	1.00
88	N16-RV2-RG8-Z0.01	614	2.43	0.00	0.07	1.23	0.00	0.00	1620	1.27	0.00	0.51	0.00	0.13	0.01
89	N2-RV2-RG8-Z0.1	0	0.00	0.00	0.00	0.00	0.00	0.00	6	0.00	0.00	0.06	0.00	0.00	0.00
90	N4-RV2-RG8-Z0.1	15	1.00	0.00	0.33	0.00	0.08	0.00	44	0.00	0.00	0.00	0.00	0.00	0.00
91	N8-RV2-RG8-Z0.1	119	2.45	0.00	0.26	0.00	0.00	0.00	161	0.00	0.00	0.00	0.00	0.00	1.00
92	N16-RV2-RG8-Z0.1	551	0.92	0.00	0.06	0.00	0.00	0.00	452	0.00	0.00	0.00	0.00	0.00	3.00
93	N2-RV2-RG8-Z1.0	9	0.42	0.00	0.00	0.00	0.00	0.00	9	0.00	0.00	0.00	0.00	0.00	0.00
94	N4-RV2-RG8-Z1.0	50	2.72	0.00	0.28	0.00	0.00	0.00	46	0.00	0.00	0.00	0.00	0.00	0.00
95	N8-RV2-RG8-Z1.0	152	2.10	0.00	0.10	0.21	0.00	0.00	161	0.79	0.00	0.00	0.00	0.00	2.00
96	N16-RV2-RG8-Z1.0	446	4.04	0.00	0.00	0.17	0.00	0.00	483	0.03	0.00	0.00	0.00	0.00	1.00
97	N2-RV2-RG20-Z0.01	3	0.63	0.00	0.00	0.00	0.00	0.00	34	0.00	0.00	0.00	0.00	0.00	0.00
98	N4-RV2-RG20-Z0.01	13	0.55	0.00	0.64	0.00	0.09	0.00	142	0.00	0.00	0.00	0.00	0.00	0.00
99	N8-RV2-RG20-Z0.01	119	1.97	0.00	0.29	0.00	0.00	0.00	543	0.00	0.00	0.00	0.00	0.00	0.00
100	N16-RV2-RG20-Z0.01	597	3.34	0.00	1.19	3.28	0.11	0.00	1676	2.12	0.00	0.01	0.00	0.02	0.00
101	N2-RV2-RG20-Z0.1	3	0.00	0.00	0.00	0.00	0.00	0.00	6	0.00	0.00	0.00	0.00	0.00	0.00
102	N4-RV2-RG20-Z0.1	19	0.73	0.00	0.18	0.00	0.00	0.00	47	0.00	0.00	2.00	0.00	0.00	0.00
103	N8-RV2-RG20-Z0.1	143	1.39	0.00	0.18	1.00	0.00	0.00	171	0.00	0.00	1.00	0.00	0.00	0.00
104	N16-RV2-RG20-Z0.1	590	1.31	0.00	0.02	0.77	0.00	0.00	451	0.04	0.00	0.00	0.00	0.00	2.00
105	N2-RV2-RG20-Z1.0	9	1.10	0.00	0.40	0.00	0.00	0.00	18	0.40	0.00	0.10	0.00	0.00	0.00
106	N4-RV2-RG20-Z1.0	43	1.00	0.00	0.07	1.00	0.27	0.00	52	0.00	0.00	0.00	0.00	0.00	0.00
107	N8-RV2-RG20-Z1.0	150	2.31	0.00	0.12	0.23	0.12	0.15	167	0.00	0.00	0.58	0.00	0.00	2.00
108	N16-RV2-RG20-Z1.0	483	2.38	0.00	0.01	2.74	0.01	0.26	490	0.78	0.00	0.19	0.00	0.20	1.00
109	N2-RV4-RG2-Z0.01	…		disrupted			…		…		disrupted			…	
110	N4-RV4-RG2-Z0.01	…		disrupted			…		…		disrupted			…	
111	N8-RV4-RG2-Z0.01	…		disrupted			…		…		disrupted			…	
112	N16-RV4-RG2-Z0.01	891	2.34	0.00	0.12	0.93	0.00	0.00	669	0.00	0.00	0.00	0.00	0.00	0.00
113	N2-RV4-RG2-Z0.1	…		disrupted			…		…		disrupted			…	
114	N4-RV4-RG2-Z0.1	…		disrupted			…		…		disrupted			…	
115	N8-RV4-RG2-Z0.1	…		disrupted			…		…		disrupted			…	
116	N16-RV4-RG2-Z0.1	908	2.29	0.00	0.09	0.23	0.00	0.00	249	0.00	0.00	0.00	0.00	0.00	1.00
117	N2-RV4-RG2-Z1.0	…		disrupted			…		…		disrupted			…	
118	N4-RV4-RG2-Z1.0	…		disrupted			…		…		disrupted			…	
119	N8-RV4-RG2-Z1.0	295	2.47	0.00	0.03	0.00	0.15	0.03	40	0.00	0.00	0.00	0.00	0.00	0.00
120	N16-RV4-RG2-Z1.0	816	2.49	0.00	0.00	1.56	0.00	0.00	193	0.00	0.00	0.00	0.00	0.00	0.00

Table 7
(Continued)

			Detached			Accreting				Detached			Accreting		
	Simulation	BH	BH–MS	BH–G	BH–WD	BH–MS	BH–G	BH–WD	NS	NS–MS	NS–G	NS–WD	NS–MS	NS–G	NS–WD
121	N2-RV4-RG8-Z0.01	7	1.70	0.00	1.00	0.00	0.00	0.00	17	0.10	0.00	0.00	0.00	0.00	0.00
122	N4-RV4-RG8-Z0.01	55	5.80	0.00	1.27	0.00	0.00	0.00	47	0.00	0.00	0.00	0.00	0.00	0.00
123	N8-RV4-RG8-Z0.01	334	3.63	0.00	0.30	0.00	0.00	0.00	265	1.00	0.00	1.00	0.00	0.00	0.00
124	N16-RV4-RG8-Z0.01	1098	4.96	0.00	0.06	0.00	0.00	0.00	1075	0.00	0.00	0.00	0.00	0.00	0.00
125	N2-RV4-RG8-Z0.1	8	1.29	0.00	0.29	0.00	0.00	0.00	4	0.00	0.00	0.00	0.00	0.00	0.00
126	N4-RV4-RG8-Z0.1	67	3.12	0.00	0.65	0.00	0.00	0.00	21	0.00	0.00	0.00	0.00	0.00	0.00
127	N8-RV4-RG8-Z0.1	312	2.47	0.00	0.28	0.00	0.00	0.00	75	0.00	0.00	0.00	0.00	0.00	1.00
128	N16-RV4-RG8-Z0.1	990	1.62	0.00	0.03	1.44	0.00	0.00	337	0.00	0.00	0.00	0.00	0.00	3.00
129	N2-RV4-RG8-Z1.0	32	1.00	0.00	0.00	0.00	0.00	0.00	2	0.00	0.00	0.00	0.00	0.00	0.00
130	N4-RV4-RG8-Z1.0	135	1.12	0.00	0.00	0.00	0.00	0.00	18	0.00	0.00	0.00	0.00	0.00	0.00
131	N8-RV4-RG8-Z1.0	344	1.97	0.00	0.00	0.00	0.00	0.00	70	0.00	0.00	0.00	0.00	0.00	0.00
132	N16-RV4-RG8-Z1.0	844	3.30	0.00	0.18	0.00	0.50	0.11	258	0.00	0.00	0.00	0.00	0.00	2.00
133	N2-RV4-RG20-Z0.01	13	2.40	0.00	1.00	0.00	0.00	0.00	16	0.00	0.00	0.00	0.00	0.00	0.00
134	N4-RV4-RG20-Z0.01	69	4.62	0.00	1.38	0.00	0.00	0.00	75	0.00	0.00	0.00	0.00	0.00	0.00
135	N8-RV4-RG20-Z0.01	377	5.29	0.00	0.46	0.00	0.00	0.00	272	0.00	0.00	0.00	0.00	0.00	0.00
136	N16-RV4-RG20-Z0.01	1112	2.98	0.00	0.04	0.00	0.00	0.00	1108	0.46	0.00	0.00	0.00	0.00	1.00
137	N2-RV4-RG20-Z0.1	11	1.62	0.00	0.75	0.00	0.00	0.00	8	0.00	0.00	0.00	0.00	0.00	1.00
138	N4-RV4-RG20-Z0.1	70	4.56	0.00	1.06	0.00	0.00	0.06	22	0.00	0.00	0.00	0.00	0.00	1.00
139	N8-RV4-RG20-Z0.1	325	2.03	0.00	0.06	1.25	0.00	0.00	107	0.00	0.00	0.00	0.00	0.00	3.00
140	N16-RV4-RG20-Z0.1	1030	3.44	0.00	0.00	1.00	0.00	0.00	346	0.00	0.00	0.00	0.00	0.00	0.00
141	N2-RV4-RG20-Z1.0	48	0.56	0.00	0.11	0.00	0.00	0.00	5	0.00	0.00	0.00	0.00	0.00	0.00
142	N4-RV4-RG20-Z1.0	128	0.62	0.00	0.00	0.00	0.00	0.00	19	0.00	0.00	0.00	0.00	0.00	0.00
143	N8-RV4-RG20-Z1.0	362	1.07	0.00	0.00	0.96	0.37	0.07	85	0.00	0.00	0.00	0.00	0.00	0.00
144	N16-RV4-RG20-Z1.0	854	4.05	0.00	0.00	0.00	0.00	0.00	259	0.00	0.00	0.00	0.00	0.00	1.00
145	N32-RV1-RG20-Z0.01	1415	5.30	0.00	0.12	4.00	0.00	0.00	4963	3.22	0.00	0.00	0.00	0.00	7.00
146	N32-RV2-RG20-Z0.01	2419	5.34	0.00	0.05	1.39	0.02	0.00	4223	2.00	0.00	1.00	0.00	0.00	2.00
147	N32-RV1-RG20-Z1.0	675	9.43	0.00	0.46	3.03	0.28	0.02	1409	8.84	0.00	2.01	0.00	0.12	2.46
148	N32-RV2-RG20-Z1.0	1328	4.55	0.00	0.03	2.53	0.35	0.00	1347	7.19	0.00	1.10	1.00	0.31	5.52

Note. Average number of BH and NS binaries of with various companion types for all simulations at late times (10–13 Gyr). We distinguish here between binaries that are found in accreting and detached configurations. Accreting binaries can be viewed as low-mass X-ray binary candidates. See Section 4 for further discussion.

Table 8
Total Number of Stellar Collisions per Model

	Simulation	MS–MS	MS–G	MS–WD	MS–NS	MS–BH	G–G	G–WD	G–NS	G–BH	WD–WD	WD–NS	WD–BH
1	N2-RV0.5-RG2-Z0.01	650	346	72	1	136	33	62	1	44	0	0	0
2	N4-RV0.5-RG2-Z0.01	1738	1309	299	35	625	134	267	24	48	4	0	1
3	N8-RV0.5-RG2-Z0.01	2133	796	1221	152	100	3	294	37	34	51	12	7
4	N16-RV0.5-RG2-Z0.01	…	…	…	…	…	…	…	…	…	…	…	…
5	N2-RV0.5-RG2-Z0.1	792	732	57	1	60	35	54	3	43	0	0	0
6	N4-RV0.5-RG2-Z0.1	1489	1207	553	28	87	28	253	14	39	19	4	0
7	N8-RV0.5-RG2-Z0.1	2628	3388	1138	93	131	35	350	18	81	27	7	1
8	N16-RV0.5-RG2-Z0.1	4170	12172	452	14	249	35	127	7	207	2	0	0
9	N2-RV0.5-RG2-Z1.0	919	773	57	1	35	100	27	0	34	0	0	0
10	N4-RV0.5-RG2-Z1.0	2263	1522	392	36	100	197	332	21	95	0	0	0
11	N8-RV0.5-RG2-Z1.0	4813	3270	1352	117	271	259	727	87	272	15	5	2
12	N16-RV0.5-RG2-Z1.0	10962	8680	2790	300	824	424	1480	150	735	27	4	3
13	N2-RV0.5-RG8-Z0.01	829	805	110	11	366	73	58	4	27	1	0	0
14	N4-RV0.5-RG8-Z0.01	1677	736	615	40	308	19	250	17	19	27	4	0
15	N8-RV0.5-RG8-Z0.01	2214	841	1186	125	133	7	245	38	37	66	17	0
16	N16-RV0.5-RG8-Z0.01	…	…	…	…	…	…	…	…	…	…	…	…
17	N2-RV0.5-RG8-Z0.1	806	553	227	9	52	22	109	4	18	7	1	0
18	N4-RV0.5-RG8-Z0.1	1628	1393	625	39	75	27	212	7	52	14	3	0
19	N8-RV0.5-RG8-Z0.1	2378	3555	720	59	107	13	164	7	62	22	2	0
20	N16-RV0.5-RG8-Z0.1	3895	12649	276	9	219	34	98	2	167	2	0	0
21	N2-RV0.5-RG8-Z1.0	992	706	143	5	56	68	141	5	40	3	0	0
22	N4-RV0.5-RG8-Z1.0	1976	1180	294	17	158	84	175	8	123	3	0	0
23	N8-RV0.5-RG8-Z1.0	4470	2803	921	73	384	185	469	29	316	8	3	4
24	N16-RV0.5-RG8-Z1.0	10128	7960	2394	167	931	315	1138	69	803	33	5	3
25	N2-RV0.5-RG20-Z0.01	740	286	229	11	166	15	98	3	15	8	1	1
26	N4-RV0.5-RG20-Z0.01	1602	613	400	23	261	13	98	3	33	13	2	8
27	N8-RV0.5-RG20-Z0.01	2043	801	998	130	147	7	210	26	33	42	3	1
28	N16-RV0.5-RG20-Z0.01	…	…	…	…	…	…	…	…	…	…	…	…
29	N2-RV0.5-RG20-Z0.1	1029	949	266	4	70	42	159	5	34	7	0	0
30	N4-RV0.5-RG20-Z0.1	1803	1518	505	27	116	22	168	10	38	12	0	1
31	N8-RV0.5-RG20-Z0.1	1953	2980	514	22	130	18	116	4	90	7	0	1
32	N16-RV0.5-RG20-Z0.1	3608	12602	256	7	249	36	78	3	192	1	0	0
33	N2-RV0.5-RG20-Z1.0	1002	609	163	2	47	78	131	5	34	2	0	0
34	N4-RV0.5-RG20-Z1.0	2161	1131	424	17	111	68	206	5	115	6	1	0
35	N8-RV0.5-RG20-Z1.0	4574	3144	1137	93	359	182	554	47	303	5	1	1
36	N16-RV0.5-RG20-Z1.0	10305	8024	2438	184	869	332	1122	98	789	19	4	1
37	N2-RV1-RG2-Z0.01	322	70	187	6	27	3	49	2	4	2	0	0
38	N4-RV1-RG2-Z0.01	533	82	442	21	34	1	82	3	3	33	3	0
39	N8-RV1-RG2-Z0.01	447	143	80	3	44	1	10	0	6	3	0	0
40	N16-RV1-RG2-Z0.01	916	405	72	3	81	1	3	1	21	1	0	0
41	N2-RV1-RG2-Z0.1	311	114	105	1	26	3	31	1	3	2	0	0
42	N4-RV1-RG2-Z0.1	659	197	399	17	25	1	82	1	8	13	0	0
43	N8-RV1-RG2-Z0.1	473	396	53	1	51	1	17	0	17	0	0	0
44	N16-RV1-RG2-Z0.1	1011	1557	47	1	91	7	16	0	34	1	0	0
45	N2-RV1-RG2-Z1.0	434	209	78	1	17	23	35	2	8	0	0	0
46	N4-RV1-RG2-Z1.0	1220	409	341	18	134	25	99	7	48	3	0	4
47	N8-RV1-RG2-Z1.0	2121	734	510	22	130	33	170	2	57	7	0	0
48	N16-RV1-RG2-Z1.0	3479	1539	497	5	295	31	157	2	146	2	0	1
49	N2-RV1-RG8-Z0.01	349	49	287	9	52	1	47	1	3	9	0	0
50	N4-RV1-RG8-Z0.01	467	99	331	15	51	0	39	2	3	24	2	2
51	N8-RV1-RG8-Z0.01	380	158	58	0	43	2	6	0	6	0	0	0
52	N16-RV1-RG8-Z0.01	997	410	73	0	91	2	10	0	21	1	0	1
53	N2-RV1-RG8-Z0.1	449	115	228	7	30	5	41	1	5	8	0	2
54	N4-RV1-RG8-Z0.1	264	140	42	0	26	0	7	0	8	0	0	0
55	N8-RV1-RG8-Z0.1	505	438	66	2	63	1	12	0	11	1	0	0

Table 8
(Continued)

	Simulation	MS–MS	MS–G	MS–WD	MS–NS	MS–BH	G–G	G–WD	G–NS	G–BH	WD–WD	WD–NS	WD–BH
56	N16-RV1-RG8-Z0.1	1279	1508	85	0	94	5	20	0	43	1	0	0
57	N2-RV1-RG8-Z1.0	574	224	160	2	52	9	54	0	14	3	0	1
58	N4-RV1-RG8-Z1.0	1243	378	313	12	62	18	79	5	29	6	0	0
59	N8-RV1-RG8-Z1.0	1854	610	325	6	114	22	104	2	60	3	0	1
60	N16-RV1-RG8-Z1.0	3403	1504	429	5	297	47	154	5	144	2	0	0
61	N2-RV1-RG20-Z0.01	341	51	289	9	42	0	37	1	1	9	0	0
62	N4-RV1-RG20-Z0.01	623	101	517	23	125	0	70	7	9	30	3	0
63	N8-RV1-RG20-Z0.01	399	128	29	2	53	0	2	0	7	0	0	0
64	N16-RV1-RG20-Z0.01	946	420	75	1	80	1	3	0	20	0	0	0
65	N2-RV1-RG20-Z0.1	548	165	182	1	77	9	53	0	16	3	0	0
66	N4-RV1-RG20-Z0.1	350	162	115	3	37	2	19	1	6	1	1	1
67	N8-RV1-RG20-Z0.1	525	385	57	0	46	3	9	0	14	0	0	0
68	N16-RV1-RG20-Z0.1	1280	1494	81	0	114	4	20	0	41	1	0	0
69	N2-RV1-RG20-Z1.0	581	191	160	1	24	19	50	0	19	1	0	0
70	N4-RV1-RG20-Z1.0	995	302	234	3	68	12	74	2	20	2	1	0
71	N8-RV1-RG20-Z1.0	1628	630	297	12	113	9	79	3	62	2	0	2
72	N16-RV1-RG20-Z1.0	3338	1435	432	11	260	31	102	5	133	2	0	0
73	N2-RV2-RG2-Z0.01	155	25	70	0	54	1	7	0	1	0	0	0
74	N4-RV2-RG2-Z0.01	171	25	98	2	19	0	16	1	1	8	0	0
75	N8-RV2-RG2-Z0.01	142	30	9	0	26	0	0	0	2	1	0	0
76	N16-RV2-RG2-Z0.01	405	83	22	0	38	0	3	0	1	1	0	0
77	N2-RV2-RG2-Z0.1	83	22	13	0	18	0	8	0	1	0	0	0
78	N4-RV2-RG2-Z0.1	142	32	44	3	49	1	6	0	2	1	0	0
79	N8-RV2-RG2-Z0.1	206	75	12	0	25	0	1	0	2	0	0	0
80	N16-RV2-RG2-Z0.1	512	259	33	0	40	1	3	0	8	2	0	0
81	N2-RV2-RG2-Z1.0	108	31	10	0	4	0	5	0	3	0	0	0
82	N4-RV2-RG2-Z1.0	254	58	42	0	11	4	7	0	7	1	0	0
83	N8-RV2-RG2-Z1.0	501	113	43	0	27	2	12	1	10	0	0	0
84	N16-RV2-RG2-Z1.0	1127	326	133	1	67	4	19	0	26	1	0	1
85	N2-RV2-RG8-Z0.01	52	3	9	0	19	0	1	0	0	0	0	0
86	N4-RV2-RG8-Z0.01	63	16	7	0	24	1	1	0	0	0	0	0
87	N8-RV2-RG8-Z0.01	156	27	15	0	19	1	3	0	5	0	0	0
88	N16-RV2-RG8-Z0.01	405	97	33	2	33	0	4	0	5	1	0	0
89	N2-RV2-RG8-Z0.1	197	45	121	0	18	0	26	0	1	4	0	0
90	N4-RV2-RG8-Z0.1	113	35	8	0	17	0	2	0	2	0	0	0
91	N8-RV2-RG8-Z0.1	225	87	13	0	26	0	5	0	1	0	0	0
92	N16-RV2-RG8-Z0.1	490	252	38	0	44	0	5	0	7	1	0	0
93	N2-RV2-RG8-Z1.0	83	26	7	1	3	2	2	0	1	0	0	0
94	N4-RV2-RG8-Z1.0	204	40	23	0	10	2	3	0	2	0	0	0
95	N8-RV2-RG8-Z1.0	480	114	53	1	25	2	7	0	12	0	0	0
96	N16-RV2-RG8-Z1.0	1173	339	91	0	64	6	35	1	18	1	0	0
97	N2-RV2-RG20-Z0.01	56	6	14	0	19	0	2	0	1	0	0	0
98	N4-RV2-RG20-Z0.01	68	16	7	0	24	0	0	0	1	0	0	0
99	N8-RV2-RG20-Z0.01	181	32	15	0	30	0	3	0	2	0	0	0
100	N16-RV2-RG20-Z0.01	451	82	39	0	37	1	4	0	3	0	0	0
101	N2-RV2-RG20-Z0.1	57	10	8	0	15	0	3	0	0	0	0	0
102	N4-RV2-RG20-Z0.1	77	22	9	0	13	0	1	0	1	0	0	0
103	N8-RV2-RG20-Z0.1	189	76	11	0	18	1	3	0	1	0	0	0
104	N16-RV2-RG20-Z0.1	532	251	35	1	37	1	4	0	8	1	0	0
105	N2-RV2-RG20-Z1.0	98	25	8	1	7	1	2	0	4	0	0	0
106	N4-RV2-RG20-Z1.0	192	41	19	0	11	3	4	0	4	0	0	0
107	N8-RV2-RG20-Z1.0	425	117	45	0	34	1	7	1	10	0	0	0
108	N16-RV2-RG20-Z1.0	1158	313	109	0	73	3	28	0	32	1	0	0
109	N2-RV4-RG2-Z0.01	3	0	0	0	11	0	0	0	0	0	0	0
110	N4-RV4-RG2-Z0.01	18	2	2	0	10	0	0	0	0	0	0	0

Table 8
(Continued)

	Simulation	MS–MS	MS–G	MS–WD	MS–NS	MS–BH	G–G	G–WD	G–NS	G–BH	WD–WD	WD–NS	WD–BH
111	N8-RV4-RG2-Z0.01	47	7	0	0	6	0	0	0	1	0	0	0
112	N16-RV4-RG2-Z0.01	179	27	14	0	11	0	1	0	0	0	0	0
113	N2-RV4-RG2-Z0.1	4	0	0	0	13	0	0	0	0	0	0	0
114	N4-RV4-RG2-Z0.1	17	4	0	0	13	0	0	0	0	0	0	0
115	N8-RV4-RG2-Z0.1	66	18	1	0	13	0	0	0	1	0	0	0
116	N16-RV4-RG2-Z0.1	205	51	12	0	19	0	1	0	1	1	0	0
117	N2-RV4-RG2-Z1.0	6	1	0	0	0	0	0	0	0	0	0	1
118	N4-RV4-RG2-Z1.0	41	3	3	0	2	0	0	0	1	0	0	0
119	N8-RV4-RG2-Z1.0	113	17	16	0	8	0	1	0	1	0	0	0
120	N16-RV4-RG2-Z1.0	330	69	33	0	14	1	2	0	5	0	0	0
121	N2-RV4-RG8-Z0.01	25	1	4	0	29	0	0	0	0	1	0	0
122	N4-RV4-RG8-Z0.01	29	8	1	0	15	0	0	0	0	0	0	0
123	N8-RV4-RG8-Z0.01	62	12	6	0	13	0	1	0	1	0	0	0
124	N16-RV4-RG8-Z0.01	172	22	16	0	16	0	1	0	0	0	0	0
125	N2-RV4-RG8-Z0.1	15	2	0	0	21	0	0	0	0	0	0	0
126	N4-RV4-RG8-Z0.1	32	8	5	0	12	0	0	0	0	0	0	0
127	N8-RV4-RG8-Z0.1	79	12	6	0	19	0	1	0	0	0	0	0
128	N16-RV4-RG8-Z0.1	256	43	22	0	24	0	2	0	2	1	0	0
129	N2-RV4-RG8-Z1.0	22	3	1	0	2	0	0	0	0	0	0	0
130	N4-RV4-RG8-Z1.0	37	8	6	0	0	0	1	0	1	0	0	0
131	N8-RV4-RG8-Z1.0	127	23	14	0	6	0	4	0	1	0	0	0
132	N16-RV4-RG8-Z1.0	340	67	31	0	6	0	2	1	3	0	0	0
133	N2-RV4-RG20-Z0.01	18	1	1	0	11	0	0	0	0	0	0	0
134	N4-RV4-RG20-Z0.01	34	3	3	0	8	0	0	0	0	0	0	0
135	N8-RV4-RG20-Z0.01	76	12	5	0	5	0	0	0	0	0	0	0
136	N16-RV4-RG20-Z0.01	197	20	24	0	13	0	2	0	1	3	0	0
137	N2-RV4-RG20-Z0.1	25	3	2	0	9	0	2	0	0	0	0	0
138	N4-RV4-RG20-Z0.1	40	10	4	0	21	0	0	0	0	0	0	0
139	N8-RV4-RG20-Z0.1	108	15	10	0	24	0	0	0	0	0	0	0
140	N16-RV4-RG20-Z0.1	216	48	24	0	20	0	1	0	2	0	0	1
141	N2-RV4-RG20-Z1.0	19	5	2	0	1	0	0	0	1	0	0	0
142	N4-RV4-RG20-Z1.0	50	5	7	0	3	0	1	0	0	0	0	0
143	N8-RV4-RG20-Z1.0	117	19	7	0	9	0	3	0	1	0	0	0
144	N16-RV4-RG20-Z1.0	344	59	20	0	13	2	7	0	3	1	0	0
145	N32-RV1-RG20-Z0.01	2167	1320	72	8	159	1	14	5	39	2	0	1
146	N32-RV2-RG20-Z0.01	1221	308	92	1	77	1	7	0	11	2	1	0
147	N32-RV1-RG20-Z1.0	6533	4406	400	5	593	49	176	1	388	3	0	2
148	N32-RV2-RG20-Z1.0	3244	928	310	0	188	13	67	0	73	4	0	1

Note. Total number of stellar collisions of various combinations of stellar types occurring in each model.

Table 9
White Dwarf Binaries, Pulsars, and Blue Stragglers

	Simulation	N_{WD}	Detached WD binaries			Accreting WD binaries			N_{pulsar}	N_{MSP}	N_{BS}
			MS	G	WD	MS	G	WD			
1	N2-RV0.5-RG2-Z0.01	…	…	…	…	…	…	…	0	0	…
2	N4-RV0.5-RG2-Z0.01	…	…	…	…	…	…	…	0	0	…
3	N8-RV0.5-RG2-Z0.01	57663	46.18	0.0	10.93	5.91	0.09	3.46	5.43	2.84	32.5
4	N16-RV0.5-RG2-Z0.01	…	…	…	…	…	…	…	0	0	…
5	N2-RV0.5-RG2-Z0.1	…	…	…	…	…	…	…	0	0	…
6	N4-RV0.5-RG2-Z0.1	…	…	…	…	…	…	…	0	0	…
7	N8-RV0.5-RG2-Z0.1	63257	79.83	0.0	11.0	14.48	0.31	9.96	6.96	3.75	79.0
8	N16-RV0.5-RG2-Z0.1	148248	184.31	0.0	19.0	15.85	1.94	15.48	9.14	0.36	114.0
9	N2-RV0.5-RG2-Z1.0	…	…	…	…	…	…	…	0	0	…
10	N4-RV0.5-RG2-Z1.0	…	…	…	…	…	…	…	0	0	…
11	N8-RV0.5-RG2-Z1.0	51888	52.03	0.0	2.71	9.3	0.4	4.8	8.58	3.15	85.0
12	N16-RV0.5-RG2-Z1.0	120186	166.38	0.0	11.65	30.83	1.22	10.06	18.52	8.65	209.0
13	N2-RV0.5-RG8-Z0.01	…	…	…	…	…	…	…	0	0	…
14	N4-RV0.5-RG8-Z0.01	16173	5.61	0.0	2.73	2.3	0.01	0.07	0.32	0.32	5.0
15	N8-RV0.5-RG8-Z0.01	73487	63.99	0.0	14.88	13.16	0.42	3.27	7.21	3.07	44.0
16	N16-RV0.5-RG8-Z0.01	…	…	…	…	…	…	…	0	0	…
17	N2-RV0.5-RG8-Z0.1	10794	7.42	0.0	2.63	1.76	0.06	2.42	0.03	0.03	5.0
18	N4-RV0.5-RG8-Z0.1	32209	37.13	0.0	6.72	5.4	0.27	2.62	1.72	1.48	17.0
19	N8-RV0.5-RG8-Z0.1	76598	128.48	0.0	18.75	17.33	1.46	9.84	4.6	2.05	94.0
20	N16-RV0.5-RG8-Z0.1	161457	169.33	0.0	16.51	24.07	0.84	16.89	6.12	0.12	84.5
21	N2-RV0.5-RG8-Z1.0	4527	0.51	0.0	0.69	0.0	0.27	0.42	0.07	0.03	…
22	N4-RV0.5-RG8-Z1.0	11703	23.28	0.0	3.63	2.8	0.45	0.94	1.56	1.06	25.0
23	N8-RV0.5-RG8-Z1.0	61276	86.5	0.0	10.04	12.55	1.12	6.42	4.86	1.94	147.0
24	N16-RV0.5-RG8-Z1.0	130637	190.14	0.0	15.54	38.2	2.39	10.49	12.71	5.29	260.0
25	N2-RV0.5-RG20-Z0.01	10616	12.24	0.0	3.1	0.58	0.0	0.14	0.19	0.19	2.0
26	N4-RV0.5-RG20-Z0.01	23665	39.64	0.0	10.03	3.95	0.16	2.56	1.13	0.13	7.0
27	N8-RV0.5-RG20-Z0.01	78359	90.06	0.0	22.85	10.7	0.37	6.87	4.79	3.75	48.0
28	N16-RV0.5-RG20-Z0.01	…	…	…	…	…	…	…	0	0	…
29	N2-RV0.5-RG20-Z0.1	10423	11.0	0.0	1.61	3.46	0.24	1.45	1.0	0.0	3.0
30	N4-RV0.5-RG20-Z0.1	33903	41.04	0.0	8.81	5.32	0.32	2.92	1.18	0.18	21.5
31	N8-RV0.5-RG20-Z0.1	81000	121.12	0.0	22.01	15.16	1.21	11.44	2.68	0.84	91.0
32	N16-RV0.5-RG20-Z0.1	164280	148.79	0.0	13.71	13.29	1.91	13.41	13.78	0.11	95.0
33	N2-RV0.5-RG20-Z1.0	13131	16.55	0.0	2.25	2.6	0.2	0.76	0.04	0.0	13.0
34	N4-RV0.5-RG20-Z1.0	30391	31.43	0.0	4.53	5.54	0.75	1.08	3.19	0.24	44.0
35	N8-RV0.5-RG20-Z1.0	63808	73.08	0.0	6.7	13.82	0.5	4.3	4.65	2.5	123.5
36	N16-RV0.5-RG20-Z1.0	133475	192.47	0.0	16.08	42.53	2.19	12.97	14.32	5.82	249.0
37	N2-RV1.0-RG2-Z0.01	…	…	…	…	…	…	…	0	0	…
38	N4-RV1.0-RG2-Z0.01	18543	47.72	0.0	6.75	6.51	0.46	7.24	0.43	0.43	13.0
39	N8-RV1.0-RG2-Z0.01	70798	190.44	0.0	15.22	9.0	1.44	7.17	0.0	0.0	9.0
40	N16-RV1.0-RG2-Z0.01	145298	192.38	0.0	12.46	25.54	1.42	16.21	1.0	0.0	6.0
41	N2-RV1.0-RG2-Z0.1	…	…	…	…	…	…	…	0	0	…
42	N4-RV1.0-RG2-Z0.1	22760	81.73	0.0	12.71	18.77	1.45	8.32	1.33	0.76	29.0
43	N8-RV1.0-RG2-Z0.1	71147	160.6	0.0	11.0	20.1	1.77	7.07	1.0	0.0	15.0
44	N16-RV1.0-RG2-Z0.1	148283	181.23	0.0	11.02	21.16	2.03	13.75	3.0	0.0	13.0
45	N2-RV1.0-RG2-Z1.0	…	…	…	…	…	…	…	0	0	…
46	N4-RV1.0-RG2-Z1.0	13329	46.14	0.0	7.32	7.74	1.82	3.77	0.89	0.39	47.0
47	N8-RV1.0-RG2-Z1.0	61791	210.21	0.0	15.23	20.09	4.02	7.86	1.67	0.75	123.0
48	N16-RV1.0-RG2-Z1.0	132203	312.87	0.0	14.39	21.59	4.65	3.65	2.0	0.07	190.0
49	N2-RV1.0-RG8-Z0.01	13358	40.48	0.0	5.85	8.56	0.38	2.73	0.0	0.0	2.0
50	N4-RV1.0-RG8-Z0.01	37707	145.22	0.0	33.71	17.75	0.29	13.43	2.57	0.48	21.0
51	N8-RV1.0-RG8-Z0.01	80919	178.94	0.0	19.97	14.1	1.52	5.16	1.0	0.0	8.0
52	N16-RV1.0-RG8-Z0.01	164070	244.66	0.0	12.09	22.26	1.53	12.55	4.0	0.0	10.0
53	N2-RV1.0-RG8-Z0.1	15811	54.66	0.0	5.47	11.16	0.52	4.64	0.08	0.08	11.0
54	N4-RV1.0-RG8-Z0.1	39139	151.57	0.0	14.86	20.95	1.67	2.38	0.0	0.0	16.0
55	N8-RV1.0-RG8-Z0.1	80248	154.92	0.0	12.77	24.88	1.69	7.23	0.0	0.0	12.0

Table 9
(Continued)

	Simulation	$N_{\rm WD}$	Detached WD binaries			Accreting WD binaries			$N_{\rm pulsar}$	$N_{\rm MSP}$	$N_{\rm BS}$
			MS	G	WD	MS	G	WD			
56	N16-RV1.0-RG8-Z0.1	163291	200.73	0.0	7.62	21.76	1.99	13.34	3.68	0.68	17.5
57	N2-RV1.0-RG8-Z1.0	14007	42.59	0.0	3.05	12.78	1.24	2.07	0.08	0.0	27.0
58	N4-RV1.0-RG8-Z1.0	31845	104.66	0.0	14.87	18.92	2.42	8.18	2.6	0.4	68.0
59	N8-RV1.0-RG8-Z1.0	67464	188.59	0.0	21.41	13.47	4.47	5.91	1.3	0.3	117.0
60	N16-RV1.0-RG8-Z1.0	138310	329.49	0.0	29.1	26.34	6.27	4.37	3.14	1.0	167.5
61	N2-RV1.0-RG20-Z0.01	17318	56.29	0.0	8.06	10.83	0.25	3.44	0.06	0.06	4.0
62	N4-RV1.0-RG20-Z0.01	35981	85.8	0.0	15.12	11.67	0.29	9.06	2.0	0.36	16.0
63	N8-RV1.0-RG20-Z0.01	83749	179.92	0.0	13.62	11.96	1.38	9.96	0.0	0.0	9.0
64	N16-RV1.0-RG20-Z0.01	168061	203.54	0.0	15.06	22.57	1.38	16.6	1.0	0.0	9.5
65	N2-RV1.0-RG20-Z0.1	15722	49.16	0.0	4.88	14.08	0.42	0.34	0.0	0.0	15.5
66	N4-RV1.0-RG20-Z0.1	40727	166.48	0.0	25.8	24.44	1.76	4.0	1.0	0.0	14.5
67	N8-RV1.0-RG20-Z0.1	82254	153.36	0.0	11.85	24.39	2.33	5.94	0.0	0.0	9.0
68	N16-RV1.0-RG20-Z0.1	166807	180.64	0.0	9.39	29.79	2.51	16.18	4.58	0.0	16.0
69	N2-RV1.0-RG20-Z1.0	15350	50.57	0.0	10.74	11.26	1.0	2.37	1.0	1.0	19.0
70	N4-RV1.0-RG20-Z1.0	33409	115.42	0.0	13.38	21.72	2.15	5.28	1.0	0.0	73.5
71	N8-RV1.0-RG20-Z1.0	69076	216.0	0.0	16.78	16.85	5.11	6.26	1.75	0.25	76.0
72	N16-RV1.0-RG20-Z1.0	138669	314.62	0.0	32.67	26.6	7.08	3.58	4.69	0.08	157.0
73	N2-RV2.0-RG2-Z0.01	…	…	…	…	…	…	…	0	0	…
74	N4-RV2.0-RG2-Z0.01	18826	223.84	0.0	20.34	25.21	2.5	14.39	1.1	0.9	6.0
75	N8-RV2.0-RG2-Z0.01	65541	335.35	0.0	11.42	59.77	3.0	25.77	0.0	0.0	2.0
76	N16-RV2.0-RG2-Z0.01	143794	442.79	0.0	15.06	74.14	4.38	29.35	0.0	0.0	2.5
77	N2-RV2.0-RG2-Z0.1	…	…	…	…	…	…	…	0	0	…
78	N4-RV2.0-RG2-Z0.1	21057	233.74	0.0	16.79	55.68	3.53	7.63	1.0	0.4	5.5
79	N8-RV2.0-RG2-Z0.1	65712	262.43	0.0	11.3	91.23	4.27	5.63	0.5	0.5	3.0
80	N16-RV2.0-RG2-Z0.1	148466	369.89	0.0	15.3	106.28	4.69	11.16	1.0	0.0	6.0
81	N2-RV2.0-RG2-Z1.0	…	…	…	…	…	…	…	0	0	…
82	N4-RV2.0-RG2-Z1.0	24788	185.0	0.0	12.12	45.71	6.29	6.06	1.0	0.0	16.0
83	N8-RV2.0-RG2-Z1.0	63765	216.23	0.0	9.42	55.12	6.15	3.31	2.25	0.0	19.0
84	N16-RV2.0-RG2-Z1.0	136364	342.14	0.0	16.64	62.11	8.1	4.04	1.0	0.0	43.0
85	N2-RV2.0-RG8-Z0.01	18765	264.2	0.0	25.4	29.5	3.4	16.5	0.0	0.0	1.0
86	N4-RV2.0-RG8-Z0.01	39727	348.73	0.0	15.45	50.82	2.45	30.0	0.0	0.0	1.5
87	N8-RV2.0-RG8-Z0.01	81253	375.31	0.0	15.5	65.0	3.62	34.09	1.0	0.0	1.0
88	N16-RV2.0-RG8-Z0.01	165866	508.17	0.0	21.69	86.33	5.63	23.74	0.41	0.0	2.0
89	N2-RV2.0-RG8-Z0.1	17882	201.59	0.0	21.47	32.71	3.06	5.76	0.25	0.25	21.0
90	N4-RV2.0-RG8-Z0.1	39141	279.75	0.0	15.0	71.92	3.08	14.5	0.0	0.0	1.0
91	N8-RV2.0-RG8-Z0.1	81184	293.74	0.0	16.74	104.48	5.06	2.52	1.0	0.0	4.0
92	N16-RV2.0-RG8-Z0.1	164513	376.81	0.0	15.52	116.74	5.1	9.23	3.0	0.0	3.0
93	N2-RV2.0-RG8-Z1.0	16377	159.25	0.0	9.0	36.92	3.5	4.0	0.0	0.0	6.0
94	N4-RV2.0-RG8-Z1.0	34130	197.33	0.0	10.11	41.61	5.89	3.72	0.0	0.0	9.0
95	N8-RV2.0-RG8-Z1.0	69050	243.9	0.0	11.34	57.86	5.34	5.69	2.0	0.0	21.5
96	N16-RV2.0-RG8-Z1.0	140116	310.58	0.0	16.68	69.3	7.66	1.34	2.04	0.04	46.0
97	N2-RV2.0-RG20-Z0.01	19746	269.11	0.0	25.89	32.58	2.26	18.26	0.0	0.0	1.0
98	N4-RV2.0-RG20-Z0.01	41624	352.82	0.0	20.82	58.09	3.0	30.36	0.0	0.0	2.0
99	N8-RV2.0-RG20-Z0.01	84228	387.16	0.0	19.94	65.97	3.16	30.71	0.0	0.0	1.0
100	N16-RV2.0-RG20-Z0.01	171316	530.48	0.0	30.88	89.05	5.33	20.04	0.3	0.0	4.0
101	N2-RV2.0-RG20-Z0.1	19784	226.29	0.0	16.14	38.21	3.71	2.79	0.0	0.0	3.0
102	N4-RV2.0-RG20-Z0.1	40876	271.27	0.0	12.45	75.73	3.73	10.27	1.0	0.0	4.0
103	N8-RV2.0-RG20-Z0.1	82728	289.12	0.0	11.85	97.03	4.55	6.85	1.0	0.0	3.0
104	N16-RV2.0-RG20-Z0.1	168828	403.94	0.0	17.54	117.26	4.98	9.16	2.0	0.0	3.0
105	N2-RV2.0-RG20-Z1.0	16910	170.8	0.0	11.2	28.8	4.4	2.2	1.0	0.0	8.0
106	N4-RV2.0-RG20-Z1.0	34398	206.27	0.0	11.27	36.8	5.47	4.73	0.0	0.0	11.5
107	N8-RV2.0-RG20-Z1.0	69737	230.81	0.0	15.5	53.5	4.73	6.12	3.0	0.0	22.0
108	N16-RV2.0-RG20-Z1.0	140622	342.04	0.0	21.67	63.06	6.75	2.46	1.0	0.0	45.0
109	N2-RV4.0-RG2-Z0.01	…	…	…	…	…	…	…	0	0	…

Table 9
(Continued)

	Simulation	$N_{\rm WD}$	Detached WD binaries			Accreting WD binaries			$N_{\rm pulsar}$	$N_{\rm MSP}$	$N_{\rm BS}$
			MS	G	WD	MS	G	WD			
110	N4-RV4.0-RG2-Z0.01	…	…	…	…	…	…	…	0	0	…
111	N8-RV4.0-RG2-Z0.01	…	…	…	…	…	…	…	0	0	…
112	N16-RV4.0-RG2-Z0.01	116606	1395.49	0.0	53.36	189.75	14.61	93.39	0.0	0.0	1.0
113	N2-RV4.0-RG2-Z0.1	…	…	…	…	…	…	…	0	0	…
114	N4-RV4.0-RG2-Z0.1	…	…	…	…	…	…	…	0	0	…
115	N8-RV4.0-RG2-Z0.1	…	…	…	…	…	…	…	0	0	…
116	N16-RV4.0-RG2-Z0.1	129372	1182.39	0.0	28.29	378.25	22.66	22.96	4.0	0.0	1.0
117	N2-RV4.0-RG2-Z1.0	…	…	…	…	…	…	…	0	0	…
118	N4-RV4.0-RG2-Z1.0	…	…	…	…	…	…	…	0	0	…
119	N8-RV4.0-RG2-Z1.0	51720	561.26	0.0	10.76	144.21	23.06	4.71	0.0	0.0	6.0
120	N16-RV4.0-RG2-Z1.0	131710	858.75	0.0	14.38	354.87	33.67	5.92	0.0	0.0	12.0
121	N2-RV4.0-RG8-Z0.01	16810	366.8	0.0	52.9	28.2	2.9	35.6	0.0	0.0	0.0
122	N4-RV4.0-RG8-Z0.01	38877	751.67	0.0	59.93	64.6	4.6	70.93	0.0	0.0	1.0
123	N8-RV4.0-RG8-Z0.01	81793	1150.97	0.0	48.77	128.17	8.87	120.9	0.22	0.0	1.0
124	N16-RV4.0-RG8-Z0.01	168173	1922.64	0.0	64.44	266.38	19.26	132.94	0.0	0.0	2.0
125	N2-RV4.0-RG8-Z0.1	17553	359.0	0.0	27.43	36.57	6.71	19.14	0.0	0.0	1.0
126	N4-RV4.0-RG8-Z0.1	38717	626.35	0.0	29.53	94.71	8.76	26.71	0.0	0.0	1.0
127	N8-RV4.0-RG8-Z0.1	80463	936.28	0.0	23.81	187.53	16.12	33.09	2.0	0.0	1.0
128	N16-RV4.0-RG8-Z0.1	165792	1441.44	0.0	26.34	453.15	26.0	30.72	9.0	0.0	4.0
129	N2-RV4.0-RG8-Z1.0	16483	299.83	0.0	18.17	29.67	7.0	8.83	0.0	0.0	0.0
130	N4-RV4.0-RG8-Z1.0	34167	473.76	0.0	14.76	65.29	16.06	11.65	1.0	0.0	1.0
131	N8-RV4.0-RG8-Z1.0	69738	643.25	0.0	8.16	168.69	24.59	6.75	0.0	0.0	5.0
132	N16-RV4.0-RG8-Z1.0	141667	911.91	0.0	13.57	363.57	35.86	4.77	2.0	0.0	12.0
133	N2-RV4.0-RG20-Z0.01	20126	430.1	0.0	67.0	35.3	3.0	32.3	0.0	0.0	0.0
134	N4-RV4.0-RG20-Z0.01	41320	794.12	0.0	60.0	70.5	4.69	79.12	0.0	0.0	1.0
135	N8-RV4.0-RG20-Z0.01	84710	1204.11	0.0	52.23	139.89	9.34	109.63	0.0	0.0	3.0
136	N16-RV4.0-RG20-Z0.01	172415	1964.04	0.0	59.94	273.2	18.89	129.81	1.0	0.0	1.0
137	N2-RV4.0-RG20-Z0.1	19752	379.5	0.0	28.25	32.88	5.88	23.25	1.0	0.0	2.0
138	N4-RV4.0-RG20-Z0.1	40217	654.94	0.0	24.56	98.06	8.5	27.56	2.0	0.0	1.0
139	N8-RV4.0-RG20-Z0.1	83099	970.75	0.0	21.25	194.41	16.81	32.75	5.0	0.0	1.0
140	N16-RV4.0-RG20-Z0.1	169786	1453.8	0.0	29.11	456.71	26.84	32.22	4.0	0.0	5.0
141	N2-RV4.0-RG20-Z1.0	17281	310.67	0.0	19.56	30.44	7.11	11.67	0.0	0.0	1.0
142	N4-RV4.0-RG20-Z1.0	34873	491.23	0.0	17.77	67.38	14.85	9.54	1.0	0.0	2.5
143	N8-RV4.0-RG20-Z1.0	70074	643.85	0.0	8.07	175.52	23.56	6.78	0.0	0.0	4.0
144	N16-RV4.0-RG20-Z1.0	142238	901.92	0.0	16.58	373.03	35.34	4.77	1.0	0.0	11.0
145	N32-RV1-RG20-Z0.01	295147	280.76	0.0	15.21	26.42	1.10	21.57	7.16	0.16	24
146	N32-RV2-RG20-Z0.01	286904	608.27	0.0	21.90	110.24	5.48	30.04	3.0	0.0	6
147	N32-RV1-RG20-Z1.0	278499	597.68	0.0	25.65	42.18	10.97	4.34	2.68	0.47	125
148	N32-RV2-RG20-Z1.0	282382	614.28	0.0	20.99	74.81	10.21	9.20	5.52	0.07	112

Note. Average number of WD binaries (see Section 6), pulsars (see Section 5), and BSs (see Section 8) for all late-time snapshots for each model.

Table 10
Binary BH Mergers

	Simulation	N_{BH} at 14 Gyr	In-cluster			Ejected	All Mergers
			Single–Single	Fewbody	Two-body		
1	N2-RV0.5-RG2-Z0.01	⋯	4	0	5	12	21
2	N4-RV0.5-RG2-Z0.01	⋯	9	1	16	42	68
3	N8-RV0.5-RG2-Z0.01	0	26	3	45	0	74
4	N16-RV0.5-RG2-Z0.01	⋯	⋯	⋯	⋯	⋯	⋯
5	N2-RV0.5-RG2-Z0.1	⋯	7	0	2	9	18
6	N4-RV0.5-RG2-Z0.1	⋯	5	0	11	28	44
7	N8-RV0.5-RG2-Z0.1	0	16	2	44	72	134
8	N16-RV0.5-RG2-Z0.1	53	46	13	151	163	373
9	N2-RV0.5-RG2-Z1.0	⋯	3	0	3	8	14
10	N4-RV0.5-RG2-Z1.0	⋯	3	1	9	17	30
11	N8-RV0.5-RG2-Z1.0	0	18	0	48	55	121
12	N16-RV0.5-RG2-Z1.0	1	28	13	183	140	364
13	N2-RV0.5-RG8-Z0.01	⋯	5	0	4	14	23
14	N4-RV0.5-RG8-Z0.01	0	14	0	20	39	73
15	N8-RV0.5-RG8-Z0.01	0	25	0	49	80	154
16	N16-RV0.5-RG8-Z0.01	⋯	⋯	⋯	⋯	⋯	⋯
17	N2-RV0.5-RG8-Z0.1	0	5	0	3	8	16
18	N4-RV0.5-RG8-Z0.1	0	7	2	15	38	62
19	N8-RV0.5-RG8-Z0.1	1	17	1	42	82	142
20	N16-RV0.5-RG8-Z0.1	69	49	11	134	178	372
21	N2-RV0.5-RG8-Z1.0	0	0	0	3	10	13
22	N4-RV0.5-RG8-Z1.0	0	2	0	6	26	34
23	N8-RV0.5-RG8-Z1.0	1	7	2	61	57	127
24	N16-RV0.5-RG8-Z1.0	6	39	19	201	136	395
25	N2-RV0.5-RG20-Z0.01	0	2	0	9	13	24
26	N4-RV0.5-RG20-Z0.01	1	9	0	13	37	59
27	N8-RV0.5-RG20-Z0.01	1	19	2	47	84	152
28	N16-RV0.5-RG20-Z0.01	⋯	⋯	⋯	⋯	⋯	⋯
29	N2-RV0.5-RG20-Z0.1	0	6	0	5	10	21
30	N4-RV0.5-RG20-Z0.1	0	7	0	23	25	55
31	N8-RV0.5-RG20-Z0.1	7	18	4	52	77	151
32	N16-RV0.5-RG20-Z0.1	92	58	13	156	167	394
33	N2-RV0.5-RG20-Z1.0	0	1	0	2	6	9
34	N4-RV0.5-RG20-Z1.0	0	8	0	18	14	40
35	N8-RV0.5-RG20-Z1.0	4	9	0	52	60	121
36	N16-RV0.5-RG20-Z1.0	5	40	13	198	126	377
37	N2-RV1-RG2-Z0.01	⋯	6	0	6	3	15
38	N4-RV1-RG2-Z0.01	0	5	0	9	18	32
39	N8-RV1-RG2-Z0.01	11	19	3	32	57	111
40	N16-RV1-RG2-Z0.01	199	51	14	104	134	303
41	N2-RV1-RG2-Z0.1	⋯	3	0	1	5	9
42	N4-RV1-RG2-Z0.1	0	5	1	11	18	35
43	N8-RV1-RG2-Z0.1	28	20	3	34	42	99
44	N16-RV1-RG2-Z0.1	0	21	8	92	130	251
45	N2-RV1-RG2-Z1.0	⋯	4	0	5	5	14
46	N4-RV1-RG2-Z1.0	1	4	0	8	9	21
47	N8-RV1-RG2-Z1.0	10	7	0	39	54	100
48	N16-RV1-RG2-Z1.0	131	15	9	123	120	267
49	N2-RV1-RG8-Z0.01	0	1	0	3	3	7
50	N4-RV1-RG8-Z0.01	1	8	1	10	29	48
51	N8-RV1-RG8-Z0.01	34	15	0	31	61	107
52	N16-RV1-RG8-Z0.01	240	41	16	100	143	300
53	N2-RV1-RG8-Z0.1	0	6	0	2	9	17
54	N4-RV1-RG8-Z0.1	1	8	0	7	21	36
55	N8-RV1-RG8-Z0.1	31	12	3	41	58	114

Table 10
(Continued)

	Simulation	N_{BH} at 14 Gyr	In-cluster			Ejected	All Mergers
			Single–Single	Fewbody	Two-body		
56	N16-RV1-RG8-Z0.1	227	39	7	121	140	307
57	N2-RV1-RG8-Z1.0	0	1	0	3	7	11
58	N4-RV1-RG8-Z1.0	0	7	1	12	18	38
59	N8-RV1-RG8-Z1.0	19	7	3	47	41	98
60	N16-RV1-RG8-Z1.0	143	26	7	122	116	271
61	N2-RV1-RG20-Z0.01	0	2	0	4	5	11
62	N4-RV1-RG20-Z0.01	0	1	0	6	31	38
63	N8-RV1-RG20-Z0.01	35	21	1	38	55	115
64	N16-RV1-RG20-Z0.01	250	39	11	106	145	301
65	N2-RV1-RG20-Z0.1	1	4	2	3	9	18
66	N4-RV1-RG20-Z0.1	3	5	1	12	24	42
67	N8-RV1-RG20-Z0.1	43	18	3	34	50	105
68	N16-RV1-RG20-Z0.1	257	32	12	100	139	283
69	N2-RV1-RG20-Z1.0	1	2	0	6	3	11
70	N4-RV1-RG20-Z1.0	3	2	0	9	12	23
71	N8-RV1-RG20-Z1.0	23	9	1	44	50	104
72	N16-RV1-RG20-Z1.0	154	19	8	129	116	272
73	N2-RV2-RG2-Z0.01	⋯	1	0	3	6	10
74	N4-RV2-RG2-Z0.01	2	7	0	6	17	30
75	N8-RV2-RG2-Z0.01	73	7	1	23	31	62
76	N16-RV2-RG2-Z0.01	489	24	7	65	103	199
77	N2-RV2-RG2-Z0.1	⋯	1	0	0	5	6
78	N4-RV2-RG2-Z0.1	1	3	0	5	13	21
79	N8-RV2-RG2-Z0.1	95	7	2	21	29	59
80	N16-RV2-RG2-Z0.1	497	20	2	49	84	155
81	N2-RV2-RG2-Z1.0	⋯	0	0	2	2	4
82	N4-RV2-RG2-Z1.0	16	1	0	3	9	13
83	N8-RV2-RG2-Z1.0	116	2	2	19	34	57
84	N16-RV2-RG2-Z1.0	433	12	6	50	63	131
85	N2-RV2-RG8-Z0.01	0	1	0	4	5	10
86	N4-RV2-RG8-Z0.01	13	4	1	8	15	28
87	N8-RV2-RG8-Z0.01	112	15	3	24	29	71
88	N16-RV2-RG8-Z0.01	610	20	6	60	94	180
89	N2-RV2-RG8-Z0.1	0	0	0	2	4	6
90	N4-RV2-RG8-Z0.1	16	4	1	8	12	25
91	N8-RV2-RG8-Z0.1	116	11	0	21	32	64
92	N16-RV2-RG8-Z0.1	541	19	5	53	81	158
93	N2-RV2-RG8-Z1.0	9	0	1	4	2	7
94	N4-RV2-RG8-Z1.0	52	1	0	6	9	16
95	N8-RV2-RG8-Z1.0	152	8	2	18	27	55
96	N16-RV2-RG8-Z1.0	441	13	3	38	74	128
97	N2-RV2-RG20-Z0.01	3	2	0	1	4	7
98	N4-RV2-RG20-Z0.01	14	4	0	5	14	23
99	N8-RV2-RG20-Z0.01	117	8	1	23	36	68
100	N16-RV2-RG20-Z0.01	581	24	4	56	86	170
101	N2-RV2-RG20-Z0.1	3	1	0	1	3	5
102	N4-RV2-RG20-Z0.1	15	2	0	6	14	22
103	N8-RV2-RG20-Z0.1	142	7	2	18	29	56
104	N16-RV2-RG20-Z0.1	589	21	2	45	87	155
105	N2-RV2-RG20-Z1.0	7	0	0	2	1	3
106	N4-RV2-RG20-Z1.0	38	4	0	5	8	17
107	N8-RV2-RG20-Z1.0	151	5	1	16	22	44
108	N16-RV2-RG20-Z1.0	481	14	2	63	74	153
109	N2-RV4-RG2-Z0.01	⋯	0	0	3	3	6

Table 10
(Continued)

	Simulation	N_{BH} at 14 Gyr	In-cluster			Ejected	All Mergers
			Single–Single	Fewbody	Two-body		
110	N4-RV4-RG2-Z0.01	⋯	2	0	0	10	12
111	N8-RV4-RG2-Z0.01	⋯	1	0	6	17	24
112	N16-RV4-RG2-Z0.01	892	12	3	31	−1	45
113	N2-RV4-RG2-Z0.1	⋯	0	0	1	4	5
114	N4-RV4-RG2-Z0.1	⋯	2	0	5	9	16
115	N8-RV4-RG2-Z0.1	⋯	5	0	5	24	34
116	N16-RV4-RG2-Z0.1	907	12	3	25	54	94
117	N2-RV4-RG2-Z1.0	⋯	0	0	0	2	2
118	N4-RV4-RG2-Z1.0	⋯	1	0	2	5	8
119	N8-RV4-RG2-Z1.0	300	3	0	6	17	26
120	N16-RV4-RG2-Z1.0	816	7	0	12	25	44
121	N2-RV4-RG8-Z0.01	6	0	0	3	3	6
122	N4-RV4-RG8-Z0.01	53	3	0	1	9	13
123	N8-RV4-RG8-Z0.01	330	11	0	9	20	40
124	N16-RV4-RG8-Z0.01	1090	8	2	28	44	82
125	N2-RV4-RG8-Z0.1	9	0	0	4	4	8
126	N4-RV4-RG8-Z0.1	68	1	0	1	11	13
127	N8-RV4-RG8-Z0.1	311	7	0	10	28	45
128	N16-RV4-RG8-Z0.1	989	9	5	37	49	100
129	N2-RV4-RG8-Z1.0	33	0	0	1	1	2
130	N4-RV4-RG8-Z1.0	133	2	1	2	5	10
131	N8-RV4-RG8-Z1.0	340	1	0	7	15	23
132	N16-RV4-RG8-Z1.0	834	7	0	25	27	59
133	N2-RV4-RG20-Z0.01	12	1	0	1	4	6
134	N4-RV4-RG20-Z0.01	68	2	0	2	10	14
135	N8-RV4-RG20-Z0.01	376	3	0	5	21	29
136	N16-RV4-RG20-Z0.01	1107	13	1	33	45	92
137	N2-RV4-RG20-Z0.1	11	1	0	2	5	8
138	N4-RV4-RG20-Z0.1	66	4	0	3	8	15
139	N8-RV4-RG20-Z0.1	327	2	1	15	21	39
140	N16-RV4-RG20-Z0.1	1026	11	3	31	52	97
141	N2-RV4-RG20-Z1.0	49	1	0	0	2	3
142	N4-RV4-RG20-Z1.0	125	3	0	1	6	10
143	N8-RV4-RG20-Z1.0	358	4	1	5	18	28
144	N16-RV4-RG20-Z1.0	856	6	1	15	28	50
145	N32-RV1-RG20-Z0.01	852	73	37	250	179	539
146	N32-RV2-RG20-Z0.01	1714	44	13	152	159	368
147	N32-RV1-RG20-Z1.0	518	43	34	315	153	545
148	N32-RV2-RG20-Z1.0	1165	40	12	182	142	376

Note. Column (3) shows the total number of BHs retained at the end of each simulation (models marked with a "…" disrupted before 14 Gyr). Columns (4)–(7) show the total number of BBH mergers occurring through single–single capture, fewbody mergers, two-body mergers, and ejected mergers, respectively. See Section 9.1 for descriptions of these various channels. Column (8) shows the total number of BBH mergers per model.

ORCID iDs

Kyle Kremer https://orcid.org/0000-0002-4086-3180
Claire S. Ye https://orcid.org/0000-0001-9582-881X
Nicholas Z. Rui https://orcid.org/0000-0002-1884-3992
Newlin C. Weatherford https://orcid.org/0000-0002-9660-9085
Sourav Chatterjee https://orcid.org/0000-0002-3680-2684
Giacomo Fragione https://orcid.org/0000-0002-7330-027X
Carl L. Rodriguez https://orcid.org/0000-0003-4175-8881
Mario Spera https://orcid.org/0000-0003-0930-6930
Frederic A. Rasio https://orcid.org/0000-0002-7132-418X

References

Aarseth, S. J. 2003, Gravitational N-Body Simulations (Cambridge: Cambridge Univ. Press)
Aarseth, S. J., & Heggie, D. C. 1976, A&A, 53, 259
Alessandrini, E., Lanzoni, B., Ferraro, F. R., Miocchi, P., & Vesperini, E. 2016, ApJ, 833, 252
Amaro-Seoane, P., Audley, H., Babak, S., et al. 2017, arXiv:1702.00786
Antognini, J. M. O., & Thompson, T. A. 2016, MNRAS, 456, 4219
Antonini, F., & Gieles, M. 2020, MNRAS, 492, 2936
Antonini, F., & Rasio, F. A. 2016, ApJ, 831, 187
Antonini, F., Toonen, S., & Hamers, A. S. 2017, ApJ, 841, 77
Arca Sedda, M., Askar, A., & Giersz, M. 2018, MNRAS, 479, 4652
Askar, A., Arca Sedda, M., & Giersz, M. 2018, MNRAS, 478, 1844

Askar, A., Szkudlarek, M., Gondek-Rosińska, D., Giersz, M., & Bulik, T. 2017, MNRAS, 464, L36
Bacon, D., Sigurdsson, S., & Davies, M. B. 1996, MNRAS, 281, 830
Bae, Y.-B., Kim, C., & Lee, H. M. 2014, MNRAS, 440, 2714
Bahramian, A., Heinke, C. O., Sivakoff, G. R., & Gladstone, J. C. 2013, ApJ, 766, 136
Bahramian, A., Heinke, C. O., Tudor, V., et al. 2017, MNRAS, 467, 2199
Banerjee, S. 2017, MNRAS, 467, 524
Banerjee, S. 2018, MNRAS, 473, 909
Banerjee, S., Baumgardt, H., & Kroupa, P. 2010, MNRAS, 402, 371
Banerjee, S., Belczynski, K., Fryer, C. L., et al. 2019, arXiv:1902.07718
Bartos, I., Kocsis, B., Haiman, Z., & Márka, S. 2017, ApJ, 835, 165
Bastian, N., & Lardo, C. 2018, ARA&A, 56, 83
Baumgardt, H., De Marchi, G., & Kroupa, P. 2008, ApJ, 685, 247
Baumgardt, H., & Hilker, M. 2018, MNRAS, 478, 1520
Baumgardt, H., Hilker, M., Sollima, A., & Bellini, A. 2019, MNRAS, 482, 5138
Baumgardt, H., & Makino, J. 2003, MNRAS, 340, 227
Belczynski, K., Heger, A., Gladysz, W., et al. 2016a, A&A, 594, A97
Belczynski, K., Holz, D. E., Bulik, T., & O'Shaughnessy, R. 2016b, Natur, 534, 512
Belczynski, K., Kalogera, V., & Bulik, T. 2002, ApJ, 572, 407
Bell, E. F., McIntosh, D. H., Katz, N., & Weinberg, M. D. 2003, ApJS, 149, 289
Belloni, D., Giersz, M., Askar, A., Leigh, N., & Hypki, A. 2016, MNRAS, 462, 2950
Belloni, D., Giersz, M., Rivera Sandoval, L. E., Askar, A., & Ciecielåg, P. 2019, MNRAS, 483, 315
Belloni, D., Zorotovic, M., Schreiber, M. R., et al. 2017, MNRAS, 468, 2429
Bird, S., Cholis, I., Muñoz, J. B., et al. 2016, PhRvL, 116, 201301
Breen, P. G., & Heggie, D. C. 2013, MNRAS, 432, 2779
Breivik, K., Kremer, K., Bueno, M., et al. 2018, ApJL, 854, L1
Casertano, S., & Hut, P. 1985, ApJ, 298, 80
Chatterjee, S., Fregeau, J. M., Umbreit, S., & Rasio, F. A. 2010, ApJ, 719, 915
Chatterjee, S., Rasio, F. A., Sills, A., & Glebbeek, E. 2013, ApJ, 777, 106
Chatterjee, S., Rodriguez, C. L., Kalogera, V., & Rasio, F. A. 2017a, ApJL, 836, L26
Chatterjee, S., Rodriguez, C. L., & Rasio, F. A. 2017b, ApJ, 834, 68
Chatterjee, S., Umbreit, S., Fregeau, J. M., & Rasio, F. A. 2013, MNRAS, 429, 2881
Choksi, N., Gnedin, O. Y., & Li, H. 2018, MNRAS, 480, 2343
Chomiuk, L., Strader, J., Maccarone, T. J., et al. 2013, ApJ, 777, 69
Church, R. P., Strader, J., Davies, M. B., & Bobrick, A. 2017, ApJL, 851, L4
Clark, G. 1975, ApJ, 199, L143
D'Orazio, D. J., & Samsing, J. 2018, MNRAS, 481, 4775
Davies, M. B. 1997, MNRAS, 288, 117
De, K., Kasliwal, M. M., Cantwell, T., et al. 2018, ApJ, 866, 72
de Mink, S. E., Pols, O. R., Langer, N., & Izzard, R. G. 2009, A&A, 507, L1
Decressin, T., Meynet, G., Charbonnel, C., Prantzos, N., & Ekström, S. 2007, A&A, 464, 1029
Denissenkov, P. A., & Hartwick, F. D. A. 2014, MNRAS, 437, L21
Di Carlo, U. N., Giacobbo, N., Mapelli, M., et al. 2019, MNRAS, 487, 2947
Dominik, M., Belczynski, K., Fryer, C., et al. 2012, ApJ, 759, 52
Dominik, M., Belczynski, K., Fryer, C., et al. 2013, ApJ, 779, 72
Duquennoy, A., & Mayor, M. 1991, A&A, 500, 337
Ebisuzaki, T., Makino, J., Tsuru, T. G., et al. 2001, ApJL, 562, L19
El-Badry, K., Quataert, E., Weisz, D. R., Choksi, N., & Boylan-Kolchin, M. 2019, MNRAS, 482, 4528
Ferraro, F. R., Lanzoni, B., Dalessandro, E., et al. 2012, Natur, 492, 393
Ferraro, F. R., Lanzoni, B., Dalessandro, E., et al. 2019, NatAs, 3, 1149
Fragione, G., Antonini, F., & Gnedin, O. Y. 2018a, MNRAS, 475, 5313
Fragione, G., & Kocsis, B. 2018, PhRvL, 121, 161103
Fragione, G., & Kocsis, B. 2019, MNRAS, 486, 4781
Fragione, G., Leigh, N. W. C., Ginsburg, I., & Kocsis, B. 2018b, ApJ, 867, 119
Fragione, G., Leigh, N. W. C., & Perna, R. 2019a, MNRAS, 488, 2825
Fragione, G., Leigh, N. W. C., Perna, R., & Kocsis, B. 2019b, MNRAS, 489, 727
Fragione, G., Pavlík, V., & Banerjee, S. 2018c, MNRAS, 480, 4955
Fregeau, J. M., Cheung, P., Portegies Zwart, S. F., & Rasio, F. A. 2004, MNRAS, 352, 1
Fregeau, J. M., Gurkan, M. A., Joshi, K. J., & Rasio, F. A. 2003, ApJ, 593, 772
Fregeau, J. M., & Rasio, F. A. 2007, ApJ, 658, 1047
Freitag, M., Gürkan, M. A., & Rasio, F. A. 2006, MNRAS, 368, 141
Frohmaier, C., Sullivan, M., Maguire, K., & Nugent, P. 2018, ApJ, 858, 50
Fryer, C. L., Belczynski, K., Wiktorowicz, G., et al. 2012, ApJ, 749, 91
Fryer, C. L., & Kalogera, V. 2001, ApJ, 554, 548
Fujii, M. S., & Portegies Zwart, S. 2016, ApJ, 817, 4
Geller, A. M., & Mathieu, R. D. 2011, Natur, 478, 356
Gieles, M., Charbonnel, C., Krause, M. G. H., et al. 2018, MNRAS, 478, 2461
Giersz, M., Leigh, N., Hypki, A., Lützgendorf, N., & Askar, A. 2015, MNRAS, 454, 3150
Giesers, B., Dreizler, S., Husser, T.-O., et al. 2018, MNRAS, 475, L15
Giesers, B., Kamann, S., Dreizler, S., et al. 2019, A&A, 632, 3
Giesler, M., Clausen, D., & Ott, C. D. 2018, MNRAS, 477, 1853
Gnedin, O. Y., Ostriker, J. P., & Tremaine, S. 2014, ApJ, 785, 71
Gosnell, N. M., Leiner, E. M., Mathieu, R. D., et al. 2019, ApJ, 885, 45
Goswami, S., Umbreit, S., Bierbaum, M., & Rasio, F. A. 2012, ApJ, 752, 43
Grindlay, J. E., Cool, A. M., Callanan, P. J., et al. 1995, ApJL, 455, L47
Gürkan, M. A., Freitag, M., & Rasio, F. A. 2004, ApJ, 604, 632
Habibi, M., Stolte, A., Brandner, W., Hußmann, B., & Motohara, K. 2013, A&A, 556, A26
Harris, W. E. 1996, AJ, 112, 1487
Harris, W. E., Morningstar, W., Gnedin, O. Y., et al. 2014, ApJ, 797, 128
Heggie, D., & Hut, P. 2003, The Gravitational Million-Body Problem: A Multidisciplinary Approach to Star Cluster Dynamics (Cambridge: Cambridge Univ. Press)
Heggie, D. C. 1975, MNRAS, 173, 729
Heinke, C. O. 2010, in AIP Conf. Ser. 1314, Int. Conf. on Binaries, ed. V. Kalogera & M. van der Sluys (Melville, NY: AIP), 135
Heinke, C. O., Grindlay, J. E., Edmonds, P. D., et al. 2005, ApJ, 625, 796
Hénon, M. 1971a, Ap&SS, 13, 284
Hénon, M. 1971b, Ap&SS, 14, 151
Hills, J. G., & Day, C. A. 1976, ApL, 17, 87
Hoang, B.-M., Naoz, S., Kocsis, B., Rasio, F. A., & Dosopoulou, F. 2018, ApJ, 856, 140
Hobbs, G., Lorimer, D. R., Lyne, A. G., & Kramer, M. 2005, MNRAS, 360, 974
Hong, J., Vesperini, E., Askar, A., et al. 2018, MNRAS, 480, 5645
Hurley, J. R., Pols, O. R., & Tout, C. A. 2000, MNRAS, 315, 543
Hurley, J. R., Tout, C. A., & Pols, O. R. 2002, MNRAS, 329, 897
Hut, P., McMillan, S., Goodman, J., et al. 1992, PASP, 104, 981
Hypki, A., & Giersz, M. 2017, MNRAS, 471, 2537
Isoyama, S., Nakano, H., & Nakamura, T. 2018, PTEP, 2018, 073E01
Ivanova, N. 2013, MmSAI, 84, 123
Ivanova, N., Chaichenets, S., Fregeau, J., et al. 2010, ApJ, 717, 948
Ivanova, N., Heinke, C. O., Rasio, F. A., et al. 2006, MNRAS, 372, 1043
Ivanova, N., Heinke, C. O., Rasio, F. A., Belczynski, K., & Fregeau, J. M. 2008, MNRAS, 386, 553
Ivanova, N., Rasio, F. A., Lombardi, J. C., Jr., Dooley, K. L., & Proulx, Z. F. 2005, ApJL, 621, L109
Jonker, P. G., Glennie, A., Heida, M., et al. 2013, ApJ, 779, 14
Joshi, K. J., Nave, C. P., & Rasio, F. A. 2001, ApJ, 550, 691
Joshi, K. J., Rasio, F. A., Zwart, S. P., & Portegies Zwart, S. 2000, ApJ, 540, 969
Kasliwal, M. M., Kulkarni, S. R., Gal-Yam, A., et al. 2012, ApJ, 755, 161
Kawamura, S., Ando, M., Seto, N., et al. 2011, CQGra, 28, 094011
Kiel, P. D., Hurley, J. R., Bailes, M., & Murray, J. R. 2008, MNRAS, 388, 393
King, I. 1962, AJ, 67, 471
Knigge, C. 2012, MmSAI, 83, 549
Knigge, C., Baraffe, I., & Patterson, J. 2011, ApJS, 194, 28
Kremer, K., Breivik, K., Larson, S. L., & Kalogera, V. 2017, ApJ, 846, 95
Kremer, K., Chatterjee, S., Rodriguez, C. L., & Rasio, F. A. 2018a, ApJ, 852, 29
Kremer, K., Chatterjee, S., Ye, C. S., Rodriguez, C. L., & Rasio, F. A. 2019a, ApJ, 871, 38
Kremer, K., Lu, W., Rodriguez, C. L., Lachat, M., & Rasio, F. 2019b, ApJ, 881, 75
Kremer, K., Rodriguez, C. L., Amaro-Seoane, P., et al. 2019c, PhRvD, 99, 063003
Kremer, K., Sepinsky, J., & Kalogera, V. 2015, ApJ, 806, 76
Kremer, K., Ye, C. S., Chatterjee, S., Rodriguez, C. L., & Rasio, F. A. 2018b, ApJL, 855, L15
Kremer, K., Ye, C. S., Chatterjee, S., Rodriguez, C. L., & Rasio, F. A. 2020, in IAU Symp. 351, Star Clusters: From the Milky Way to the Early Universe, ed. A. Bragaglia et al. (Cambridge: Cambridge Univ. Press), 357
Krolik, J. H., & Piran, T. 2011, ApJ, 743, 134
Kroupa, P. 2001, MNRAS, 322, 231
Kroupa, P., & Jerabkova, T. 2018, arXiv:1806.10605
Kulkarni, S. R., Hut, P., & McMillan, S. 1993, Natur, 364, 421
Leigh, N., Sills, A., & Knigge, C. 2011, MNRAS, 416, 1410
Leigh, N. W. C., Geller, A. M., McKernan, B., et al. 2018, MNRAS, 474, 5672

Lombardi, J. C. J., Warren, J. S., Rasio, F. A., Sills, A., & Warren, A. R. 2002, ApJ, 568, 939
Lunnan, R., Kasliwal, M. M., Cao, Y., et al. 2017, ApJ, 836, 60
Luo, J., Chen, L.-S., Duan, H.-Z., et al. 2016, CQGra, 33, 035010
Lyne, A., Brinklow, A., Middleditch, J., et al. 1987, Natur, 328, 399
Maccarone, T. J., Kundu, A., Zepf, S. E., & Rhode, K. L. 2007, Natur, 445, 183
Mackey, A. D., Wilkinson, M. I., Davies, M. B., & Gilmore, G. F. 2007, MNRAS, 379, L40
Mackey, A. D., Wilkinson, M. I., Davies, M. B., & Gilmore, G. F. 2008, MNRAS, 386, 65
MacLeod, M., Guillochon, J., Ramirez-Ruiz, E., Kasen, D., & Rosswog, S. 2016, ApJ, 819, 3
MacLeod, M., Macias, P., Ramirez-Ruiz, E., et al. 2017, ApJ, 835, 282
Mapelli, M. 2016, MNRAS, 459, 3432
Marsh, T. R., Nelemans, G., & Steeghs, D. 2004, MNRAS, 350, 113
Mathieu, R. D., & Geller, A. M. 2009, Natur, 462, 1032
McLaughlin, D. E., & van der Marel, R. P. 2005, ApJS, 161, 304
Merritt, D., Piatek, S., Portegies Zwart, S., & Hemsendorf, M. 2004, ApJL, 608, L25
Metzger, B. D., & Pejcha, O. 2017, MNRAS, 471, 3200
Miller-Jones, J. C. A., Strader, J., Heinke, C. O., et al. 2015, MNRAS, 453, 3918
Moody, K., & Sigurdsson, S. 2009, ApJ, 690, 1370
Morscher, M., Pattabiraman, B., Rodriguez, C., Rasio, F. A., & Umbreit, S. 2015, ApJ, 800, 9
Nelemans, G. 2005, in ASP Conf. Ser. 330, The Astrophysics of Cataclysmic Variables and Related Objects, ed. J. M. Hameury & J. P. Lasota (San Francisco, CA: ASP), 27
Nelemans, G., Yungelson, L. R., & Portegies Zwart, S. F. 2004, MNRAS, 349, 181
Paczyński, B. 1967, AcA, 17, 287
Pang, X., Grebel, E. K., Allison, R. J., et al. 2013, ApJ, 764, 73
Pattabiraman, B., Umbreit, S., Liao, W.-k., et al. 2013, ApJS, 204, 15
Pavlík, V., Kroupa, P., & Šubr, L. 2019, A&A, 626, A79
Perets, H. B., Li, Z., Lombardi, J. C., Jr., & Milcarek, S. R., Jr. 2016, ApJ, 823, 113
Peuten, M., Zocchi, A., Gieles, M., Gualandris, A., & Hénault-Brunet, V. 2016, MNRAS, 462, 2333
Piotto, G., King, I. R., Djorgovski, S. G., et al. 2002, yCat, 339
Portegies Zwart, S. F., Baumgardt, H., Hut, P., Makino, J., & McMillan, S. L. W. 2004, Natur, 428, 724
Portegies Zwart, S. F., & McMillan, S. L. W. 2002, ApJ, 576, 899
Portegies Zwart, S. F., McMillan, S. L. W., & Gieles, M. 2010, ARA&A, 48, 431
Ransom, S. M. 2008, in IAU Symp. 246, Dynamical Evolution of Dense Stellar Systems, ed. E. Vesperini, M. Giersz, & A. Sills (Cambridge: Cambridge Univ. Press), 291
Rappaport, S., Podsiadlowski, P., Joss, P. C., Di Stefano, R., & Han, Z. 1995, MNRAS, 273, 731
Rodriguez, C. L., Amaro-Seoane, P., Chatterjee, S., et al. 2018a, PhRvD, 98, 123005
Rodriguez, C. L., Amaro-Seoane, P., Chatterjee, S., & Rasio, F. A. 2018b, PhRvL, 120, 151101
Rodriguez, C. L., & Antonini, F. 2018, ApJ, 863, 7
Rodriguez, C. L., Chatterjee, S., & Rasio, F. A. 2016, PhRvD, 93, 084029
Rodriguez, C. L., & Loeb, A. 2018, ApJ, 866, 5
Rodriguez, C. L., Morscher, M., Pattabiraman, B., et al. 2015, PhRvL, 115, 051101
Rosswog, S., Ramirez-Ruiz, E., & Hix, W. R. 2009, ApJ, 695, 404
Samsing, J., & D'Orazio, D. J. 2018, MNRAS, 481, 5445
Samsing, J., D'Orazio, D. J., Kremer, K., Rodriguez, C. L., & Askar, A. 2019, arXiv:1907.11231
Samsing, J., Leigh, N. W. C., & Trani, A. A. 2018, MNRAS, 481, 5436
Sana, H., de Mink, S. E., de Koter, A., et al. 2012, Sci, 337, 444
Sandage, A. R. 1953, AJ, 58, 61
Sarajedini, A., Bedin, L. R., Chaboyer, B., et al. 2007, AJ, 133, 1658
Sasaki, M., Suyama, T., Tanaka, T., & Yokoyama, S. 2016, PhRvL, 117, 061101
Shara, M. M., & Hurley, J. R. 2002, ApJ, 571, 830
Shen, K. J. 2015, ApJL, 805, L6
Shen, K. J., Quataert, E., & Pakmor, R. 2019, ApJ, 887, 180
Shishkovsky, L., Strader, J., Chomiuk, L., et al. 2018, ApJ, 855, 55
Sigurdsson, S. 1993, ApJL, 415, L43
Sigurdsson, S., & Phinney, E. S. 1995, ApJS, 99, 609
Sills, A., & Glebbeek, E. 2010, MNRAS, 407, 277
Silsbee, K., & Tremaine, S. 2017, ApJ, 836, 39
Spera, M., & Mapelli, M. 2017, MNRAS, 470, 4739
Spera, M., Mapelli, M., Giacobbo, N., et al. 2019, MNRAS, 485, 889
Spitzer, L. 1987, Dynamical Evolution of Globular Clusters (Princeton, NJ: Princeton Univ. Press)
Spitzer, L. J. 1969, ApJL, 158, L139
Strader, J., Chomiuk, L., Maccarone, T. J., Miller-Jones, J. C. A., & Seth, A. C. 2012, Natur, 490, 71
Šubr, L., Kroupa, P., & Baumgardt, H. 2008, MNRAS, 385, 1673
Tauris, T. M., Langer, N., & Kramer, M. 2012, MNRAS, 425, 1601
The LIGO Scientific Collaboration, The Virgo Collaboration, Abbott, B. P., et al. 2019a, PhRvX, 9, 031040
The LIGO Scientific Collaboration, The Virgo Collaboration, Abbott, B. P., et al. 2019b, ApJ, 882, 24
Tylenda, R., Hajduk, M., Kamiński, T., et al. 2011, A&A, 528, A114
Umbreit, S., Fregeau, J. M., Chatterjee, S., & Rasio, F. A. 2012, ApJ, 750, 31
Ventura, P., D'Antona, F., Mazzitelli, I., & Gratton, R. 2001, ApJL, 550, L65
Verbunt, F., van Paradijs, J., & Elson, R. 1984, MNRAS, 210, 899
Vink, J. S., de Koter, A., & Lamers, H. J. G. L. M. 2001, A&A, 369, 574
Wang, L., Spurzem, R., Aarseth, S., et al. 2016, MNRAS, 458, 1450
Warner, B. 1995, CAS, 28
Weatherford, N. C., Chatterjee, S., Kremer, K., & Rasio, F. A. 2019, arXiv:1911.09125
Weatherford, N. C., Chatterjee, S., Rodriguez, C. L., & Rasio, F. A. 2018, ApJ, 864, 13
Webbink, R. F. 1984, ApJ, 277, 355
Woosley, S. E. 2016, ApJL, 824, L10
Yang, Y., Bartos, I., Haiman, Z., et al. 2019, ApJ, 876, 122
Ye, C. S., Kremer, K., Chatterjee, S., Rodriguez, C. L., & Rasio, F. A. 2019, ApJ, 877, 122
Zevin, M., Samsing, J., Rodriguez, C., Haster, C.-J., & Ramirez-Ruiz, E. 2019, ApJ, 871, 91
Ziosi, B. M., Mapelli, M., Branchesi, M., & Tormen, G. 2014, MNRAS, 441, 3703
Zocchi, A., Gieles, M., & Hénault-Brunet, V. 2019, MNRAS, 482, 4713